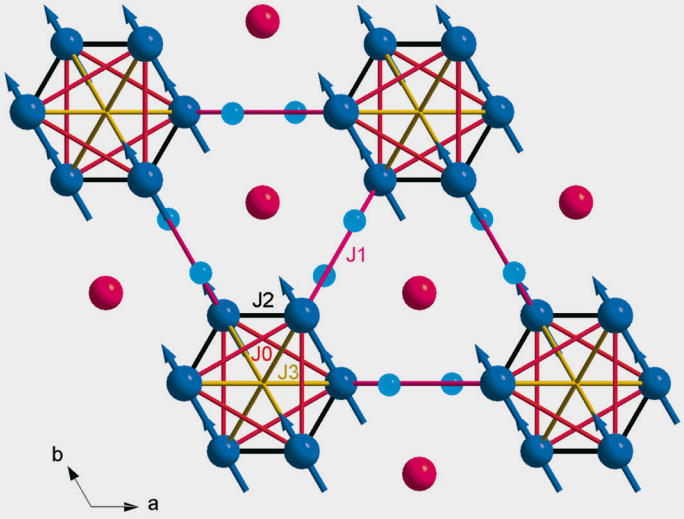

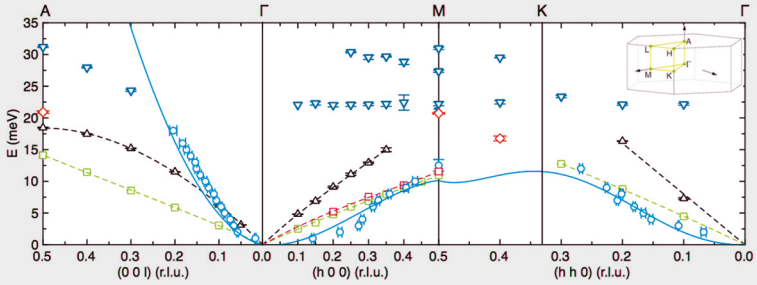

Inelastic neutron scattering on magnetocaloric compounds

Nikolaos Biniskos

Schlüsseltechnologien / Key Technologies
Band / Volume 186
ISBN 978-3-95806-362-4

Mitglied der Helmholtz-Gemeinschaft

JÜLICH
Forschungszentrum

Schriften des Forschungszentrums Jülich
Reihe Schlüsseltechnologien / Key Technologies Band / Volume 186

Forschungszentrum Jülich GmbH
Jülich Centre for Neutron Science (JCNS)
Quantenmaterialien und kollektive Phänomene (JCNS-2 / PGI-4)

Inelastic neutron scattering on magnetocaloric compounds

Nikolaos Biniskos

Schriften des Forschungszentrums Jülich
Reihe Schlüsseltechnologien / Key Technologies Band / Volume 186

ISSN 1866-1807 ISBN 978-3-95806-362-4

Bibliografische Information der Deutschen Nationalbibliothek.
Die Deutsche Nationalbibliothek verzeichnet diese Publikation in der
Deutschen Nationalbibliografie; detaillierte Bibliografische Daten
sind im Internet über http://dnb.d-nb.de abrufbar.

Herausgeber und Vertrieb:	Forschungszentrum Jülich GmbH Zentralbibliothek, Verlag 52425 Jülich Tel.: +49 2461 61-5368 Fax: +49 2461 61-6103 zb-publikation@fz-juelich.de www.fz-juelich.de/zb
Umschlaggestaltung:	Grafische Medien, Forschungszentrum Jülich GmbH
Druck:	Grafische Medien, Forschungszentrum Jülich GmbH
Copyright:	Forschungszentrum Jülich 2018

Schriften des Forschungszentrums Jülich
Reihe Schlüsseltechnologien / Key Technologies, Band / Volume 186

D 82 (Diss., RWTH Aachen University, 2018)

ISSN 1866-1807
ISBN 978-3-95806-362-4

Vollständig frei verfügbar über das Publikationsportal des Forschungszentrums Jülich (JuSER)
unter www.fz-juelich.de/zb/openaccess.

This is an Open Access publication distributed under the terms of the Creative Commons Attribution License 4.0,
which permits unrestricted use, distribution, and reproduction in any medium, provided the original work is properly cited.

Abstract

The search for more efficient use of energy has been leading to a growing interest in the research field of magnetocaloric materials. The magnetocaloric effect (MCE) refers to a change of temperature or entropy of a magnetic material exposed to a change of magnetic field. The MCE requires the exchange of magnetic, lattice and/or electronic entropy during an adiabatic (de-)magnetization process. A large MCE at room temperature and low magnetic field for a material with abundant and environmentally friendly elements opens the way for magnetic cooling devices.

From the $Mn_{5-x}Fe_xSi_3$ system, that exhibits a moderate MCE at low magnetic fields, two materials in single crystal form are under investigation: the ferromagnetic (FM) compound $MnFe_4Si_3$ and the parent compound Mn_5Si_3. The aim of this thesis is to investigate the spin and lattice dynamics and their couplings in these compounds that are up to nowadays unexplored with inelastic neutron scattering (INS) and inelastic X-ray scattering (IXS) measurements. Such studies might help to point out ingredients that may favour large MCE, such as phonon-magnon interaction, effect of spin fluctuations etc.

The FM compound $MnFe_4Si_3$ is a promising candidate for applications since it exhibits a moderate MCE near room temperature. Its magnetic excitation spectrum has been investigated by means of polarized and unpolarized INS. Spin-wave measurements at 1.5 K reveal a strong anisotropy of the magnetic exchange interactions along the (h00) and (00l) reciprocal directions of the hexagonal system, which also manifests itself in the q-dependent linewidths in the paramagnetic (PM) state. The correlation lengths indicate a short-range order, while the average linewidth is of the order of k_BT_C pointing to a behavior typical of many ferromagnets. In addition, the in- and out-of-plane spin-fluctuations are found to be isotropic around T_C and can be suppressed by a magnetic field of 2 T.

In order to study the spin and lattice dynamics and their interactions in $MnFe_4Si_3$, a combination of IXS and INS (polarized and unpolarized) measurements was performed. A remarkable feature evidenced by this combination of measurements is that along the (h00) direction the magnon branch close to the zone boundary falls exactly on the two transverse acoustic (TA) phonons. Furthermore, a large difference of intensities in the two non-spin-flip (NSF) channels was observed for one TA phonon mode. This difference of intensity between the two NSF channels can be attributed to the nuclear-magnetic interference term.

The parent compound Mn_5Si_3 has been extensively characterized as a model system by many groups in the past decades by magnetometry, X-ray and neutron diffraction on powder and single crystal samples. Previous studies indicate the existence of two stable antiferromagnetic (AF) phases at about 100 K (AF2) and 66 K (AF1), respectively. AF2 and AF1 transitions are of first-order and the inverse MCE (the sample heats up when an external magnetic field is applied adiabatically) is associated with the AF1-AF2 phase transition. INS experiments revealed that AF1 is characterized by sharp spin-waves, but AF2 is characterized by a mixed signal that resembles the one of the AF1 and PM state, indicating strong spin-fluctuations coexisting with spin-waves. Moreover, the application of a magnetic field in the AF1 phase induces spin-fluctuations, which points to their importance for the inverse MCE in Mn_5Si_3.

Zusammenfassung

Die Suche nach einer effizienteren Nutzung der Energie hat auch zu einem wachsenden Interesse an dem Forschungsgebiet magnetokalorischer Materialien geführt. Der magnetokalorische Effekt (MCE) beschreibt eine Änderung der Temperatur oder Entropie eines magnetischen Materials, das einer Magnetfeldänderung ausgesetzt ist. Der MCE erfordert den Austausch von magnetischer, Gitter- und/oder elektronischer Entropie wahrend eines adiabatischen (De-)magnetisierungsprozesses. Ein hoher MCE nahe Zimmertemperatur und niedrige Magnetfelder für Materialien bestehend aus ausreichend vorhandenen und umweltfreundlichen Elementen sind die beste Grundvorraussetzung für magnetische Kühlgeräte.

Aus dem System $Mn_{5-x}Fe_xSi_3$, das einen moderaten MCE bei niedrigen Magnetfeldern aufweist, werden zwei Materialien in Einkristallform untersucht: die ferromagnetische (FM) Verbindung $MnFe_4Si_3$ und die Ausgangsverbindung Mn_5Si_3. Das Ziel dieser Arbeit ist die Untersuchung der Spin- und Gitterdynamik und ihrer Kopplungen, die bis heute sowohl mit inelastischer Neutronenstreuung (INS) als auch mit inelastischer Röntgenstreuung (IXS) unerforscht sind. Diese Untersuchungen können helfen, Bestandteile aufzuzeigen, die einen grossen MCE begünstigen, wie z.B. Phonon-Magnon Wechselwirkung, Effekt von Spinfluktuationen, etc.

Die FM-Verbindung $MnFe_4Si_3$ ist ein vielversprechender Kandidat für Anwendungen, da sie einen moderaten MCE bei Zimmertemperatur aufweist. Das magnetische Anregungsspektrum wurde mit Hilfe von polarisierter und unpolarisierter INS untersucht. Spinwellenmessungen bei 1.5 K zeigen eine starke Anisotropie der magnetischen Austauschwechselwirkungen entlang der (h00) und (00l) reziproken Richtungen des hexagonalen Systems, die sich auch in der q-abhängigen Linienbreite im paramgnetischen (PM) Zustand manifestiert. Die Korrelationslängen weisen auf eine kurzreichweitige Ordnung hin, während die mittlere Linienbreite in der Grössenordnung k_BT_C liegt und somit ein für viele Ferromagnete typisches Verhalten aufweist. Die Spinfluktuation werden ausserdem in der Ebene und senkrecht dazu als isotrop nahe T_C gefunden und können durch ein Magnetfeld von 2 T unterdrückt werden.

Um die Spin- und Gitterdynamik und ihre Wechselwirkungen in $MnFe_4Si_3$ zu untersuchen, wurde eine Kombination aus IXS und INS Experimenten durchegführt (polarisiert und unpolarisiert). Durch diese Kombination beider Messmethoden wurde die bemerkenswerte Tatsache ersichtlich, dass entlang der (h00) Richtung der Magnonenzweig nahe des Zonenrandes exakt auf die beiden transversalen akustischen (TA) Phononenzweige fällt. Desweiteren wurde ein grosser Intensitätsunterschied in den zwei non-spin-flip (NSF) Kanälen für eine TA Phononmode beobachtet. Diese Differenz in der Intensität zwischen den beiden NSF Kanälen kann dem nuklearen-magnetischen Interferenzterm zugeschrieben werden.

Die Ausgangsverbindung Mn_5Si_3 wurde in den vergangenen Jahrzehnten durch viele Gruppen als Modellsystem mit Hilfe von Magnetometermessungen, Röntgen- und Neutronendiffraktion in Pulver und Einkristallform ausführlich charakterisiert. Frühere Untersuchungen berichten von der Existenz zweier stabiler antiferromagnetischer (AF) Phasen unterhalb ca. 100 K (AF2) und 66 K (AF1). Die AF2 und AF1 Phasenübergänge sind erster Ordnung und der inverse MCE (die Probe erwärmt sich, wenn ein externes magnetisches Feld adiabatisch angelegt wird) wird mit dem Phasenübergang AF1-AF2 verbunden. INS Experimente lassen erkennen, dass AF1 durch scharfe Spinwellen charakterisiert wird, aber AF2 durch ein gemischtes Signal repräsentiert wird, das dem AF1 und PM Zustand ähnelt, was auf eine Koexistenz von scharfen Spinwellen und Spinfluktuationen hindeutet. Ausserdem induziert ein Magnetfeld in der AF1 Phase Spinfluktuationen, was auf deren Bedeutung für den inversen MCE in Mn_5Si_3 hinweist.

Contents

1 Introduction **1**
1.1 Caloric effects in ferroic materials . . . 1
1.2 The magnetocaloric effect (MCE) . . . 1
1.2.1 History of the MCE and applications . . . 1
1.2.2 Theory of the MCE . . . 2
1.2.3 A magnetic refrigeration cycle . . . 3
1.3 Magnetocaloric compounds . . . 4
1.3.1 Classification of MC compounds . . . 4
1.3.2 The $Mn_{5-x}Fe_xSi_3$ series . . . 6
1.4 Elementary excitations . . . 9
1.4.1 Phonons . . . 9
1.4.2 Magnons . . . 11
1.5 Motivation . . . 12

2 Experimental techniques **13**
2.1 Properties of neutrons . . . 13
2.2 Basics of neutron scattering . . . 14
2.2.1 Neutron scattering from matter . . . 14
2.2.2 Cross-sections . . . 15
2.2.3 Nuclear scattering . . . 16
2.2.4 Magnetic scattering . . . 17
2.2.5 General properties of the scattering function $S(\mathbf{Q}, \omega)$ . . . 19
2.2.6 Polarized neutrons . . . 20
2.2.6.1 Nuclear scattering with polarized neutrons . . . 21
2.2.6.2 Magnetic scattering with polarized neutrons . . . 21
2.3 Inelastic X-ray scattering . . . 23

3 Experimental instruments **27**
3.1 The neutron triple axis spectrometer . . . 27
3.2 Polarized neutron scattering with triple axis spectrometer . . . 29
3.3 Inelastic X-ray scattering with ID28 . . . 30

4 Spin dynamics of the magnetocaloric compound $MnFe_4Si_3$ 33
4.1 Spin dynamics of localized and itinerant electron systems . . . 33
4.2 Experimental details . . . 34
4.3 Spin-wave scattering . . . 35
4.4 Paramagnetic scattering . . . 40
4.5 Spin dynamics under magnetic field . . . 44
4.6 Discussion . . . 46
4.7 Conclusions . . . 48

5 Unravelling the underlying mechanisms of the inverse magnetocaloric compound Mn_5Si_3 49
5.1 Inverse magnetocaloric compounds . . . 49
5.2 Experimental details . . . 50
5.3 Preliminary measurements . . . 51
5.4 Determination of phonon and spin-wave dispersion curves in the non-collinear AF1 phase 52
5.5 Spin dynamics in the collinear AF2 phase . . . 56
5.5.1 Unpolarized INS data . . . 56
5.5.2 Polarized INS data . . . 59
5.6 Field induced spin-fluctuations . . . 61
5.7 Discussion . . . 63
5.8 Conclusions . . . 64

6 Investigation of phonon-magnon interaction in the magnetocaloric compound $MnFe_4Si_3$ 65
6.1 Interaction between lattice and magnetic degrees of freedom . . . 65
6.2 Experimental details . . . 66
6.3 Investigating the lattice dynamics of $MnFe_4Si_3$ with IXS . . . 66
6.4 Investigating possible phonon-magnon interaction in $MnFe_4Si_3$ with INS and IXS . . . 69
6.5 Nuclear-magnetic interference . . . 71
6.6 Discussion . . . 73
6.7 Conclusions . . . 74

7 Summary and Outlook 75

A Appendix 77
A.1 Spin-wave simulations of $MnFe_4Si_3$ . . . 77
A.1.1 Input file for SpinWave software package . . . 77
A.1.2 Simulation of optic magnons and powder average of $MnFe_4Si_3$ . . . 79
A.2 Additional INS spectra of Mn_5Si_3 . . . 80
A.2.1 Unpolarized INS spectra of Mn_5Si_3 in the AF2 phase . . . 80
A.2.2 Unpolarized INS spectra of Mn_5Si_3 in the PM state . . . 80
A.3 Additional IXS spectra of $MnFe_4Si_3$ . . . 81
A.4 Additional polarized elastic and inelastic neutron spectra and temperature dependence of the magnetization of $MnFe_4Si_3$ . . . 81

B List of abbreviations 83

Bibliography **85**

Chapter 1

Introduction

1.1 Caloric effects in ferroic materials

Saving or using energy more efficiently nowadays could be the key to overcome the dramatic changes in the global climate. Gas compression refrigeration devices for industrial and residential applications are highly energy demanding and one possible way to reduce the energy consumption is to investigate alternative cooling techniques based on solid state caloric effects. The caloric effect is related to changes of a ferroic's material temperature or entropy under the sudden application of an external field: magnetic, electric, or mechanical.

Depending on the origin of the temperature/entropy change, the caloric effect can be classified as magnetocaloric, elastocaloric or mechanocaloric [1, 2, 3]. Magnetocaloric and electrocaloric materials show thermal changes in response to changes of an applied magnetic (ΔH) and electric (ΔE) field, respectively. Mechanocaloric materials show thermal changes in response to changes of applied stress field $\Delta\sigma$: elastocalorics (in literature are referred also as piezocalorics) and barocalorics respond to changes of uniaxial stress ($\Delta\sigma_u$) and hydrostatic pressure (Δp), respectively. A caloric material that exhibits thermal changes to more than one kind of driving field would be characterized as multicaloric [4]. At present, the magnetocaloric effect is considered as the most practical solid-state refrigerator technology [5].

1.2 The magnetocaloric effect (MCE)

1.2.1 History of the MCE and applications

The magnetocaloric effect (MCE) is the direct consequence of the variation of the total entropy of a magnetically responsive material in solid state when subjected to a magnetic field change and is an intrinsic property of any magnetic compound. Warburg (1881) is credited for the discovery that iron heats up or cools down by applying an external magnetic field change [6]. Later, Tesla (1890) [7] and Edison (1892) [8] held patents for a heat engine based on the MCE. Weiss and Piccard (1918) [9] were the first to establish the physical properties of the MCE and Debye (1926) [10] and Giauque (1927) [11] independently proposed the principle of adiabatic demagnetization (ADM). It was not until 1933 when Giauque and MacDougall demonstrated the ADM in paramagnetic salts, which has been employed for achieving ultralow temperatures in research laboratories for decades [12]. Since then several proof-of-

principle apparatus have been constructed for magnetic refrigeration at low temperatures and in 1976 Brown demonstrated magnetocaloric (MC) cooling near room temperature using the ferromagnetic (FM) material gadolinium [13]. In 1997 a magnetic refrigerator using Gd as refrigerating material demonstrated both the reliability and efficiency of such devices [14]. The apparatus works with a magnetic field of 5 T to yield a temperature span of 38 K and a cooling power of 100 W. The efficiency of a magnetic cooling device with a solid refrigerator material is as high as 60 % of the Carnot efficiency (at a temperature span of 5 K), where the best conventional gas compressor or vapour cycle refrigerators yield less than 40 % [5]. Meanwhile more than 100 MC compounds have been proposed for applications [5, 15, 16]. With the discovery of materials exhibiting the so-called giant MCE [17, 18], the interest and research publications in magnetic refrigeration at room temperature has greatly increased. Therefore, magnetic refrigeration based on the MCE might rapidly be applied in heat pumps, gas liquefaction, large-scale air conditioners, etc [19].

1.2.2 Theory of the MCE

The MCE consists of a materials thermal response when subjected to a magnetic field change and can be quantified as the temperature change in a material for an adiabatic magnetic field change (ΔT_{ad}), or as the entropy change in an isothermal process upon field variation (ΔS_{iso}). The relationship between the two properties is illustrated in Fig. 1.1. It shows the total entropy of a magnetic material at a fixed pressure as a function of temperature for two values of an applied external magnetic field. In the process A→B the magnetic field is applied isothermally. The alignment of the spins result in a lowering of the magnetic entropy and consequently in a lowering of the total entropy. In the process A→C the magnetic field is applied adiabatically (the material is completely thermally isolated). In order to conserve the total entropy, the system is forced to increase it's temperature. The quantities ΔS_{iso} and ΔT_{ad} are characteristic values for the MCE according to an initial temperature T and for a magnetic field change ΔH=H_2-H_1 and are given by $\Delta S_{iso}(T, \Delta H)$=$S(T, H_2)$-$S(T, H_1)$ and $\Delta T_{ad}(T, \Delta H)$=$T_2$-$T_1$.

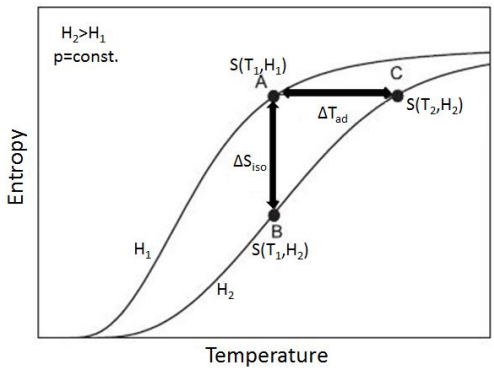

Figure 1.1: Schematic Entropy-Temperature diagram for constant pressure and two different magnetic fields (inspired by [20]).

If one considers the entropy as a function of temperature and magnetic field the total differential (at

constant pressure) can be written as:

$$dS(T,H) = \left(\frac{\partial S(T,H)}{\partial T}\right)_{H,p} dT + \left(\frac{\partial S(T,H)}{\partial H}\right)_{T,p} dH. \tag{1.1}$$

Using the Maxwell relation [16]:

$$\left(\frac{\partial S(T,H)}{\partial H}\right)_{T,p} = \left(\frac{\partial M(T,H)}{\partial T}\right)_{H,p}, \tag{1.2}$$

one obtains for ΔS_{iso}:

$$\Delta S_{iso}(T,\Delta H) = \int_{H_1}^{H_2} \left(\frac{\partial S(T,H)}{\partial H}\right)_{T,p} dH = \int_{H_1}^{H_2} \left(\frac{\partial M(T,H)}{\partial T}\right)_{H,p} dH. \tag{1.3}$$

Alternatively, ΔS_{iso} can be determined by use of the second law of thermodynamics:

$$\left(\frac{\partial S(T,H)}{\partial T}\right)_{H,p} = \left(\frac{C(T,H)}{T}\right)_{H,p}, \tag{1.4}$$

where $C(T,H)$ is the heat capacity. This results for ΔS_{iso} and ΔT_{ad} to:

$$\Delta S_{iso}(T,\Delta H) = \int_0^T \frac{C(T,H_2) - C(T,H_1)}{T} dT, \tag{1.5}$$

$$\Delta T_{ad}(T,\Delta H) = -\int_{H_1}^{H_2} \frac{T}{C(T,H)} \left(\frac{\partial S(T,H)}{\partial H}\right)_{T,p} dH = -\int_{H_1}^{H_2} \frac{T}{C(T,H)} \left(\frac{\partial M(T,H)}{\partial T}\right)_{H,p} dH. \tag{1.6}$$

If $C(T,H)$ is independent of T and H, then the ΔT_{ad} is coupled to the ΔS_{iso} via:

$$\Delta T_{ad}(T,\Delta H) = -\frac{T}{C}\Delta S_{iso}(T,\Delta H). \tag{1.7}$$

Significant MCE can be observed around a phase transition, where a relatively small magnetic field ($\approx$1 T) can produce a large entropy or temperature change. The MCE is expected to be large when the temperature derivative of the magnetization ($(\partial \mathrm{M}/\partial \mathrm{T})_H$) is large and $C(T,H)$ is small at the same temperatures. It should be noted that for the ADM no spontaneous thermodynamic transition is needed.

In a process where the applied magnetic field increases (ΔH>0) one can distinguish two types of MCE: i) the direct or conventional MCE, where $(\partial \mathrm{M}/\partial \mathrm{T})_H$<0, resulting to ΔS_{iso}<0 and ΔT_{ad}>0 (the MC compound heats up) and ii) the inverse MCE, where $(\partial \mathrm{M}/\partial \mathrm{T})_H$>0, resulting to ΔS_{iso}>0 and ΔT_{ad}<0 (the MC compound cools down).

1.2.3 A magnetic refrigeration cycle

If one neglects couplings between the lattice, magnetic and electronic degrees of freedom, the total entropy S of a magnetic material consists of the sum of the lattice (S_l), magnetic (S_m), and electronic (S_e) entropies. Assuming that only the magnetic entropy strongly depends on the magnetic field, the total entropy as a function of temperature and magnetic field at constant pressure can be expressed as [21]: $S(T, H)_p$=$(S(T)_l$+$S(T, H)_m$+$S(T)_e)_p$. Applying a magnetic field in a magnetic material causes a magnetic ordering of spins, resulting in a lowering of the magnetic entropy. The material's temperature directly influences the kinetics of the electrons and the lattice vibrations. Lowering the temperature (releasing

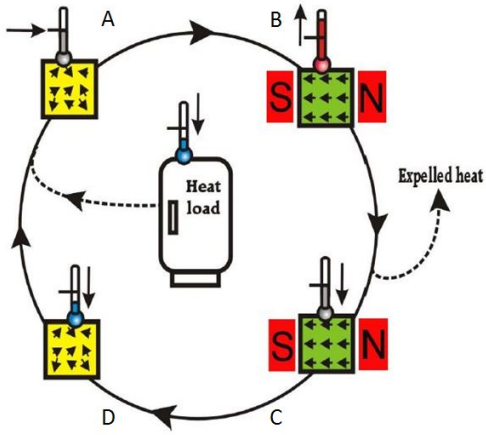

Figure 1.2: Schematic representation of a magnetic refrigeration cycle, which transports heat from the heat load to its surroundings (taken from [18]).

energy from the system) creates a more ordered system and therefore less entropy. A simplistic magnetic refrigeration cycle is visualized in Fig. 1.2.

In the process A→B in Fig. 1.2 an external magnetic field is applied under adiabatic conditions in a MC compound. The magnetic moments orient parallel to the applied field, decreasing S_m. The decrease in S_m is compensated by an increase in S_l and S_e, causing an increase in the temperature of the MC material. In the process B→C a heat transfer fluid (e.g., water if we are close to room temperature) can be employed to cool the MC compound back to its initial temperature. In C→D an adiabatic demagnetization process occurs (removal of magnetic field). The magnetic moments return to the original alignment causing an increase of S_m in the material and, therefore, decreasing its S_l, S_e and temperature. In the last step (process D→A), in order to cool the contents of the refrigerator, heat is extracted by passing a heat transfer fluid through the MC material. The cycle ABCDA is the basis for the construction of a magnetic refrigerator.

1.3 Magnetocaloric compounds

1.3.1 Classification of MC compounds

Since the MCE is expected to be large when spontaneous magnetic ordering occurs, the MC compounds can be classified according to the order of their magnetic phase transition. Materials that undergo a first-order phase transition (FOPT) show a discontinuity in the first derivative of the free energy with respect to a thermodynamic variable. The FOPT is not only magnetic but magnetostructural. Materials that undergo a second-order phase transition (SOPT) show a continuity and discontinuity in the first and second derivative of the free energy with respect to a thermodynamic variable, respectively. For MC compounds with FOPT giant MCE are reported with large values for ΔT_{ad} and ΔS_{iso}. However, large magnetic fields are necessary to trigger the magnetostructural transitions and the width of the peak shape for ΔS_{iso} is narrow, which limits the applicability of the materials for cyclic operation. In addition, large thermal and magnetic hysteresis imply a consumption of energy that is lost for the cooling process. On

the other hand materials that exhibit SOPT lack thermal hysteresis and a broader peak shape for ΔS_{iso} occurs around the transition temperature, but compared to materials with FOPT smaller values for ΔT_{ad} and ΔS_{iso} are reported [5]. It should be noted that independently of the order of the transition, the peak position of the maximum isothermal entropy change (ΔS_{MAX}) and temperature can be tuned by the purity and homogeneity of the MC material [22]. Nowadays, possibilities for developing devices that allow the use of different kinds of materials inside the same prototype are explored [24].

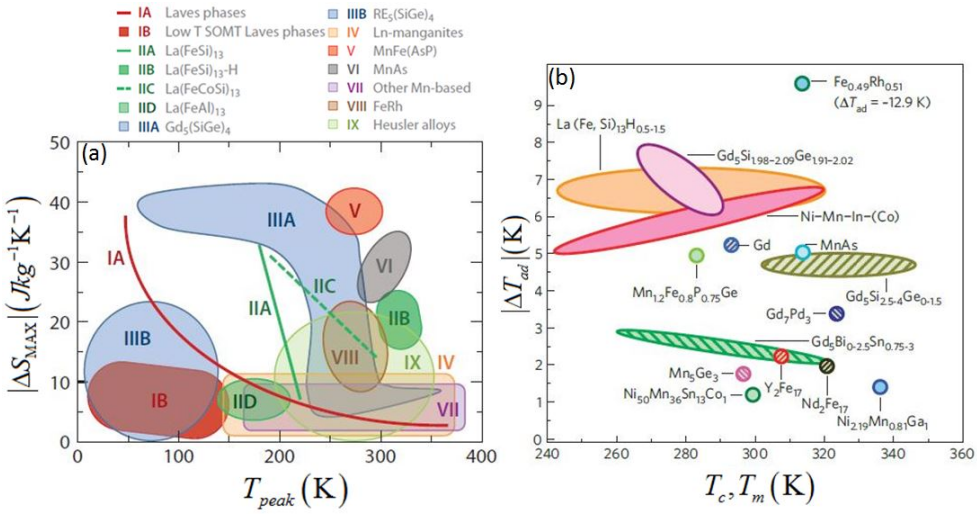

Figure 1.3: (a) Absolute value of maximum isothermal entropy change for field change from 0 to 5 T versus peak temperature for different families of MC materials (taken from [5]). (b) Absolute value of adiabatic temperature change versus transition temperature for field change from 0 to 2 T for various MC materials that either undergo a SOPT (T_c) (marked by hatched pattern) or a FOPT (T_m) (marked by solid fill-pattern) (taken from [39]).

Some representative materials investigated for their MC properties are shown in Figs 1.3(a)-(b). Apart from the pure metals [15] and the MC compounds that exhibit the giant MCE (e.g. $Gd_5Ge_{4-x}Si_x$ [17, 25], $LaFe_{13-x}Si_xH$ [26, 27, 28] and MnFeP(As,Ge) [18, 29]), materials such as manganites [30, 31, 32], amorphous alloys [33, 34, 35], Heusler alloys [39, 36, 37, 38], Laves phases [40, 41, 42] and other $3d$ and $4f$ metal based alloys and intermetallics [43, 44] have been extensively investigated for their magneto-thermodynamic properties. Up to nowadays, the largest ΔT_{ad} is reported for FeRh alloys (close to 1:1 stoichiometry), but the MCE is irreversible in this system [15, 45].

Except from the values of ΔT_{ad} and ΔS_{iso} that should be significant around room temperature for low magnetic field changes (ideally from 0 to 2 T), there is a number of other factors that must be taken into account for choosing materials for a commercial magnetic refrigeration design. These include: i) cheap, non-toxic, abundant, resistant to corrosion and environmentally friendly materials, ii) low manufacturing cost, iii) good mechanical properties, iv) high electrical resistance for avoiding Foucault currents during the rapid magnetic field changes, v) low specific heat and high thermal conductivity for increasing efficiency and vi) low thermal and magnetic hysteresis for high operation frequency.

1.3.2 The $Mn_{5-x}Fe_xSi_3$ series

Among the suggested MC compounds for applications the $Mn_{5-x}Fe_xSi_3$ ($0 \leq x \leq 5$) based systems are interesting candidates. They consist of abundant, non-toxic and cheap elements and they exhibit moderate MCE at low magnetic fields and at different temperatures depending on x (e.g. the magnetic entropy change for a field variation from 0 to 2 T is about 2 $JK^{-1}kg^{-1}$ for x=4) [46]. Figs 1.4(a) and 1.4(b) illustrate the rich phase diagram and the magnetic entropy change for these materials [46] and evidence that replacing Mn by Fe affects both the critical temperatures and ΔS_m. In the context of the MCE properties, for the parent compound Mn_5Si_3 the inverse MCE is reported, while for the x=3, 4, 5 it is the direct one. Early studies proposed that the $Mn_{5-x}Fe_xSi_3$ series crystallize in a hexagonal structure, with two distinguished crystallographic sites occupied by Mn and Fe in different ratios depending on composition [47]. In the present study emphasis is given to the Mn_5Si_3 and $MnFe_4Si_3$ compounds.

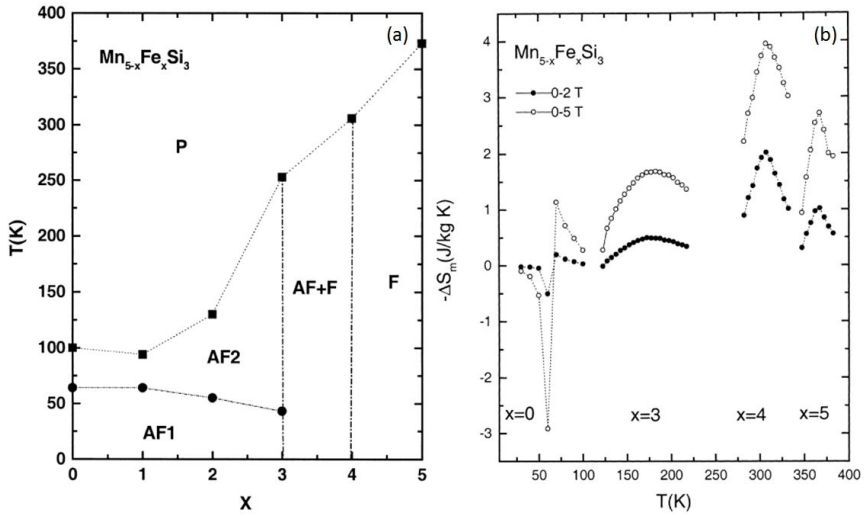

Figure 1.4: (a) Magnetic phase diagram and (b) magnetic entropy changes for two different magnetic field variations for the $Mn_{5-x}Fe_xSi_3$ system (taken from [46]).

The parent compound Mn_5Si_3 crystallizes in the high temperature paramagnetic (PM) state in the hexagonal $P6_3/mcm$ space group with two distinct crystallographic positions for Mn atoms (Wyckoff positions (WP) $6g$ for Mn2 and $4d$ for Mn1) [48]. With the onset of long-range magnetic order the symmetry is reduced to orthorhombic. Two first-order phase transitions towards antiferromagnetic (AF) phases occur at $T_{N_2} \approx 100$ K (AF2) and $T_{N_1} \approx 66$ K (AF1), respectively [46]. The magnetic structure of Mn_5Si_3 has been established with neutron diffraction experiments on single crystals. Associated with the AF2 ordering, a change of crystal structure to the orthorhombic space group $Ccmm$ occurs and Mn2 divides into two sets of inequivalent positions (Mn21 and Mn22). The orthorhombic cell dimensions are related to those of the hexagonal cell by $a_o = a_h$, $b_o \approx \sqrt{3}a_h$ and $c_o = c_h$ (see Fig. 1.5). Magnetic reflections in this cell follow the condition $h + k$ odd corresponding to the magnetic propagation vector $\boldsymbol{\kappa}$=(0, 1, 0) [49]. In this phase, the Mn1 and Mn21 atoms have no ordered moments, but the Mn22 atoms have their magnetic moments of magnitude 1.48(1) μ_B aligned almost parallel and antiparallel to the b-axis (see Fig. 1.5) [49]. A small deviation from collinearity occurs and is temperature dependent increasing up

to 8 ° near 70 K [49, 50]; AF2 is nonetheless named as collinear phase in this work. Another structural distortion occurs concomitantly with the AF1 ordering towards an orthorhombic cell without inversion symmetry (space group $Cc2m$) [51]. The magnetic moments reorient in a highly non-collinear and non-coplanar arrangement, while the propagation vector remains the same. Mn1 atoms (Mn11≈Mn12) acquire a magnetic moment (1.20(5) μ_B) and are oriented parallel and antiparallel to the direction with polar coordinates θ=116(1) °, ϕ=105(1) °, where θ is measured from [001] and ϕ from (010). Still the Mn21 atoms have no moments like in the AF2 phase. The Mn22 sites (Mn23 and Mn24) related by the centre of symmetry are no longer magnetically equivalent in the AF1 phase and carry a moment of 2.30(9) and 1.85(9) μ_B depending on their site position (see Fig. 1.5 and Table 1.1). Neutron diffraction [50, 52] and macroscopic measurements [53, 54] indicate that Mn_5Si_3 undergoes several magnetic phase transitions under magnetic field and temperature with the inverse-MCE observed in the vicinity of the AF1-AF2 phase transition.

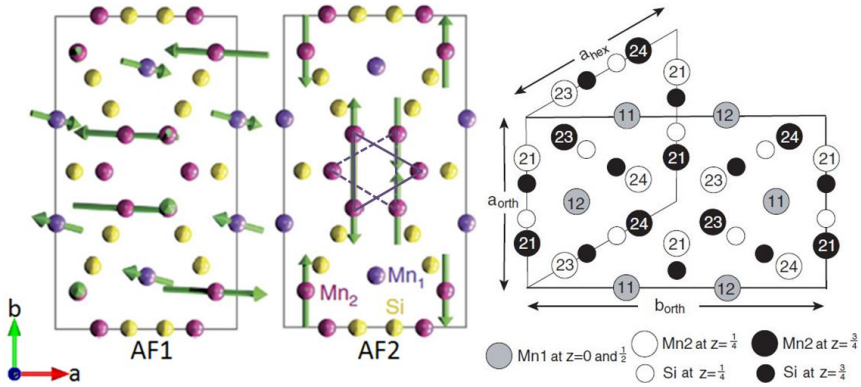

Figure 1.5: Projection in the (a,b) plane of the orthorhombic unit cell of Mn_5Si_3 in the two AF phases (taken from [55]). The triangles with continuous and dashed lines are located in different planes separated by $c/2$. The relationship between the orthorhombic and hexagonal unit cells is shown in the right figure. For the AF1 phase Mn11≈Mn12 and the Mn23 and Mn24 sites correspond to the Mn22 sites of the AF2 phase (taken from [52]).

Table 1.1: Manganese atomic positions in the PM state and the two AF phases of Mn_5Si_3. In the two ordered AF phases the magnitude and the direction of the magnetic moments is given according to single crystal neutron diffraction data [49, 51]. θ is measured from [001] and ϕ from (010).

PM	AF2			AF1		
$P6_3/mcm$	$Ccmm$			$Cc2m$		
atomic positions	atomic positions	moment direction	magnitude	atomic positions	moment direction	magnitude
Mn1 in 4d	Mn1 in 8e	–	–	Mn11 in 4a	θ=116(1) ° ϕ=105(1) °	1.20(5) μ_B
Mn2 in 6g	Mn21 in 4c	–	–	Mn21 in 4b	–	–
	Mn22 in 8g	parallel and antiparallel to [010]	1.48(1) μ_B	Mn23 in 4b	$\pm(\theta$=70(1) ° ϕ=93(1) °)	2.30(9) μ_B
				Mn24 in 4b	$\pm(\theta$=21(1) ° ϕ=11(1) °)	1.85(9) μ_B

From the $Mn_{5-x}Fe_xSi_3$ series, the FM compound $MnFe_4Si_3$ is the most promising one in means of applications, since a transformation from the PM state to the FM phase occurs at the Curie temperature

(T_C) ≈300 K [56, 57, 58] with | ΔS_m |≈2 $JK^{-1}kg^{-1}$ for a field change from 0 to 2 T [46, 56]. The order of the FM transition seems not to be fully established. Hysteresis loops point to a first-order FM transition [56]. Recent measurements of hyperfine fields with Mössbauer spectroscopy propose that the type of the magnetic transition cannot be strictly characterized as first or second-order [59]. In this framework it is worthwhile to note that in Fe_2P-based MC materials the order of the FM transition changes from first to second order depending on composition [60]. According to recent X-ray and neutron diffraction experiments performed on single crystals indicate that $MnFe_4Si_3$ crystallizes in the hexagonal space group $P\overline{6}$ [56]. While in the higher symmetrical space group $P6_3/mcm$ three symmetrically independent sites are occupied in the structure (M1 at WP position 6g; M2 at WP 4d; Si at WP 6g); these Wyckoff positions are split in space group $P\overline{6}$, and six symmetrically independent sites exist (M1a/M1b; M2a/M2b; Si1a/Si1b). The M2a/M2b sites are exclusively occupied by Fe, while M1a/M1b sites have a mixed occupancy of Mn and Fe. In this structure (see Fig. 1.6 and Table 1.2), the sites with mixed occupancy of Mn/Fe carry an ordered magnetic moment of approximately 1.5(2) μ_B, while no significant magnetic moment could be determined on the position which is occoupied by Fe [56]. The direction of the magnetic moments is consistent with magnetization measurements performed on single crystals, where a strong anisotropy is found with the easy axis of magnetization lying perpendicular to the c-axis [56].

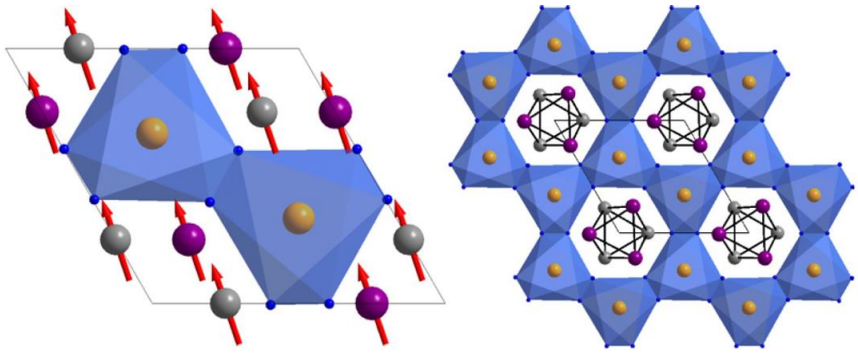

Figure 1.6: Projection of the structure of $MnFe_4Si_3$ along the [001] direction in the hexagonal space group $P\overline{6}$ (taken from [56]). Sites occupied by Mn and Fe are shown in magenta and grey; sites exclusively occupied by Fe are shown in orange; Si atoms are shown in blue. Magenta and grey sites are in different layers along the [001] direction.

Table 1.2: Mn and Fe atomic positions in the PM state and the FM phase of $MnFe_4Si_3$ according to single crystal neutron diffraction data [56]. θ is measured from the [100] direction.

PM		FM	
$P\overline{6}$		$P\overline{6}$	
atomic positions	occupancy	moment direction	magnitude
M1a in 3j	37.6(2)% Mn, 62.8(2)% Fe	θ=16(2) °	1.5(2) μ_B
M1b in 3k	27.7(7)% Mn, 72.3(7)% Fe	θ=16(2) °	1.5(2) μ_B
M2a in 2h	100% Fe	–	–
M2b in 2i	100% Fe	–	–

1.4 Elementary excitations

Ehrenfest classified the phase transitions based on the behavior of the thermodynamic free energy as a function of thermodynamic variables [61]. Phase transitions are categorized as first or second order depending on where the lowest derivative of the free energy is discontinuous at the transition. The various solid/liquid/gas transitions are first-order transitions (away from the critical point), because the change in density, which is the (inverse of the) first derivative of the free energy with respect to pressure, is discontinuous. Most of the PM to FM phase transition are classified as second-order transitions. Although first-order transitions may arise when structural change occur at the magnetic phase transition. In the former case the magnetization, which is the first derivative of the free energy with respect to the applied magnetic field, increases continuously from zero as the temperature decreases below T_c, but the magnetic susceptibility, the second derivative of the free energy with the field, changes discontinuously.

When a system enters its low temperature phase from the high temperature phase a symmetry is broken. In all ordered phases there are elementary excitations. In systems with continuous broken symmetries at the ordering temperature new collective excitations arise (see Table 1.3) and restore the broken symmetries. Investigating elementary excitations reveals dynamical properties of matter.

Table 1.3: Characteristic phase transitions and corresponding breaking of symmetries, order parameters and elementary excitations. ρ_G is the density. M and $M_\uparrow - M_\downarrow$ refer to the magnetization and staggered magnetization, respectively.

ordering	broken symmetry	high T phase	low T phase	order parameter	excitations
crystal	translation & rotation	liquid	solid	ρ_G	phonons
ferromagnetic	rotation & time	paramagnet	ferromagnet	M	magnons
antiferromagnetic	rotation & time	paramagnet	antiferromagnet	$M_\uparrow - M_\downarrow$	magnons

1.4.1 Phonons

If an atom in a crystal lattice is displaced from its equilibrium position by a small amount, then the forces acting on this atom will tend to make it return in its initial position. This results in lattice vibrations. Due to forces between the atoms in the crystal lattice, the displacement of one or more atoms from their equilibrium positions will cause a set of correlated vibrational waves that will propagate through the whole lattice. A simple model to describe this effect is to consider atoms in a crystal lattice as a series of harmonic oscillators (which corresponds to atoms coupled with elastic springs). Then the frequencies of motion will depend on the mass of the atoms and the strength of the springs connecting them.

According to quantum mechanics, the energy levels of the harmonic oscillator are quantized. Similarly the energy levels of lattice vibrations are quantized and the quantum of vibration is called phonon. Each phonon is having an energy of $\hbar\omega$, where ω is the frequency of the atomic motion. Phonon frequencies depend on the wave-length of the distortion, the mass of the atoms and the binding forces (analogous to the spring stiffness) that connects them. Phonons are bosons and the expected number of phonons in an energy state $\hbar\omega_s$ is given by the Bose-Einstein statistics $n_s(\boldsymbol{q})=\frac{1}{e^{\frac{\hbar\omega_s(\boldsymbol{q})}{k_BT}}-1}$.

In order to describe the dispersion relation $\omega(q)$ of a monoatomic linear chain, one considers a linear chain consisting of atoms with mass M, connected by springs with an average force constant C and

separated by a lattice constant a. By using the harmonic approximation (atomic vibrations are described as decoupled normal vibrations) together with Newton's second law and making a plane wave ansatz $u_n(t) = Ae^{i(qna-\omega t)}$, it is possible to deduce the dispersion relation for the phonon frequency as [63]:

$$\omega(q) = 2\sqrt{\frac{C}{M}} \mid sin\frac{qa}{2} \mid, \tag{1.8}$$

where q is the wave-vector. For one atom in one dimension, one obtains only one phonon branch. The sine dependence shows that: i) for small q-vectors (long wave-lengths) the frequency ω is linear in q, ω=$c_s q$ where c_s is the sound velocity and ii) for $q\rightarrow$0 the frequency tends to zero.

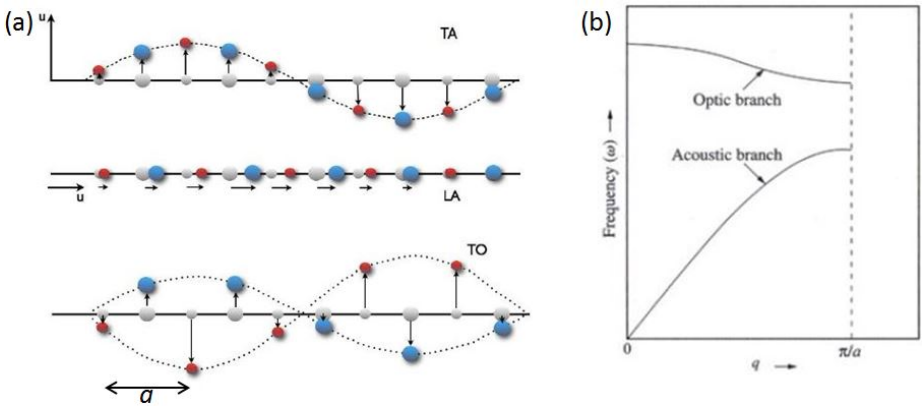

Figure 1.7: (a) Schematic representation of an infinite two-atomic linear chain with lattice constant a, where u represents the displacement (taken from [62]). Top left: transverse acoustic mode (TA), middle: longitudinal acoustic mode (LA), bottom left: transverse optic mode (TO). In an acoustic and optic mode the atomic motions are in and out of phase, respectively. (b) Dispersion of an acoustic and an optic phonon branch in a diatomic chain in the first Brillouin zone.

The function $\omega(q)$ is periodic with period $\frac{2\pi}{a}$, which is equal to a unit cell length in reciprocal space. All information concerning the frequencies and equation of motions is contained within the range -$\frac{\pi}{a}$<q<$\frac{\pi}{a}$. This range is called the first Brillouin zone. The values $\pm\frac{\pi}{a}$ are the Brillouin zone boundaries (lying half way between Brillouin zone centers) and there, in this simple case, the slope of the dispersion $\frac{d\omega(q)}{dq}$ is zero. Adding a reciprocal lattice vector τ=$\frac{2\pi}{a}$ to any point at any wave-vector gives the same result as in the first Brillouin zone.

Every atom has three degrees of freedom and therefore three modes of vibration are assigned along x, y and z. For crystals with r atoms in the unit cell there are 3r possible phonon modes. 3 are acoustic modes and the remaining (3r-3) are optic with a non-zero frequency at **q**=0. The modes can be further classified as longitudinal and transverse (see Fig. 1.7). In longitudinal modes the displacement u of the atoms is parallel to the propagation direction **q** of the vibration, whereas in the two transverse modes the displacement is perpendicular.

Phonon dispersion curves are usually measured experimentally and calculated theoretically along high symmetry direction of reciprocal space where degeneracies may occur. The frequency scale for phonons are typically in the THz region (1 THz=4.136 meV). The study of phonons is an important part of condensed matter physics because they play a major role in many physical properties, like thermal expansion, transport properties (thermal and electrical conductivity), heat capacity and superconductivity.

1.4.2 Magnons

In general magnetic systems are described by the Heisenberg Hamiltonian $H = -\sum_{ij} J_{ij}\mathbf{S}_i\mathbf{S}_j$, where J_{ij} is the exchange integral describing the exchange energy of overlapping charge distributions of the different atoms i and j. An electron system with its quantum mechanical exchange interaction will result to a spin-ordered ground state. For simplicity we can assume that this results to two different ground states: (i) spins ordered parallel (FM ground state) or (ii) antiparallel (AF ground state). Spin deviations from the average direction of the magnetic moments can be represented by the sum of deviations due to the set of propagating sinusoidal waves, which are named spin-waves. The concept of spin-waves is illustrated in Fig. 1.8. In a simple FM in the ground state all spins are aligned parallel to one direction. The z-component of a single spin S is $m_s = S$. Exciting this state the z-component is reduced ($m_s < S$). Since the spins are coupled with each other via the exchange interaction the movement of this spin will influence the neighbouring spins and will initialize a wave of spins processing around z-axis. The quantized particles of spin-waves are called magnons. There can be series of such wave-like motions and each spin will have a wave-length and a quantized energy $\hbar\omega_q$.

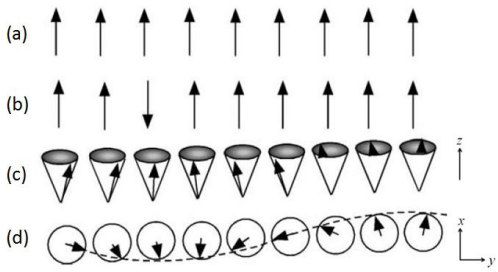

Figure 1.8: Visualization of FM spin-waves (taken from [64]). (a) Spin alignment of a simple FM in its ground state. (b) An isolated spin is reversed which costs a lot of energy. (c) A lower energy is achieved by sharing the disturbance among neighbouring atoms. All spins precess around the z-axis. (d) Component of spins in the xy-plane show a wave-like motion.

For a FM linear chain with nearest neighbour FM exchange interaction J separated by a distance a, the spin-wave dispersion is given by [65]:

$$\hbar\omega_q = 4SJ(1 - cos(qa)) \tag{1.9}$$

and is shown in Fig. 1.9(a). For small q-vectors (long wave-lengths) the dispersion relation is given by: $\hbar\omega_q \simeq 2SJa^2q^2 = Dq^2$, where D refers to the spin-wave stiffness. For an AF linear chain the magnon dispersion is given by [65]:

$$\hbar\omega_q = 4S \mid J \mid sin(qa) \tag{1.10}$$

and is shown in Fig. 1.9(b). In the long wave-length limit the dispersion relation is reduced to: $\hbar\omega_q \simeq 4S \mid J \mid aq = c_{sw}q$, where c_{sw} refers to the spin-wave velocity. The nearest neighbour exchange integral J is positive for ferromagnets and negative for antiferromagnets.

In general cases the spin-wave dispersion for systems with one magnetic atom per unit cell is written as [64]:

$$\hbar\omega_q = 2S(J_0 - J_{\mathbf{q}}), \tag{1.11}$$

where the term $J_{\mathbf{q}}$ is the Fourier transformed exchange coupling. $J_{\mathbf{q}}$ is given by: $J_{\mathbf{q}}=\sum_{l'} J_{ll'} e^{i\boldsymbol{q}(\boldsymbol{R}_l-\boldsymbol{R}_{l'})}$, with $\boldsymbol{R}_l$ and $\boldsymbol{R}_{l'}$ being the coordinates of the l_{th} and l'_{th} unit cell. In the spin-wave dispersions shown in Fig. 1.9 there are no gaps so that $\hbar\omega_q$=0 at **q**=0. In real systems, however, energy gaps may exist due to the single-ion anisotropy.

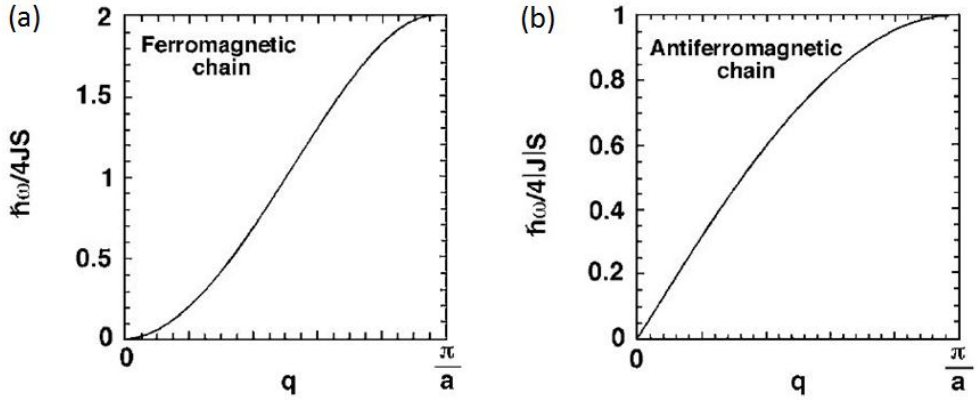

Figure 1.9: Spin-wave dispersion of (a) a FM and (b) an AF chain in a one dimensional lattice with lattice constant a in the first Brillouin zone (taken from [64]).

1.5 Motivation

Most groups from the magnetocaloric community are interested in quantifying the MCE via macroscopic measurements such as heat capacity and magnetization, and in establishing magneto-structural couplings in MC compounds with X-ray and neutron diffraction investigations. These measurements are essential, since the total entropy of a system depends on the magnetic and structural properties, but they cannot answer the question of the fundamental driving forces of the MCE. While different scenarios are well known for specific systems, no microscopic mechanism based on key ingredients such as coupling of spin, lattice and electronic degrees of freedom has been experimentally proven and to the knowledge of the author, in literature only few works have been published to this direction [66, 67, 68]. Inelastic neutron scattering (INS) experiments and as complementary inelastic X-ray scattering (IXS) measurements, can fulfil this need and provide key information, concerning the spin and lattice dynamics and their couplings of MC compounds.

The $Mn_{5-x}Fe_xSi_3$ series provide a very good opportunity to initiate such studies, because large and high quality (in terms of stoichiometry and homogeneity) single crystals can be grown straightforwardly with the Czochralski method. In this work, two materials will be investigated; the parent compound Mn_5Si_3, where the inverse MCE is reported and the FM compound $MnFe_4Si_3$, which is promising for near room temperature applications. In addition, literature provides a very strong background concerning the macroscopic and structural properties of these two MC compounds, which are necessary before starting inelastic measurements with neutrons and X-rays.

Chapter 2

Experimental techniques

2.1 Properties of neutrons

The neutron is an ideal probe for studying condensed matter under elastic and inelastic scattering conditions. Being uncharged particles, neutrons can interact very weakly with matter and penetrate deeply into materials. The zero net charge means that there is no Coulomb barrier to overcome and this implies that neutrons disregard the charged electronic cloud and interact directly with the atomic nucleus. The interaction between the nucleus of an atom and a neutron is short range ($\approx 10^{-13}$ cm). This is much less than the de Broglie wave-length of thermal neutrons $\lambda_{th} = \frac{h}{\sqrt{m_n k_B T}} \approx 10^{-8}$ cm=1 Å(neutrons coming from a moderator near room temperature), so the interaction can be considered point-like.

The neutron-nucleus scattering process contains only s-wave components and therefore is isotropic (with equal probability in any direction). This process is characterised by the scattering length b and for most elements is in the range of $0.2 \leq \mid b \mid \leq 1 \cdot 10^{-12}$ cm, comparable to the nuclear radius. The scattering length is a complex number, where its imaginary part corresponds to absorption; mainly radiative capture by the nuclei. For neutrons, in contrast with electrons and X-rays, the scattering is independent of the number of electrons and its strength varies among the elements and the isotopes of the same element. In addition, the scattering amplitude from a sample is equal to the sum of scattering amplitudes of individual atoms, due to the weakness of the neutron-atomic nucleus interaction.

Neutrons carry no charge, but their internal structure consisting of quarks and gluons, gives them a magnetic moment of μ_n=-1.913 μ_N, where $\mu_N = \frac{e\hbar}{2m_p}$ is the nuclear magneton. The neutron's magnetic moment interacts with the unpaired electron spins of magnetic atoms with a comparable strength to that of the nuclear interaction. Therefore, neutrons are a suitable probe for studying magnetic properties of matter. Moreover, the spin angular momentum of $\pm\frac{\hbar}{2}$ per neutron allows to prepare a spin-polarized neutron beam (a beam that contains a single angular momentum state): either spin-up, $+\frac{\hbar}{2}$, or spin-down, $-\frac{\hbar}{2}$. With spin-polarized neutron beams one can determine magnetic structures, separate the magnetic from the nuclear scattering, isolate the incoherent scattering from the total scattering, etc.

Another important feature of the neutron properties is their relatively large mass (m_n=1.675·10^{-24} g). The kinetic energy of neutrons produced from research reactors or spallation sources can be modified by collisions with atoms of similar mass from moderating mediums (e.g. hydrogen). The resulting energy distribution of the moderated neutrons is Maxwellian-like, and the average neutron velocity is determined by the temperature of the moderator. This provides neutrons with energies varying from 0.1 to 500 meV,

which are appropriate for studying a wide variety of dynamical phenomena in materials in solid and liquid state.

Despite the unique advantages that neutrons have as a non-destructive probe, they are weakly scattered once they penetrate matter; moreover, the available neutron beams provide low intensities. Synchrotron sources can provide fluxes of 10^{18} photons per second per square millimeter compared with 10^6 neutrons per second per square millimeter in the same energy bandwidth even at the most powerful continuous neutron sources.

2.2 Basics of neutron scattering

2.2.1 Neutron scattering from matter

When neutrons are scattered from matter, during the interaction the total energy and the momentum of the neutrons and matter are conserved. This is described via the equations [69]:

$$E = \hbar\omega = E_i - E_f = \frac{\hbar^2}{2m_n}(k_i^2 - k_f^2) \tag{2.1}$$

$$\hbar\mathbf{Q} = \hbar\mathbf{k}_f - \hbar\mathbf{k}_i. \tag{2.2}$$

In these equations, the wave-vector magnitude is $k = \frac{2\pi}{\lambda}$, where λ is the neutron wave-length of the neutron beam and the momentum transfer is $\hbar\mathbf{Q}$. The indices i and f refer to the incident and scattered neutron beam, respectively. The angle between the incident and scattered neutron beam is 2θ (scattering angle) and the energy transferred to matter is $E = \hbar\omega$. The vector relation between $\mathbf{Q}$, $\mathbf{k}_i$ and $\mathbf{k}_f$ is sketched in the so-called scattering triangle (see Fig. 2.1). From Eq. 2.2 the magnitude of $\mid \mathbf{Q} \mid$ can be defined via:

$$Q^2 = k_i^2 + k_f^2 - 2k_i k_f cos2\theta. \tag{2.3}$$

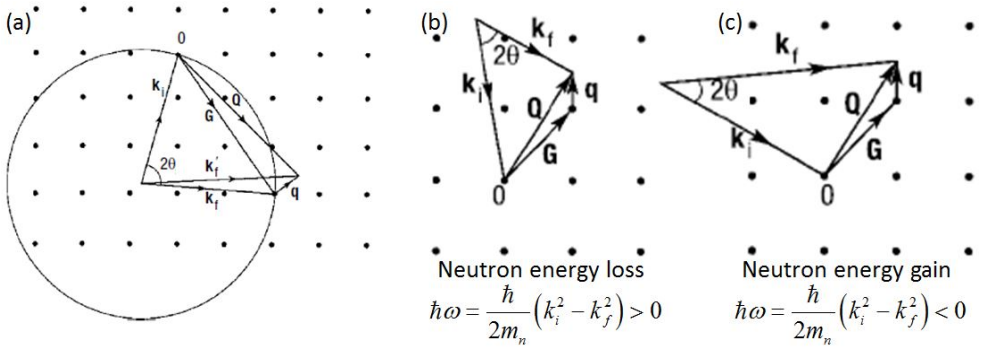

Figure 2.1: Vector relation between $\mathbf{Q}$, $\mathbf{k}_i$ and $\mathbf{k}_f$ for Bragg (elastic) and inelastic scattering process (taken from [69]). (a) Two-dimensional representation of reciprocal space showing the Ewald circle. $\mathbf{G}$ is a reciprocal lattice vector and $\hbar\mathbf{q}$ the momentum transfer within the first Brillouin zone. Inelastic scattering process for (b) neutron energy loss and (c) neutron energy gain. 0 represents the origin of reciprocal space.

The dots in Fig. 2.1 represent a reciprocal lattice with each point corresponding to a reciprocal lattice vector. For Bragg scattering the circle (Ewald circle) in Fig. 2.1(a) with radius k passes through two

points, one of which is the origin of reciprocal space. $\mathbf{k}_i$ and $\mathbf{k}_f$ correspond to the direction of the incident and diffracted neutron beam relative to the crystal, respectively. In this case, the Bragg condition $\mathbf{Q}=\mathbf{G}=\mathbf{k}_f-\mathbf{k}_i$ is satisfied, where $\mathbf{G}$ is a reciprocal lattice vector. For $|\mathbf{k}_i|=|\mathbf{k}_f|$ Eq. 2.3 can be rewritten as $|\mathbf{Q}|=|\mathbf{G}|=2|\mathbf{k}_i|\sin\theta=\frac{4\pi}{\lambda}\sin\theta$. This is the so-called Bragg's law and can be written in the more familiar form: $\lambda=2d\sin\theta$; the magnitude of the reciprocal lattice vector is $|\mathbf{G}|=\frac{2\pi}{d}$, where d is an interplanar spacing.

In an inelastic scattering process, where $|\mathbf{k}_i|\neq|\mathbf{k}_f|$, a difference of momentum is associated with an energy transfer to the sample. For inelastic experiments in single crystals, physics depends only on the relative wave-vector defined within a Brillouin zone, and therefore, $\mathbf{Q}$ is often decomposed into $\mathbf{Q}=\mathbf{G}+\mathbf{q}$. $\hbar\mathbf{q}$ is the momentum transfer within the first Brillouin zone and corresponds to the wave-vector of an elementary excitation, which is to be specified. For magnetically ordered systems, one can use the magnetic zone for convenience so that $\mathbf{Q}=\mathbf{G}+\mathbf{q}+\boldsymbol{\kappa}$, where $\boldsymbol{\kappa}$ is the propagation vector of the magnetic structure. It should be noted that for an INS experiment, one typically holds one vector constant (k_i or k_f), while changing the other. Figs 2.1(b) and 2.1(c) illustrate two cases where k_i is kept constant and k_f varies. In the first case (see Fig. 2.1(b)) $k_f<k_i$ resulting to $\hbar\omega>0$; energy is transferred from the incident neutron beam to the sample and an excitation is created. In the second case (see Fig. 2.1(c)) $k_f>k_i$ resulting to $\hbar\omega<0$; energy is transferred from the sample to the neutron beam and an excitation is annihilated. The former and the latter case are equivalent to the Stokes and the anti-Stokes scattering in optical spectroscopy, respectively.

2.2.2 Cross-sections

In a neutron scattering experiment one measures the fraction of neutrons of incident energy E_i scattered into an element of solid angle dΩ with an energy between E_f and E_f+dE_f. The measured quantity is the partial differential cross-section $\frac{d^2\sigma}{d\Omega dE_f}$ and has units of area·energy^{-1}·solid angle^{-1}. The partial differential cross-section describes a specific transition of the scattering system from one of its quantum states to another. In more general terms the quantity $\frac{d^2\sigma}{d\Omega dE_f}$ is a measurement of the response of the sample to an incident neutron beam with energy E_i and wave-vector k_i.

The partial differential cross-section has both a coherent and an incoherent part [70]:

$$\frac{d^2\sigma}{d\Omega dE_f}=\left(\frac{d^2\sigma}{d\Omega dE_f}\right)_{\text{coherent}}+\left(\frac{d^2\sigma}{d\Omega dE_f}\right)_{\text{incoherent}}, \tag{2.4}$$

where both terms have an elastic and inelastic contribution. Coherent scattering describes the way neutron waves are scattered from different nuclei and interfere constructively with each other. This type of scattering depends on the distances between atoms and on the scattering vector $\mathbf{Q}$. Coherent elastic scattering gives information about the equilibrium structure of the sample, while coherent inelastic scattering provides information about the collective motions of the atoms. Incoherent scattering describes the way the incident neutron wave interacts independently with each nucleus in the sample; the scattered waves from different nuclei have random relative phases and therefore cannot produce constructive interference. Incoherent elastic scattering is isotropic in all directions and creates an uniform background in the scattering experiments. Incoherent inelastic scattering results from the interaction of a neutron with the same atom at different positions and times. Therefore it provides information about atomic diffusion. The values for the coherent and incoherent scattering lengths for different elements and isotopes vary in a non systematic way across the periodic table. The coherent scattering length is given by $b_{coh}=\overline{b}$ (the scattering lengths of all the nuclei of the sample are $\overline{b}=\sum_n f_n b_n$, where b_n is the scattering length of a n

distinct isotope with nuclear spin **I** appearing with frequency f_n) and the incoherent scattering length is given by b_{incoh}=$\sqrt{\overline{b^2} - \overline{b}^2}$ (the scattering lengths deviations from the mean value $\overline{b}$).

Since the scattering of slow neutrons is a weak process it can be described by the first-order perturbation theory, i.e Fermi's Golden Rule for transition rates. The incident and scattered neutron states are treated as plane waves with energies E_i and E_f and wave-vectors $\mathbf{k}_i$ and $\mathbf{k}_f$. The double differential cross-section or response function is described in a four dimensional space and is given by [70]:

$$\frac{d^2\sigma}{d\Omega dE_f} = \left(\frac{m_n}{2\pi\hbar^2}\right)^2 \frac{k_f}{k_i} \sum_{n_0} p(n_0) \sum_{n_1} \mid \langle \mathbf{k}_f \sigma_f n_1 \mid V \mid \mathbf{k}_i \sigma_i n_0 \rangle \mid^2 \delta(\epsilon_1 - \epsilon_0 - \hbar\omega). \tag{2.5}$$

The indices 0 and 1 refer to the initial and final states of the sample, respectively. E is the energy of the neutron and ϵ the energy of the sample. The factor $\frac{k_f}{k_i}$ is related to the fact that the cross-section is defined as the ratio of the outgoing and incoming neutron flux. The sum $\sum_{n_0}$ runs over all initial states n_0 of the system, each occurring with a probability $p(n_0)$. The probability $p(n_0)$ at a given temperature T is calculated by: $p(n_0)$=$\frac{e^{-\frac{\epsilon n_0}{k_B T}}}{\sum_{n_0} e^{-\frac{\epsilon n_0}{k_B T}}}$. The sum $\sum_{n_1}$ runs over all final states n_1 of the system. The matrix element $\langle ... \rangle$ is between the initial (sample (n_0) + neutron ($\mathbf{k}_i$, σ_i)) and the final (sample (n_1) + neutron ($\mathbf{k}_f$, σ_f)) total state of the system. V is the interaction potential between the neutron and the sample. The δ function rules out the states (n_1, ϵ_1) for which energy is not conserved.

One formalism for interpreting the obtained data for $\frac{d^2\sigma}{d\Omega dE_f}$ is the linear response theory. Linear response theory is often written in terms of correlation functions, which depend on time and spatial coordinates. These correlation functions are usually written as $\langle$A($\boldsymbol{R}$, t)B($\boldsymbol{R}'$, t$'$)$\rangle$, where A and B are quantum mechanical operators for observable variables and the angular brackets denote thermal averages. The neutron cross-section is proportional to the Fourier transform of $\langle$A($\boldsymbol{R}$, t)B($\boldsymbol{R}'$, t$'$)$\rangle$ with respect to the time and spatial coordinates and the conjugate variables in the Fourier transform are the energy $\hbar\omega$ and momentum transfer $\hbar\mathbf{Q}$, respectively.

2.2.3 Nuclear scattering

For nuclear scattering due to the very short distance of the neutron-nucleus interaction the potential is a δ function and can be written in terms of the Fermi pseudo potential as [70]:

$$V(\mathbf{r}) = \frac{2\pi\hbar^2}{m_n} \sum_l b_l \delta(\mathbf{r} - \mathbf{R}_l), \tag{2.6}$$

where $\mathbf{R}_l$ is the position of the nucleus l and b_l its scattering length. Inserting the expression of the Fermi pseudo potential in Eq. 2.5, assuming unpolarized neutron beam and introducing quantum mechanical Heisenberg operators one obtains for nuclear scattering [70]:

$$\left(\frac{d^2\sigma}{d\Omega dE_f}\right)^{\text{nuclear}} = \frac{k_f}{k_i} \frac{1}{2\pi\hbar} \sum_{l,l'=1}^{N} \overline{b_{l'} b_l} \int_{-\infty}^{\infty} \langle e^{-i\mathbf{Q}\mathbf{R}_{l'}(0)} e^{i\mathbf{Q}\mathbf{R}_l(t)} \rangle e^{-i\omega t} dt = \frac{k_f}{k_i} S_n(\mathbf{Q}, \omega). \tag{2.7}$$

The scattering function or the dynamical structure factor $S_n(\mathbf{Q}, \omega)$ describes the properties of the sample and depends only on the momentum and the energy transferred from the neutron to the sample. The **Q** and the ω dependence of $S_n(\mathbf{Q}, \omega)$ provide information of where atoms are and how atoms move. N is the total number of nuclei, t is the time and $\boldsymbol{R}_l$ are the coordinates of the scattering centers. Assuming

that no correlation exists among the b values of different nuclei then one can separate the coherent and incoherent part of $S_n(\mathbf{Q},\omega)$ using $\overline{b_{l'}}\,\overline{b_l}=\overline{b}^2$ for $l'\neq l$ and $\overline{b_{l'}\,b_l}=\overline{b^2}$ for $l'=l$.

In a Bravais lattice the displacement of a nucleus from its equilibrium position m due to thermal motion is given by: $\boldsymbol{R}_m(t)=\boldsymbol{m}+\boldsymbol{u}_m(t)$, where $\boldsymbol{u}_m(t)$ is the Heisenberg operator for the atomic displacement. Assuming that the interatomic forces are linear functions of the atomic displacements, then $\boldsymbol{u}_m(t)$ can be expressed as a sum of a set of normal modes [70]:

$$\mathbf{Q}\cdot\mathbf{u}_m(t)=\sqrt{\frac{\hbar}{2MN}}\sum_s\frac{\mathbf{Q}\cdot\mathbf{e}_s}{\sqrt{\omega_s}}\left(a_s e^{i(\mathbf{q}\cdot\mathbf{m}-\omega_s t)}+a_s^\dagger e^{-i(\mathbf{q}\cdot\mathbf{m}-\omega_s t)}\right), \tag{2.8}$$

where ω_s refers to the frequency and $\boldsymbol{e}_s$ to the polarization vector of the mode s. The sum $\sum_s$ is over the N values of $\mathbf{q}$ in the first Brillouin zone and M is the mass of an atom (we assume all atoms are the same). a_s and $a_s^\dagger$ are the Heisenberg annihilation and creation operators, respectively. The expression for the coherent one phonon double differential cross-section is given by [70]:

$$\left(\frac{d^2\sigma}{d\Omega dE_f}\right)^{\text{1 phonon}}_{\text{coh}} = \frac{k_f}{k_i}\frac{\overline{b}^2(2\pi)^3}{2MV_0}e^{-2W(\mathbf{Q})}\sum_s\sum_\tau\frac{(\mathbf{Q}\cdot\mathbf{e}_s)^2}{\omega_s}\cdot \cdot\left(\langle n_s\rangle\delta(\omega+\omega_s)\delta(\mathbf{Q}+\mathbf{q}-\boldsymbol{\tau})+\langle n_s+1\rangle\delta(\omega-\omega_s)\delta(\mathbf{Q}-\mathbf{q}-\boldsymbol{\tau})\right), \tag{2.9}$$

where V_0 is the unit cell volume and $e^{-2W(\mathbf{Q})}$ the Debye-Waller factor. The cross-section in Eq. 2.9 contains the factors $\delta(\omega\pm\omega_s)$ and $\delta(\mathbf{Q}\pm\mathbf{q}-\boldsymbol{\tau})$, which implies that scattering occurs if two conditions are satisfied: i) $\omega=\pm\omega_s$ and ii) $\mathbf{Q}=\boldsymbol{\tau}\pm\mathbf{q}$. The first and second term after the double sum in Eq. 2.9 describe phonon annihilation and phonon creation by a neutron, respectively. In general, the quantity $\hbar\mathbf{Q}$ refers to the neutron momentum change, while $\hbar(\boldsymbol{\tau}+\mathbf{q})$ is the momentum imparted to the crystal.

The double differential nuclear cross-section for coherent one phonon scattering for a system containing different atoms with mass M_d at position d is given by [70]:

$$\left(\frac{d^2\sigma}{d\Omega dE_f}\right)^{\text{coh 1 phonon}}_{\text{dif. atoms}} = \frac{k_f}{k_i}\frac{(2\pi)^3}{2V_0}\sum_s\sum_\tau\frac{1}{\omega_s}\mid\sum_d\frac{\overline{b_d}}{\sqrt{M_d}}e^{-W_d}e^{i\mathbf{Qd}}(\mathbf{Q}\cdot\mathbf{e}_{ds})\mid^2\cdot \cdot\left(\langle n_s\rangle\delta(\omega+\omega_s)\delta(\mathbf{Q}+\mathbf{q}-\boldsymbol{\tau})+\langle n_s+1\rangle\delta(\omega-\omega_s)\delta(\mathbf{Q}-\mathbf{q}-\boldsymbol{\tau})\right) \tag{2.10}$$

It should be noted that in experiments one could measure different scattering intensities in different Brillouin zones for the same frequency due to terms involving the $\mathbf{Q}$ dependence in the scattering function.

2.2.4 Magnetic scattering

Neutrons are scattered from the magnetic field that is generated from unpaired electrons in a sample. The magnetic field has two sources: i) the electron spins lead to a dipole-dipole interaction and ii) moving electrons generate a field obtained from the Biot-Savart's equation. Unlike the nuclear interaction, the magnetic interaction is not isotropic. The strength of the magnetic interaction between the nucleus and the neutron depends on the relative orientations of their magnetic moments and the distance $\mathbf{r}$ between them.

The interaction potential due to the magnetic interaction between a neutron in spin-state $\boldsymbol{\sigma}$ and a moving electron with momentum $\mathbf{p}$ and spin $\mathbf{S}$ is given by [64]:

$$V(\mathbf{r})=-\gamma_N\mu_N 2\mu_B\boldsymbol{\sigma}\left(\nabla\left(\frac{\boldsymbol{S}\times\hat{\mathbf{R}}}{R^2}\right)+\frac{1}{\hbar}\frac{\boldsymbol{p}\times\hat{\mathbf{R}}}{R^2}\right), \tag{2.11}$$

where γ_N=-1.913 is the value of the neutron gyromagnetic ratio. The first and second term describe the spin and orbital interaction with the electron, respectively.

Inserting the expression of the magnetic interaction potential in Eq. 2.5, it is possible to obtain the magnetic scattering double differential cross-section of unpolarized neutron beam for identical magnetic ions and spin-only magnetism [71]:

$$\left(\frac{d^2\sigma}{d\Omega dE_f}\right)^{\text{magnetic}} = \frac{k_f}{k_i}(r_0\gamma_N)^2 f^2(\mathbf{Q}) e^{-2W(\mathbf{Q})} \sum_{\alpha,\beta}\left(\delta_{\alpha,\beta} - \frac{Q_\alpha Q_\beta}{Q^2}\right) \frac{1}{2\pi}\int_{-\infty}^{\infty} e^{-i\omega t} dt \sum_l e^{i\mathbf{Q}\mathbf{r}_l} \langle S_0^\alpha(0) S_l^\beta(t)\rangle$$
$$= (r_0\gamma_N)^2 \frac{k_f}{k_i} f^2(\mathbf{Q}) e^{-2W(\mathbf{Q})} \sum_{\alpha,\beta}\left(\delta_{\alpha,\beta} - \frac{Q_\alpha Q_\beta}{Q^2}\right) S^{\alpha\beta}(\mathbf{Q},\omega). \quad (2.12)$$

There are three important features concerning the magnetic neutron scattering in Eq. 2.12: i) the scattering amplitude is given by the classical electron radius r_0=0.282·10^{-12} cm and therefore, is of the same order of magnitude as the nuclear scattering, ii) the magnetic form factor $f(\mathbf{Q})$ is the Fourier transform of the normalized magnetization density and indicates that magnetic scattering decreases at increasing $\mathbf{Q}$ (as opposed to nuclear scattering) and iii) the polarization factor $\left(\delta_{\alpha,\beta} - \frac{Q_\alpha Q_\beta}{Q^2}\right)$ indicates that only components of the sample's magnetization that are perpendicular to the scattering vector $\mathbf{Q}$ are effective in the scattering process (the indices α and β refer to Cartesian coordinates).

The geometry for elastic magnetic scattering is illustrated in Fig. 2.2. The scattering is largest when $\mathbf{Q}$ is perpendicular to the magnetic moment $\boldsymbol{\mu}$. The magnetic interaction vector $\mathbf{S}_\perp$ is given by: $\mathbf{S}_\perp = \hat{\mathbf{Q}} \times (\mathbf{S} \times \hat{\mathbf{Q}})$, which leads to: $|\mathbf{S}_\perp|^2 = \sum_{\alpha,\beta}\left(\delta_{\alpha,\beta} - \frac{Q_\alpha Q_\beta}{Q^2}\right) S_\alpha^* S_\beta$.

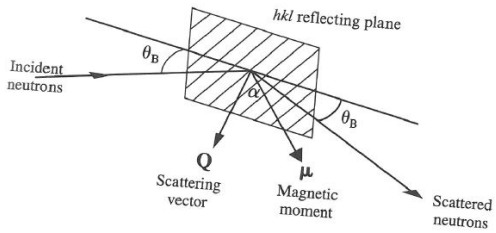

Figure 2.2: Sketched geometry of elastic magnetic scattering (taken from [72]). The intensity of the scattered beam is proportional to $\sin^2\alpha$. If $\boldsymbol{\mu}\|\mathbf{Q}$ the intensity is zero.

The inelastic unpolarized neutron double differential cross-section from the spin-waves, assuming identical magnetic ions with localized electrons and spin only scattering, with moment ordering along the z-direction, is given by the sum of terms for one magnon annihilation and creation by [64]:

$$\left(\frac{d^2\sigma}{d\Omega dE_f}\right)^{\text{1 magnon}} = \frac{k_f}{k_i}\frac{4\pi^3}{V_0}(r_0\gamma_N)^2 S f^2(\mathbf{Q}) e^{-2W(\mathbf{Q})}\left(1 - \left(\frac{Q_z}{Q}\right)^2\right)\sum_q\sum_\tau \cdot$$
$$\cdot\left(\langle n_q\rangle\delta(\omega+\omega_q)\delta(\mathbf{Q}+\mathbf{q}-\boldsymbol{\tau}) + \langle n_q+1\rangle\delta(\omega-\omega_q)\delta(\mathbf{Q}-\mathbf{q}-\boldsymbol{\tau})\right). \quad (2.13)$$

From the above equation one can see that peaks in the INS spectra will appear from spin-wave scattering if the conditions: i) $\omega = \pm\omega_q$ and ii) $\mathbf{Q} = \boldsymbol{\tau} \pm \mathbf{q}$ are satisfied, similarly to the coherent one phonon scattering process.

In a PM state of a localized magnetic system, for a temperature much higher than the ordering temperature, the magnetic moments of the ions are completely uncorrelated and randomly oriented. This

results to zero internal magnetic field. If the spin orientation of a particular ion changes there will be no energy change of the system. Therefore, the spin matrix element $\langle S_0^\alpha(0) S_l^\beta(t)\rangle$ is time independent. For a PM Bravais crystal with localized electrons in zero external magnetic field the cross-section is non-zero for l=0 and $\alpha = \beta$. This results to $\sum_{\alpha,\beta}\left(\delta_{\alpha,\beta} - \frac{Q_\alpha Q_\beta}{Q^2}\right) = 2$ and the elastic double differential cross-section is given by [64]:

$$\left(\frac{d^2\sigma}{d\Omega dE_f}\right)^{\text{PM}} = \frac{k_f}{k_i}(r_0\gamma_N)^2 \frac{1}{2\pi\hbar}\sum_l \mid f_l(\mathbf{Q}) \mid^2 \frac{1}{6} g_l^2 S_l(S_l+1), \tag{2.14}$$

where g_l is the Landé factor. Because of the Q dependence, the PM scattering decreases with increasing $\mathbf{Q}$ values, as demonstrated for the magnetic and spin-wave scattering. If a magnetic field H is applied along the z-axis, a nonzero average spin $\overline{S_z}$ leads to a coherent scattering that will be superimposed on the nuclear Bragg scattering (and is proportional to $\langle S^z\rangle^2$) and a diffusive signal. For a perfect PM, where no correlations and no interactions between atomic spins exist, the magnetic scattering is isotropic, elastic and independent of temperature.

2.2.5 General properties of the scattering function $S(\mathbf{Q},\omega)$

The scattering function $S(\mathbf{Q},\omega)$ is not a completely arbitrary function and since it is essentially related to a measured intensity, is always positive. The intensity relation for up-scattering ($\hbar\omega < 0$: annihilation of an excitation) and down-scattering ($\hbar\omega > 0$: creation of an excitation) is given through the detailed balance condition [73]:

$$S(-\mathbf{Q},-\omega) = e^{-\frac{\hbar\omega}{k_B T}} S(\mathbf{Q},\omega). \tag{2.15}$$

The detailed balance condition can be tracked back to the sum $\sum_{n_0} p(n_0)$ of the general Eq. 2.5 and can be used for systems in thermal equilibrium. For T=0 K there are no energy levels populated above the ground state, therefore, up-scattering is not possible. For high temperatures, the intensity is almost the same for up and down-scattering, since the transition rate for two nearly equally populated states is nearly the same. It should be noted that for systems with inversion symmetry $-\mathbf{Q}$ can be replaced by $\mathbf{Q}$ in Eq. 2.15.

When the response to a periodic perturbation is periodic with the same frequency, one can define another complex function, the generalized dynamic susceptibility $\chi(\mathbf{Q},\omega)$=$\chi'(\mathbf{Q},\omega)$+$i\chi''(\mathbf{Q},\omega)$. The real part describes the response in phase with the perturbation (reactive part), while the imaginary part is related to the out of phase response (dissipative part). The real and imaginary part of the susceptibility are related by the Kramers-Kronig relation [69]: $\chi'(\mathbf{Q},\omega) = \frac{1}{\pi}\int_{-\infty}^{\infty} \frac{\chi''(\mathbf{Q},\omega')}{\omega-\omega'} d\omega'$. The imaginary part $\chi''(\mathbf{Q},\omega)$ of the dynamical susceptibility, which is an odd function of ω, is related to the scattering function $S(\mathbf{Q},\omega)$ through [73]:

$$S(\mathbf{Q},\omega) = \frac{1}{\pi}\frac{1}{1-e^{-\frac{\hbar\omega}{k_B T}}}\chi''(\mathbf{Q},\omega). \tag{2.16}$$

One can connect $\chi''(\mathbf{Q},\omega)$ with the bulk susceptibility χ_b measured with a SQUID magnetometer, via the relation: $\chi_b = \lim_{\mathbf{Q}\to\mathbf{0}} -\chi'(\mathbf{Q},0) = \lim_{\mathbf{Q}\to\mathbf{0}} \frac{1}{\pi}\int_{-\infty}^{\infty} \frac{\chi''(\mathbf{Q},\omega')}{\omega'} d\omega'$.

An excitation at a given frequency ω_q and with an infinite life time can be expressed by delta functions as [73]: $S(\mathbf{Q},\omega) = (n(\omega)+1)\, Z_Q\, (\delta(\omega-\omega_q) - \delta(\omega+\omega_q))$, where Z_Q is a dimensionless structure

factor and $n(\omega)+1 = \left(1-e^{-\frac{\hbar\omega}{k_B T}}\right)^{-1}$. The two delta functions express creation and annihilation of excitations and the minus in the second delta function assures that $Z_Q\left(\delta(\omega-\omega_q)-\delta(\omega+\omega_q)\right)$ is an odd function of ω, since $\chi''(\mathbf{Q},\omega) \propto Z_Q\left(...\right)$. If an excitation has finite life time, but still remains well defined, then delta functions can be replaced by Lorentzians functions and one obtains [73]:

$$\begin{aligned} S(\mathbf{Q},\omega) = & \ \frac{1}{\pi}\left(n(\omega)+1\right) Z_Q \left(\frac{\Gamma_q}{(\omega-\omega_q)^2+\Gamma_q^2} - \frac{\Gamma_q}{(\omega+\omega_q)^2+\Gamma_q^2}\right) \\ & = \frac{1}{\pi}\left(n(\omega)+1\right) Z_Q \frac{4\omega\omega_q\Gamma_q}{(\omega^2-\Omega_q^2)^2+4\omega_q^2\Gamma_q^2}, \end{aligned} \tag{2.17}$$

where Γ_q is the q-dependent linewidth, corresponding to the half width at half maximum (HWHM) of the Lorentzian peak. Because a Lorentzian function corresponds to the exponential decay of the excitation in time, one can rewrite $S(\mathbf{Q},\omega)$ in terms of a damped harmonic oscillator function, where $\Omega_q = \sqrt{\omega_q^2+\Gamma_q^2}$.

For overdamped excitations and in the limit of small ω, one can use a quasielastic Lorentzian which describes a relaxation behaviour [73]:

$$S(\mathbf{Q},\omega) = \frac{1}{\pi}\left(n(\omega)+1\right)\frac{Z_Q}{\Omega_q'}\frac{\omega\Gamma_q'}{\omega^2+\Gamma_q'^2}. \tag{2.18}$$

A quasielastic Lorentzian is a Fourier transformation of an exponential decay $e^{-\frac{t}{\tau}}$, where $\tau^{-1}=\Gamma_q'$. For magnetic scattering, $\frac{Z_Q}{\Omega_q'}$ can be replaced by $\chi'(\mathbf{Q},0)$. Eq. 2.18 is used to described PM correlated systems as opposed to Eq. 2.14 that is used for uncorrelated PM systems.

2.2.6 Polarized neutrons

So far in the neutron cross-sections the neutron spin state was neglected and only the change from one momentum state to another was considered. In polarized neutron scattering experiments, both the momentum and the neutron spin state are considered. The polarization of neutrons is defined by the normalized average over the neutron spins **P**=$2\langle\mathbf{S}\rangle$ [62]. The polarization will be measured with respect to a quantization axis. In any device for polarization analysis the polarization of the neutron beam is defined by [62]:

$$P = \frac{n_\uparrow - n_\downarrow}{n_\uparrow + n_\downarrow}, \tag{2.19}$$

where $n_\uparrow$ and $n_\downarrow$ refer to up and down neutron spin orientations, respectively, with respect to a polarisation axis. P=1 and P=0 correspond to completely polarized and unpolarized neutron beam, respectively.

When the neutron polarization is considered then the double differential cross-section in Eq. 2.5 consists of four cross-sections [70]:

$$\frac{d^2\sigma}{d\Omega dE_f} = \frac{1}{2}(\text{sum of four spin state cross-sections}). \tag{2.20}$$

The four spin state cross-sections involve all the four possible spin state transitions for the initial and final neutron spin state, namely $\sigma_{\uparrow\uparrow}$, $\sigma_{\downarrow\downarrow}$, $\sigma_{\uparrow\downarrow}$ and $\sigma_{\downarrow\uparrow}$. The $\frac{1}{2}$ factor indicates that the probability for spin-up and spin-down neutron state is the same. In the general case the double differential cross-section for initial (σ_i) and final (σ_f) neutron spin states can be written as [69]:

$$\left(\frac{d^2\sigma}{d\Omega dE_f}\right)_{\sigma_i,\sigma_f}^{\text{polarized beam}} = \frac{k_f}{k_i}\sum_{i,f} P(i) \mid \langle f \mid \sum_l e^{i\mathbf{Q}\mathbf{r}_l} U_l^{\sigma_i,\sigma_f} \mid i\rangle \mid^2 \delta(E_i - E_f - \hbar\omega), \tag{2.21}$$

where P_i refers to the probability of being in the initial state $|i\rangle$ and $U_l^{\sigma_i,\sigma_f} = \langle\sigma_f \mid A_l + B_l\mathbf{I}_l\boldsymbol{\sigma} - \frac{r_0\gamma_n}{2}\mathbf{M}_{\perp l}\boldsymbol{\sigma}\mid \sigma_i\rangle$ to the scattering amplitude (see below).

2.2.6.1 Nuclear scattering with polarized neutrons

The nuclear interaction operator $\hat{V}_n$ can be described by a point-like and isotope specific Fermi pseudo potential as discussed before. For nuclei with zero spin the scattering length operator $\hat{b}$ is scalar and the scattering will be independent of the neutron spin orientation. The interaction becomes spin dependent if the scattering nuclei have a non-zero nuclear spin **I** and the scattering lengths differ for parallel and antiparallel alignment of **I** and **S**. Then $\hat{b}$ can be written as the sum of average and coherent part A and a fluctuating spin dependent part: $\hat{\mathbf{b}} = A + B\hat{\boldsymbol{\sigma}}\hat{\mathbf{I}}$ (A and B are constants). $\hat{\boldsymbol{\sigma}}$ is the Pauli spin operator given by the Pauli spin matrixes $\hat{\sigma}_x$=$\begin{pmatrix} 0 & 1 \\ 1 & 0 \end{pmatrix}$, $\hat{\sigma}_y$==$\begin{pmatrix} 0 & -i \\ i & 0 \end{pmatrix}$ and $\hat{\sigma}_z$=$\begin{pmatrix} 1 & 0 \\ 0 & -1 \end{pmatrix}$. Defining a polarization axis z for the neutron polarization **P**=2$\langle\hat{\mathbf{S}}\rangle$=$\langle\hat{\boldsymbol{\sigma}}\rangle$, with spin-up states $|+\rangle$=$\begin{pmatrix} 1 \\ 0 \end{pmatrix}$ and spin-down states $|-\rangle$=$\begin{pmatrix} 0 \\ 1 \end{pmatrix}$, one obtains the following matrix elements for nuclear scattering [69]:

$$\begin{aligned} \langle + \mid \hat{\boldsymbol{b}} \mid + \rangle &= A + BI_z \\ \langle - \mid \hat{\boldsymbol{b}} \mid - \rangle &= A - BI_z \\ \langle + \mid \hat{\boldsymbol{b}} \mid - \rangle &= B(I_x - iI_y) \\ \langle - \mid \hat{\boldsymbol{b}} \mid + \rangle &= B(I_x + iI_y). \end{aligned} \tag{2.22}$$

The obtained result is independent of the direction of **P** with respect to **Q**. For coherent scattering and assuming random orientation of nuclear spins, all scattering appears in the non-spin flip (NSF) channels. For incoherent scattering if $I = 0$ there is no spin flip (SF) scattering.

2.2.6.2 Magnetic scattering with polarized neutrons

The magnetic interaction potential is given by $\hat{V}_m = -\frac{r_0\gamma_n}{2}\hat{\boldsymbol{\sigma}}\hat{\mathbf{M}}_{\mathbf{Q}}^{\perp}$, with $\hat{\mathbf{M}}_{\mathbf{Q}}^{\perp}$ referring to the operator of the magnetic interaction that is reduced to only the perpendicular components of $\mathbf{M_Q}$ with respect to **Q** ($\mathbf{M}_{\mathbf{Q}}^{\perp} = \mathbf{e_Q} \times \mathbf{M_Q} \times \mathbf{e_Q}$) [62]. $\mathbf{M_Q}$ is the total Fourier transform of the spin and orbital contribution to the magnetization density.

For polarized neutron experiments, the usual convention is to define a cartesian coordinate system with the x-axis parallel to **Q**, the y-axis perpendicular to **Q** in the scattering plane and the z-axis perpendicular to the scattering plane. Since neutron scattering experiments probe only the magnetism perpendicular to the scattering vector **Q**, the measured magnetic fluctuations are therefore $\langle\delta M_y\rangle$ and $\langle\delta M_z\rangle$, where:

$$\langle\delta M_\alpha\rangle = S^{\alpha\alpha}(\mathbf{Q}, \omega). \tag{2.23}$$

The longitudinal polarization analysis (LPA) method allows to recover $\mathbf{P}_L$, the projection of the final polarization **P** onto the incident polarization $\mathbf{P}_0$. The longitudinal component of the polarization is given by $P_L = \frac{\mathbf{P}\cdot\mathbf{P}_0}{P_0}$. By neglecting terms arising from the nuclear spins, the chiral and nuclear-magnetic interference terms (NMI), one can deduce the following expressions for the NSF (the polarization does not change) and SF (completely reversion of the polarization) cross-sections in the different cases where

$\mathbf{P}_0$ is parallel to **x**, **y** and **z** [64]:

$$\begin{aligned}
\left(\frac{d^2\sigma}{d\Omega dE}\right)^{x}_{\text{NSF}} &\propto BG_{\text{NSF}} + \langle N\rangle \\
\left(\frac{d^2\sigma}{d\Omega dE}\right)^{x}_{\text{SF}} &\propto BG_{\text{SF}} + \langle \delta M_y\rangle + \langle \delta M_z\rangle \\
\left(\frac{d^2\sigma}{d\Omega dE}\right)^{y}_{\text{NSF}} &\propto BG_{\text{NSF}} + \langle N\rangle + \langle \delta M_y\rangle \\
\left(\frac{d^2\sigma}{d\Omega dE}\right)^{y}_{\text{SF}} &\propto BG_{\text{SF}} + \langle \delta M_z\rangle \\
\left(\frac{d^2\sigma}{d\Omega dE}\right)^{z}_{\text{NSF}} &\propto BG_{\text{NSF}} + \langle N\rangle + \langle \delta M_z\rangle \\
\left(\frac{d^2\sigma}{d\Omega dE}\right)^{z}_{\text{SF}} &\propto BG_{\text{SF}} + \langle \delta M_y\rangle,
\end{aligned} \tag{2.24}$$

where $\langle N\rangle$ refers to the nuclear scattering and BG_{NSF} and BG_{SF} are the background in the NSF and SF channel, respectively. In other words one can determine the structural and magnetic contributions by measuring the NSF and SF cross-sections in a configuration where $\mathbf{P}_0 \parallel \mathbf{Q}$. Magnetic fluctuations parallel to the neutron beam polarization are visible in the non-spin-flip channel, while fluctuations perpendicular to the neutron beam polarization give rise to the spin-flip signal (i.e. inversion of the polarization of the scattered beam with respect to the initial one).

In the general case where the symmetric nuclear-magnetic interference and antisymmetric chiral terms cannot be neglected the four differential cross-sections, $\sigma^{++} = \left(\frac{d^2\sigma}{d\Omega dE}\right)^{++}$, $\sigma^{--} = \left(\frac{d^2\sigma}{d\Omega dE}\right)^{--}$, $\sigma^{+-} = \left(\frac{d^2\sigma}{d\Omega dE}\right)^{+-}$ and $\sigma^{-+} = \left(\frac{d^2\sigma}{d\Omega dE}\right)^{-+}$ for an initial polarization applied, respectively, along **x**, **y** and **z** are given by [64]:

$$\begin{aligned}
\sigma_x^{++} &= \sigma_x^{\text{NSF}} \\
\sigma_x^{--} &= \sigma_x^{\text{NSF}} \\
\sigma_x^{+-} &= \sigma_x^{\text{SF}} - P_0 M_{\text{ch}} \\
\sigma_x^{-+} &= \sigma_x^{\text{SF}} + P_0 M_{\text{ch}} \\
\sigma_y^{++} &= \sigma_y^{\text{NSF}} + P_0 R_y \\
\sigma_y^{--} &= \sigma_y^{\text{NSF}} - P_0 R_y \\
\sigma_y^{+-} &= \sigma_y^{\text{SF}} \\
\sigma_y^{-+} &= \sigma_y^{\text{SF}} \\
\sigma_z^{++} &= \sigma_z^{\text{NSF}} + P_0 R_z \\
\sigma_z^{--} &= \sigma_z^{\text{NSF}} - P_0 R_z \\
\sigma_z^{+-} &= \sigma_z^{\text{SF}} \\
\sigma_z^{-+} &= \sigma_z^{\text{SF}},
\end{aligned} \tag{2.25}$$

where M_{ch} is the chiral term and R_α ($\alpha = y, z$) the symmetric NMI terms coupling the nuclear and the magnetic components in the direction α. The different terms, namely the nuclear. magnetic, NMI and chiral, can be determined separately from linear combinations of the previous relations.

2.3 Inelastic X-ray scattering

Photons with a wave-length of λ=0.1 nm have an energy of about 12 keV. Therefore, the study of phonon excitations in condensed matter, which are in the meV region, requires a relative energy resolution of at least $\frac{\Delta E}{E} \sim 10^{-7}$. There are a number of instances when inelastic X-ray scattering (IXS), using the backscattering technique, can compete with inelastic neutron scattering (INS) as a tool to study collective structural excitations. An example is that it is not possible to study acoustic excitations propagating with the speed of sound v_s using a probe particle with a speed $v < v_s$. Another advantage of the IXS technique arises from the fact that very small beam sizes (of the order of a few tens of micrometers) can be produced at todays synchrotron sources. This opens the way to study systems available only in small quantities as single crystals (down to a few 10^{-6} mm^3) and investigate them in extreme thermodynamic conditions, such as very high pressures combined with high temperatures.

For an inelastic X-ray scattering process, where the used probe is a photon beam, the momentum and energy conversion relations are:

$$E = \hbar\omega = E_i - E_f \tag{2.26}$$

$$\hbar\mathbf{Q} = \hbar\mathbf{k}_f - \hbar\mathbf{k}_i. \tag{2.27}$$

The relation between momentum and energy in the case of photons is different compared to neutrons since it is given by $E(k) = \hbar ck$. In the case for IXS the energy gains or losses associated with i.e. phonon excitations, are always much smaller than the energy of the incident photon ($E \ll E_i$). Therefore, the ratio between the exchanged momentum and the incident photon momentum is given by:

$$Q^2 = k_i^2 + k_f^2 - 2k_i k_f cos2\theta \xrightarrow{k_i \approx k_f} \frac{Q}{k_i} = 2sin\left(\frac{\theta}{2}\right), \tag{2.28}$$

where θ is the scattering angle. For IXS there is no limitations in the energy transfer at given momentum transfer for phonon excitations, in contrast to INS where a strong coupling between energy and momentum transfer exists due to the instrumental constrains.

In the weak relativistic limit and by neglecting resonance phenomena close to the X-ray absorption limit and the much weaker magnetic couplings, the electron-photon interaction is described via the Thomson interaction Hamiltonian [73]:

$$H_{\text{X-Th}} = \frac{1}{2} r_0 \sum_j \mathbf{A}^2(\mathbf{r}_j, t), \tag{2.29}$$

where r_0 refers to the classical electron radius and $\mathbf{A}(\mathbf{r}_j, t)$ to the electromagnetic field vector potential in the $\mathbf{r}_j$ coordinate of the jth electron. The sum $\sum_j$ is over all the electrons of the system. The double differential cross-section is proportional to the number of incident photons scattered with an energy range ΔE and momentum variation into a solid angle $\Delta\Omega$. In the process, where a photon with initial energy E_i, wave-vector $\mathbf{k}_i$ and polarization $\boldsymbol{\epsilon}_i$, is scattered into a final state of energy E_f, wave-vector $\mathbf{k}_f$ and polarization $\boldsymbol{\epsilon}_f$, and the electron system goes from an initial state $|I\rangle$ to a final state $|F\rangle$, one obtains for the double differential cross-section [73]:

$$\frac{d^2\sigma}{d\Omega dE_f} = r_0^2 (\boldsymbol{\epsilon}_i \cdot \boldsymbol{\epsilon}_f)^2 \frac{k_f}{k_i} \sum_{I,F} P_I \mid \langle F \mid \sum_j e^{i\mathbf{Q}\mathbf{r}_j} \mid I \rangle \mid^2 \delta(\hbar\omega - E_f - E_i). \tag{2.30}$$

The sum $\sum_{I,F}$ over the initial and final states is the thermodynamic average and P_I refers to the thermal population of the initial state.

Within the adiabatic approximation, the systems quantum state $|S\rangle$ can be seperated into a product of an electronic part $|S_e\rangle$ and a nuclear part $|S_n\rangle$: $|S\rangle$=$|S_e\rangle|S_n\rangle$. The electronic part depends only parametrically from the nuclear coordinates. If the electronic part of the total wave function is not changed by the scattering process, then the difference between the initial state $|I\rangle$=$|I_e\rangle|I_n\rangle$ and the final state $|F\rangle$=$|F_e\rangle|F_n\rangle$ is only due to excitations associated to atomic density fluctuations. Using these two hypotheses, one arrives from the correlation function of the electron density that is contained in Eq. 2.30 to the correlation function of the atomic density [73]:

$$\frac{d^2\sigma}{d\Omega dE_f} = r_0^2(\boldsymbol{\epsilon}_i \cdot \boldsymbol{\epsilon}_f)^2 \frac{k_f}{k_i} \left(\sum_{I_n,F_n} P_{I_n} \mid \langle F_n \mid \sum_l f_l(\mathbf{Q}) e^{i\mathbf{QR}_l} \mid I_n \rangle \mid^2 \delta(\hbar\omega - E_f - E_i) \right), \quad (2.31)$$

where $f_l(\mathbf{Q})$ is the atomic form factor of the atom l and $\mathbf{R}_l$ its position vector. The expression in the parenthesis $(...)$ contains the dynamical structure factor $S(\mathbf{Q},\omega)$. Assuming that the system contains N equal scattering units, then this expression can be simplified by the factorization of the form factor of these scattering units to:

$$S(\mathbf{Q},\omega) = \mid f(\mathbf{Q}) \mid^2 \frac{1}{2\pi\hbar N} \int_{-\infty}^{\infty} e^{-i\omega t} \langle e^{-i\mathbf{QR}_l(0)} e^{i\mathbf{QR}_{l'}(t)} \rangle dt. \quad (2.32)$$

Then the double differential cross-section can be rewritten as [73]:

$$\frac{d^2\sigma}{d\Omega dE_f} = r_0^2(\boldsymbol{\epsilon}_i \cdot \boldsymbol{\epsilon}_f)^2 \frac{k_f}{k_i} \mid f(\mathbf{Q}) \mid^2 S(\mathbf{Q},\omega) = \left(\frac{d^2\sigma}{d\Omega}\right)_{\text{Th}} \mid f(\mathbf{Q}) \mid^2 S(\mathbf{Q},\omega). \quad (2.33)$$

This expression is valid only for a system composed of equal scattering units, therefore, the coupling characteristics of the photons to the system (i.e. the Thomson scattering cross-section) are separated from the dynamical properties of the system, and the atomic form factor $f(\mathbf{Q})$ appears as a multiplication factor.

By substituting the atomic form factor with either the elementary cell form factor, or the molecular form factor, the expression can be generalized to describe crystalline and molecular systems. The expression for the $S(\mathbf{Q},\omega)$ depends on whether the system is crystalline or amorphous. For crystalline systems, the formalism for the inelastic structure factor is well established, and the symmetry considerations, as well as, the phonon selection rules are identical to the ones for INS.

The similarities and differences between the IXS and INS technique can be summarized as:

(i) X-rays couple to the electrons of the system with a cross-section proportional to r_0^2. The strength is comparable to the neutron-nucleus scattering cross-section b.

(ii) The IXS cross-section is proportional to $\mid f_l(\mathbf{Q}) \mid^2$. For $Q \to 0$ the form factor equals to Z (the number of electrons in the scattering atom). For increasing values of Q, the form factor decays. For INS the cross-section is proportional to b^2.

(iii) The total absorption cross-section of X-rays above 10 keV is limited in almost all cases ($Z > 4$) by the photoelectric absorption ($\sim \lambda^3 Z^4$), while for INS there is weak absorption.

(iv) In IXS there are no incoherent scattering contributions in contrast to INS.

(v) The beam size for IXS is $\leq$100 μm and the energy resolution about 1 meV. For INS the beam size is several centimetres and the energy resolution about 0.1 meV (for cold triple axis spectrometers).

(vi) The INS triple axis spectrometers resolution function is approximately Gaussian changing in ($\mathbf{Q}$, E)-space, while the IXS one is Lorentzian with long tails. For IXS measurements this can be a serious handicap for low energy excitations ($<$20 meV) due to the presence of elastic diffuse scattering.

Chapter 3

Experimental instruments

3.1 The neutron triple axis spectrometer

One instrument for measuring magnetic and lattice excitations in solids is the triple axis spectrometer (TAS). The TAS is using Bragg diffraction to prepare and analyze the neutron wave-length. The name of the spectrometer arises from the existence of three axes that are the important components of the instrument and can be rotated [69]. A sketch of a typical TAS is illustrated in Fig. 3.1. In order to select the proper neutron wave-length, according to Bragg's law ($n\lambda = 2d_{hkl}sin\theta$), the monochromator crystal as well as the sample table have to rotate around the first axis. Around the second axis the analyzer/detector unit can be rotated, whereby the sample scattering angle ϕ is selected with respect to the direction of the incident wave-vector k_i. Around the third axis, both the analyzer crystal and detector are rotated in order to select the desired wave-length of the scattered neutron beam. An additional rotation around the sample axis can be performed in order to scan any accessible plane in reciprocal space. Various components, such as collimators and filters, can be installed in order to improve the efficiency of a TAS. Collimators control the divergence of the neutron beam and can be installed in the incident and/or in the scattered beam. The collimation can improve the **Q** and E resolution of the instrument. Filters are installed to suppress higher order wave-lengths (arising from Bragg's law) from the monochromator and/or the analyzer. As a consequence, they also contribute in reducing the background and the spurious signal from the sample environment (cryostat, magnets etc.).

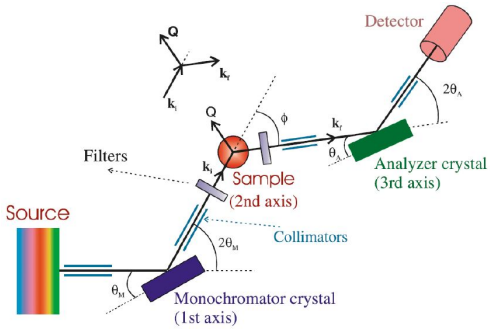

Figure 3.1: Sketch of a triple axis spectrometer (taken from [74]). The different components are described in the text.

In a single detector TAS one can access one point at the time in the $(\mathbf{Q}, \omega)$-space. This can be very time consuming, especially when the signal is weak and every point must be measured a long time. In order to cover larger portions in the $(\mathbf{Q}, \omega)$-space, multiplexing schemes have been employed to the secondary spectrometer (analyzer-detector). This is done by operating several analyzer-detector arms in parallel. As an example, the FlatCone multianalyzer setup that was used for measurements in this work is shown in Fig. 3.2 [75].

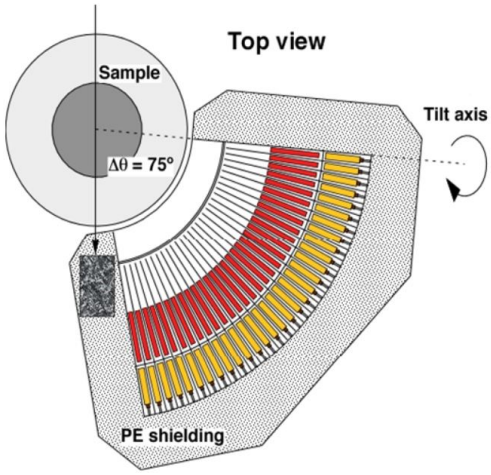

Figure 3.2: Sketch (courtesy of Dr. P. Steffens) of the FlatCone multianalyzer setup used at the Institut Laue Langevin (ILL) in Grenoble, France. The secondary spectrometer consists of 31 analyzers and detectors tubes.

With a TAS one performs for convenience two types of scans: (i) energy scans at constant $\mathbf{Q}$ or (ii) $\mathbf{Q}$ scans at constant energy transfer. For constant-$\mathbf{Q}$ scans, the spectrometer is set to a particular $\mathbf{Q}$, which is kept fixed during the scan and the energy transfer is changing. In constant-E scans the spectrometer is set to detect a particular energy transfer of the investigated excitation and $\mathbf{Q}$ is varied in a specific direction in reciprocal space (usually along a high symmetry direction). The choice between these two scans is dictated by the nature of the excitations, e.g. the slope in $(\mathbf{Q}, \omega)$-space of the investigated dispersion of the propagating modes. For the steeper parts of the dispersion constant-E scans are employed. For measurements close to the zone boundaries where dispersions become flat, usually constant-$\mathbf{Q}$ scans are preferred.

The observed intensity at a given $(\mathbf{Q}, \omega)$ depends not only on the scattering process from the sample but also on the instrument resolution. The measured intensity $I(\mathbf{Q}, \omega)$ is the convolution of the resolution function $F(\mathbf{Q}, \omega)$ and the scattering function $S(\mathbf{Q}, \omega)$: $I(\mathbf{Q}, \omega) = F(\mathbf{Q}, \omega) \otimes S(\mathbf{Q}, \omega)$. The resolution function $F(\mathbf{Q}, \omega)$, depends on the experimental configuration, such as the initial and the final energy, the mosaic spread of the sample (in case of single crystals), the monochromator and the analyzer, as well as the collimation used in the setup. In many neutron scattering experiments, taking into account the resolution effects is crucial in determining the intrinsic width and amplitude of an excitation. Computer programs are available nowadays that can perform the four-dimensional (three dimensions for $\mathbf{Q}$ and one for ω) convolution of the resolution function for a specific experimental configuration with a model, fit the result to the data, and finally give the model parameters, such as the intrinsic correlation lengths and

the lifetime of excitations [76].

The resolution ellipsoid is usually more elongated along one direction. This elongation is the basis for the focusing condition of the spectrometer as the widths of the observed peaks depend on the orientation of the ellipsoid with respect to the dispersion surface. For the focusing condition, the long axis of the ellipsoid is parallel to the dispersion curve, therefore the observed peaks will be more intense and narrower compared with the defocusing condition. This is shown in Fig. 3.3, for an upward dispersion curve. The focusing and the defocusing conditions can be determined from the instrument configuration [77].

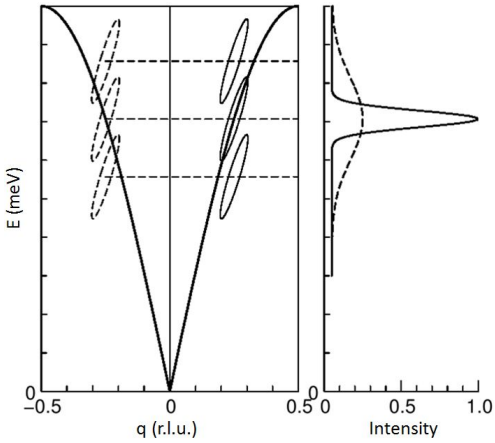

Figure 3.3: Effect of focusing (full line in the observed intensity) and defocusing conditions (dashed line in the observed intensity). If the resolution ellipsoid is adopted to the slope of the dispersion, the peak shape of the inelastic signal can be optimized (taken from [62]).

3.2 Polarized neutron scattering with triple axis spectrometer

In order to perform experiment with polarized neutrons, some modifications are necessary to the standard TAS setting (see Fig. 3.4). For polarizing experiments in some cases the monochromator can be used as a polarizer by selecting specific crystals. Good polarizing crystals, i.e. select neutron with a given spin state, are FM crystals where the nuclear structure factor ($F_N(\mathbf{Q})$) is similar to the magnetic structure factor ($F_M(\mathbf{Q})$). The differential cross-section for the general case of magnetized crystal is given by [69]:

$$\left(\frac{d\sigma}{d\Omega}\right)^{\pm\pm} = \left(F_N(\mathbf{Q}) \pm F_M(\mathbf{Q})\right)^2 . \tag{3.1}$$

If one can find a special reflection where $|F_N(\mathbf{Q})|=|F_M(\mathbf{Q})|$, then the diffracted neutron beam will be completely polarized. This is the case for the (111) reflection of the Heusler alloy Cu_2MnAl. The analyzer is made of the same material as the monochromator and operates the same way. Another way of polarizing the neutron beam is using magnetic multilayers with spin dependent transmission/reflection.

The directions of the spins in a neutron polarized experiment can be changed by flippers. The precession of the spin around a magnetic field is given by the Larmor angular frequency ω_L. If the magnetic field rotation ω_B is much smaller than ω_L, then the component of the polarization parallel to the magnetic field maintains its direction, while the perpendicular one processes around the magnetic field

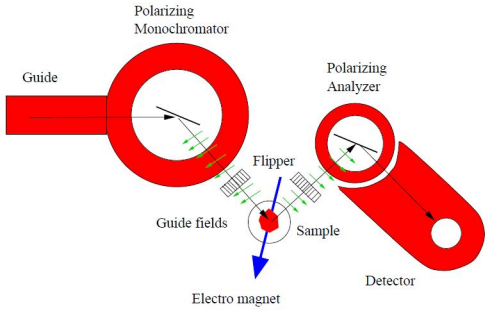

Figure 3.4: Sketch of a triple axis spectrometer in polarized mode (taken from [78]). The different components are described in the text.

(adiabatic case). If $\omega_L \ll \omega_B$, then the neutron spins will precess around the new field (non-adiabatic case). Mezei-flippers consist of a coil with a tuneable current. The current needed to turn the spin depends on the neutron velocity. A guide field is applied both before and after the coil. Before entering the coil the neutron spins are aligned along the guide field. When entering the coil the neutron spins are turned to a new direction. The guide field after the coil ensures that the neutron spins will maintain the new obtained direction. In order to access all four neutron spin cross-sections, it is necessary to install flippers on both sides of the sample (in the incident and in the scattered beam direction).

3.3 Inelastic X-ray scattering with ID28

The setup of the inelastic X-ray scattering beamline ID28 is shown in Fig. 3.5. After the premonochromatization, the initial energy is defined by a flat backscattering monochromator. In the backscattering geometry for X-rays the resolution of the initial wave-length depends on the properties of the monochromator crystal and is given by $\frac{\Delta\lambda}{\lambda} = \frac{\Delta d_{hkl}}{d_{hkl}} + cot\theta\Delta\theta \approx \frac{\Delta d_{hkl}}{d_{hkl}}$ for θ=89.98 °.

It can be shown that the resolving power is given by [73]: $\frac{\Delta E}{E} = \frac{d_{hkl}}{\pi\Lambda_{ext}}$, where d_{hkl} refers to the lattice spacing associated with the (hkl) reflection order and Λ_{ext} to the primary extinction length. Λ_{ext} increases with the reflection order of a perfect single crystal. A perfect single crystal can be defined as a periodic lattice without defects and/or distortions. A (13, 13, 13) reflection from a highly perfect silicon crystal can reach $\frac{\Delta E}{E} = 10^{-8}$. After further optical components, the photons are scattered from the sample and arrive in the analyzer. The energy resolution of the analyzer should be the same as the monochromator. The refocussed, energy-analyzed X-rays are detected by an inclined silicon diode detector. There are five independent analyzer systems with a fixed angular offset between them, mounted on a long arm that can rotate around a vertical axis of the sample. This rotation allows to select the scattering angle (θ_s) for the five analyzers and consequently the corresponding exchanged momentum $Q = 2k_i sin(\frac{\theta_s}{2})$.

In contrast to the TAS, due to the backscattering geometry, the energy difference between the analyzer and the monochromator cannot be changed by modifying the Bragg angle on one of the two crystals (analyzer(s), monochromator). The energy scans are performed by keeping the Bragg angle constant and by changing the relative temperature between the two crystals. The temperature change affects the relative lattice parameter and therefore the value of the reflected energies. The temperature of the analyzer is kept constant, while the temperature of the monochromator changes, and therefore E_i varies. Considering that

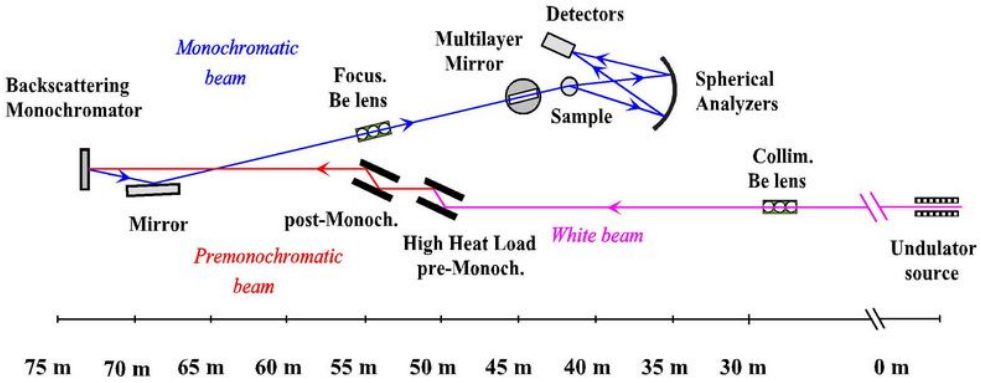

Figure 3.5: Setup of the inelastic X-ray scattering beamline ID28 at the European Synchrotron Radiation Facility (ESRF) (taken from [62]).

$\frac{\Delta E}{E} = \frac{\Delta d}{d} = \alpha \Delta T$ (α=2.58·10^{-6} K^{-1} for Si at room temperature), the temperature has to be controlled with a precision of 0.5 mK to obtain an energy step for about 1 tenth of the energy resolution.

Chapter 4

Spin dynamics of the magnetocaloric compound $MnFe_4Si_3$

4.1 Spin dynamics of localized and itinerant electron systems

For revealing microscopic ingredients that favour the MCE, which is enhanced around a magnetic phase transition, an investigation of the magnetic properties in the ordered phase ($T < T_C$), as well as, in the magnetically non-ordered state ($T > T_C$) is necessary. To this aim the spin dynamics of the MC compound $MnFe_4Si_3$ has been investigated above and below T_C as a function of the wave-vector $\mathbf{Q}$ and the energy E with INS in single crystals.

A magnetically ordered phase is described by the order parameter M (e.g. magnetization for a FM). In real systems magnetic fluctuations ($\langle \delta M \rangle$) occur. They describe the deviation of the magnetic moments from their average value. As the temperature approaches T_C (critical point) these fluctuations become important. Near the critical point in continuous phase transitions, the behaviour of a system can be described by power laws of the deviations of thermodynamic variables from their values at the critical point. Investigating the magnetic field response of the fluctuations around the critical point with INS might possibly point out major components at play for the MCE in $MnFe_4Si_3$.

Magnetism in solids originates from the magnetic moments of the atoms in the system. The magnetic moments are a consequence of the spin and angular momenta of the electrons. Two different models have been proposed to describe the magnetism in solids: the localized and the itinerant model. The behaviour of the spin-fluctuations is different for localized and itinerant electron systems. An empirical formula used to described the PM scattering function $S(\mathbf{Q}, \omega)$ is given by the double Lorentzian function [79, 80]:

$$S(\mathbf{Q},\omega) = \frac{1}{\pi}\frac{1}{1-e^{-\frac{\hbar\omega}{k_B T}}}\frac{\chi_0}{1+\left(\frac{q}{\kappa}\right)^2}\frac{\hbar\omega\Gamma_q}{\Gamma_q^2+\omega^2} = \frac{1}{\pi}\frac{1}{1-e^{-\frac{\hbar\omega}{k_B T}}}\chi_q\frac{\hbar\omega\Gamma_q}{\Gamma_q^2+\omega^2}, \tag{4.1}$$

where χ_q, Γ_q and κ are the q-dependent susceptibility, linewidth and inverse correlation length and χ_0 the static susceptibility.

In the case of localized magnetism the atoms constituting the solids have total angular momentum from spin and orbit from the electrons of each atom. The magnetic moments exist below and above the critical temperature and are confined to single atoms. The spins interact via quantum mechanical exchange interactions described by the Heisenberg model for magnetism ($H = \sum_{i,j} J_{ij} S_i S_j$). The q-dependent

linewidth can be approximated by [80]:

$$\Gamma_{\text{loc}}(q) = A_{\text{loc}} q^{2.5} f(\frac{\kappa^{\pm}}{q}), \tag{4.2}$$

where $f(\frac{\kappa^{\pm}}{q})$ represents the dynamical scaling function and $\pm$ refers to measurements above and below T_C. The dynamical scaling function equals to 1 at T_C and is a homogeneous function of $\frac{\kappa^{\pm}}{q}$ away from T_C. The inverse of the spin correlation length is given by the critical law [80]:

$$\kappa^{\pm} = \kappa_0^{\pm} \left(\frac{\mid T - T_C \mid}{T_C} \right)^{\nu}. \tag{4.3}$$

In this formula κ_0 refers to the inverse spin correlation length at T=0 K and the exponent ν equals to 0.5 and 0.7 for a Heisenberg model within the mean-field approximation and for critical scattering for Heisenberg spins (spins that have x, y and z component) in 3D, respectively.

In the itinerant case electrons are nearly free and are shared along the entire solid in an electron gas. Weak itinerant ferromagnets are characterized by small magnetic moments and the conduction electrons are mainly responsible for the magnetic properties of these materials. Exchange interaction causes a splitting between spin-up and spin-down density of states. Magnetic order appears when the total energy is reduced by this splitting. One simplified model to explain this is the Stoner model [65]. For weak itinerant ferromagnets the q-dependent linewidth is different when compared to a localized ferromagnet and is given by [80]:

$$\Gamma_{\text{wi}}(q) = A_{\text{wi}} q \left(1 + \left(\frac{q}{\kappa^{\pm}} \right)^2 \right). \tag{4.4}$$

4.2 Experimental details

The single crystal of $MnFe_4Si_3$ was grown by the Czochralski method [56] and two samples of this batch with a mass of about 7 g each were individually mounted on an aluminium sample holder and oriented in the (a*,c) and (a*,b*) scattering plane of the hexagonal lattice, respectively. The linewidths of the rocking curve of each sample consists of a single Gaussian peak and is of about 0.3 ° as measured by neutron diffraction.

INS measurements were carried out on the cold and thermal TAS IN12 [81] and IN22 at the Institut Laue Langevin (ILL), as well as on MIRA [82] and PUMA [83] at the Heinz Maier-Leibnitz Zentrum (MLZ). The spectrometers used for INS studies were setup in W configuration with a fixed final energy and a fully focusing setup. MIRA was used in elastic TAS mode with 60' secondary collimation. The corresponding integration in energy covers the range from -0.1 to 0.1 meV. Additional information regarding each configuration is given in Table 4.1.

For unpolarized INS measurements below T_C the sample was cooled down to the base temperature $T \approx$1.5 K with a ^{4}He flow cryostat or a closed cycle cryostat (configurations "A" and "B" in Table 4.1), while for measurements above T_C a cryofurnace was used to cover the temperature region of 80≤T≤500 K (configuration "C" in Table 4.1). Elastic measurements on MIRA were performed using a 2.2 T vertical field magnet with the field applied in the plane (configuration "F").

For INS measurements with polarized neutrons, the incident neutron beam spin state was prepared for IN12 with a transmission polarizing cavity [81] located after the velocity selector and for IN22 with a Heusler (Cu_2MnAl(111)) monochromator. All along the neutron path guide fields were installed to

Table 4.1: Instrument configurations. "PG" refers to pyrolytic graphite. Higher order contamination was removed using a PG filter in the scattered neutron beam on IN22 and PUMA. On IN12 and MIRA a velocity selector (VS) was employed before and a cooled Be filter after the monochromator, respectively. The symbol " * " refers to polarized setups.

Config.	TAS	Monoch.	Anal.	k_f (Å^{-1})	Filter
A	IN12	PG(002)	PG(002)	2	VS
B	PUMA	PG(002)	PG(002)	1.971	PG
C	IN12	PG(002)	PG(002)	1.3	VS
D	IN12*	PG(002)	$Cu_2MnAl(111)$	2	VS
E	IN22*	$Cu_2MnAl(111)$	$Cu_2MnAl(111)$	2.662	PG
F	MIRA	PG(002)	PG(002)	1.4	Be

maintain the polarization of the beam. In order to investigate the spin-wave scattering, the sample was placed in a 2.5 T vertical field magnet. The single crystal was first heated up above T_C to 316 K and then cooled down to 1.5 K under a vertical magnetic field of H_z=1 T applied parallel to the b-axis of the hexagonal system of the sample, corresponding to an axis within the easy plane of magnetization [56]. This results in a single domain state of the sample. The scattered beam was analyzed by a combination of a Mezei spin flipper and a horizontally focusing Heusler analyzer set at fixed k_f (configurations "D" and "E" in Table 4.1). The PM scattering was also investigated in detail at T=316 K using the spherical polarization analysis setup CRYOPAD [84] and configuration "E". For all measurements with polarized neutron beam (configurations "D" and "E") a flipping ratio ($F = \frac{\text{NSF}}{\text{SF}}$) of about 14 has been measured on a graphite sample.

4.3 Spin-wave scattering

The real and reciprocal space primitive translation vectors for a hexagonal Bravais lattice ($a = b \neq c$, $\alpha = \beta = 90\,^\circ$ and $\gamma = 120\,^\circ$) are given by:

$$\mathbf{a} \equiv \mathbf{a}_1 = \frac{\sqrt{3}a}{2}\hat{x} + \frac{a}{2}\hat{y}\,,\ \mathbf{b} \equiv \mathbf{a}_2 = -\frac{\sqrt{3}a}{2}\hat{x} + \frac{a}{2}\hat{y} \text{ and } \mathbf{c} \equiv \mathbf{a}_3 = c\hat{z} \tag{4.5}$$

$$\mathbf{a}^* \equiv \mathbf{b}_1 = \frac{2\pi}{\sqrt{3}a}\hat{x} + \frac{2\pi}{a}\hat{y}\,,\ \mathbf{b}^* \equiv \mathbf{b}_2 = -\frac{2\pi}{\sqrt{3}a}\hat{x} + \frac{2\pi}{a}\hat{y} \text{ and } \mathbf{c}^* \equiv \mathbf{b}_3 = \frac{2\pi}{c}\hat{z}. \tag{4.6}$$

A hexagonal Bravais lattice has as reciprocal lattice another hexagonal lattice with lattice constants $\frac{4\pi}{\sqrt{3}a}$ and $\frac{2\pi}{c}$ rotated through 30 $^\circ$ about the c-axis with respect to the direct lattice (see Fig. 4.1). The first Brillouin zone of the hexagonal lattice has also a hexagonal structure. The reciprocal lattice is generated by reciprocal lattice vectors $\mathbf{Q}_{(h,k,l)} = h\mathbf{a}^* + k\mathbf{b}^* + l\mathbf{c}^*$. The connection between the reciprocal latice vectors and real space lattice spacing for the hexagonal structure is given by:

$$\mid \mathbf{Q}_{(h,k,l)} \mid = \frac{2\pi}{d_{hkl}} = 2\pi\sqrt{\frac{4}{3a^2}(h^2 + hk + k^2) + \frac{l^2}{c^2}}. \tag{4.7}$$

In this chapter: **Q=G+q**, where **G** corresponds to a zone center, **Q**=(Q_h, Q_k, Q_l) is the scattering vector and **q**=(h, k, l) expresses the wave vector of an elementary excitation given in reciprocal lattice units (r.l.u.). All vectors are represented in hexagonal coordinates. Magnetic excitations of the MC compound $MnFe_4Si_3$ were measured mainly around the zone centers **G**=(2, 0, 0), **G**=(0, 2, 0) and **G**=(0,

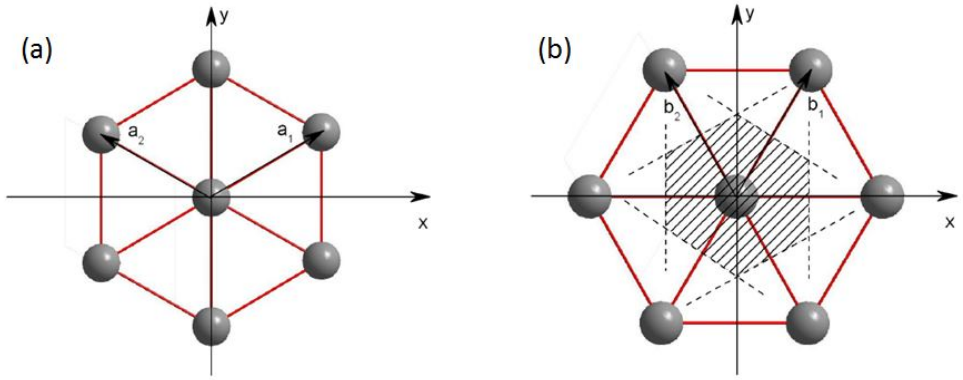

Figure 4.1: Sketch of a hexagonal lattice in (a) real and in (b) reciprocal space in xy plane. The shaded area indicates the first Brillouin zone.

0, 2) with configuration "A" and "B". There the calculated magnetic form factors for Fe and Mn are expected to have significant magnitude (see Fig. 4.2).

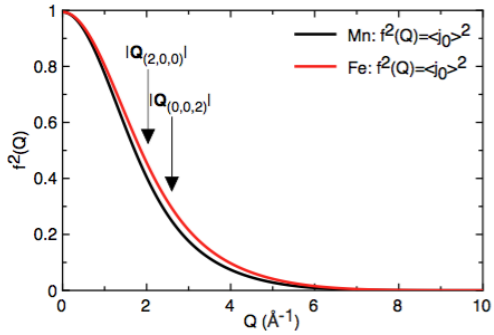

Figure 4.2: Magnetic form factors squared versus the modulus of the wave-vector $Q = \frac{4\pi}{\lambda} sin\theta$ for Mn and Fe. The $\langle j_0 \rangle$ integral is calculated using the parameters given in [85]. The arrows indicate the zone centers were magnetic excitations were measured for $MnFe_4Si_3$.

In order to extract acoustic magnon branches, constant energy and constant **Q** scans were carried out at energy transfers below 20 meV at T=1.5 K along the high symmetry reciprocal directions (h00), (hh0) and (00l) of the hexagonal system. Specific scans were repeated above T_C, e.g. at T=313 K, in order to establish the magnetic nature of the excitations. Typical representatives of such measurements are shown in Figs 4.3. In Fig. 4.3(a) the peak observed at T=1.5 K is replaced by a broad quasi elastic signal above the ordering temperature at T=313 K. It should be noted that the peak at T=1.5 K is extremely broad (FWHM=3.5(2) meV). The instrument resolution for this setting as computed with the software [76] is 1.2 meV. This broadening might be caused from strong spin-fluctuations at the WP 4d or from chemical disorder at the WP 6g [56]. In Fig. 4.3(b) only magnons are observed around the zone center **G**=(2, 0, 0) at Q_h=1.73 r.l.u. and Q_h=2.25 r.l.u., the former being more prominent due to the instrumental resolution focusing conditions. Around the zone center **G**=(3, 0, 0) two distinct peaks at Q_h=2.73 r.l.u. and Q_h=2.93 r.l.u. are attributed to spin-wave and phonon scattering, respectively. The peak observed in

the FM phase (T=1.5 K) at Q_h=2.73 r.l.u. (magnon) is replaced by an almost flat background in the PM state (T=313 K), while in contrast the peak at Q_h=2.93 r.l.u. (phonon) remains in the same Q_h position for the two different temperatures. The decrease of the magnon intensities in the two different zone centers that are in the focusing side of the spectrometer (Q_h=1.73 r.l.u. and Q_h=2.73 r.l.u.) is due to the decrease of the magnetic form factor $f(\mathbf{Q})$ with increasing $\mathbf{Q}$.

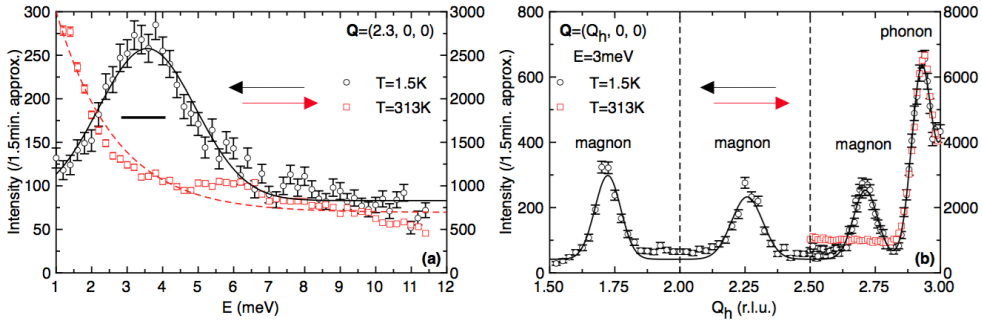

Figure 4.3: (a) Energy spectra at $\mathbf{Q}$=(2.3, 0, 0) and (b) $\mathbf{Q}$ spectra around $\mathbf{Q}$=(Q_h, 0, 0) at constant energy transfer of 3 meV measured at IN12 spectrometer with unpolarized setup (configuration "A") at 313 K (squares) and 1.5 K (circles). Neutron intensity for data at 1.5 K and 313 K is given on the left and right vertical axis, respectively. The solid lines correspond to fits with Gaussian functions and the dashed line is a guide for the eyes. The solid horizontal line on the left figure indicates the instrument resolution and the vertical dashed lines on the right figure the Brillouin zone boundaries.

Further experiments with polarized neutrons were performed along the (h00) and (00l) directions at 1.5 K using instrument configurations "D" and "E". Figs 4.4 show characteristic constant energy scans with polarized neutrons performed for an energy transfer of 5 meV around $\mathbf{Q}$=(2, 0, Q_l) (see Fig. 4.4(a)) and for an energy transfer of 4 meV around $\mathbf{Q}$=(Q_h, 0, 2) (see Fig. 4.4(b)).

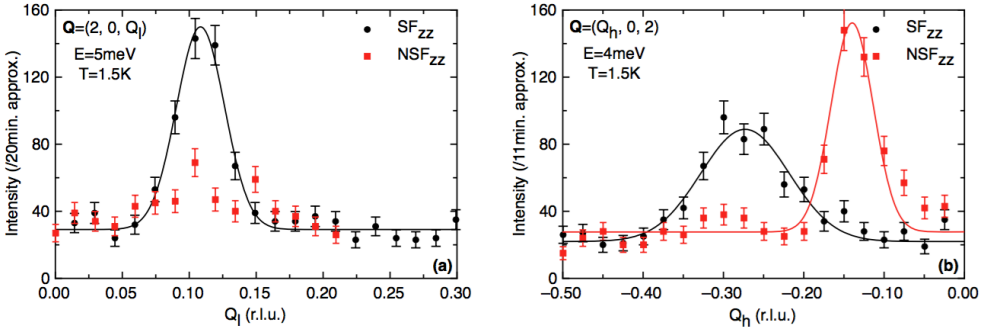

Figure 4.4: Polarized inelastic neutron scattering spectra obtained at IN12 (configuration "D") at T=1.5 K (a) around $\mathbf{Q}$=(2, 0, Q_l) at constant energy transfer of 5 meV and (b) around $\mathbf{Q}$=(Q_h, 0, 2) at constant energy transfer of 4 meV from spin flip and non-spin flip channel. The solid lines represent fits with Gaussian functions.

In Fig. 4.4(b) the peak observed in the spin flip (SF_{zz}) channel vanishes in the non-spin flip (NSF_{zz}) channel. The polarization is along the direction of the applied vertical magnetic field, z, which corresponds to the direction of the ordered magnetic moments in the single domain sample $MnFe_4Si_3$. Spin-waves

correspond to precession perpendicular to the ordered moment with therefore a unique component $\langle \delta M_y \rangle$ ($\langle \delta M_z \rangle$=0). In the crystal frame and for **Q** in the (a*,c) plane, the cross sections become (see Eq. 2.24 in Section 2.2.6.2):

$$\left(\frac{d^2\sigma}{d\Omega dE}\right)^z_{\text{NSF}} \propto BG_{\text{NSF}} + \langle N \rangle$$

$$\left(\frac{d^2\sigma}{d\Omega dE}\right)^z_{\text{SF}} \propto BG_{\text{SF}} + \langle \delta M_y \rangle = BG_{\text{SF}} + cos^2\theta \langle \delta M_c \rangle + sin^2\theta \langle \delta M_{a^*} \rangle,$$

with θ the angle between **Q** and the (h00) direction, $\langle N \rangle$ is the nuclear scattering and BG_{NSF} and BG_{SF} are the background in the NSF and SF channel, respectively. Consistently, the peaks observed at Q_l=0.11 r.l.u. and Q_h=-0.28 r.l.u. correspond to spin-wave scattering and the peak at Q_h=-0.13 r.l.u. to phonon scattering. Measurements with polarized neutrons are crucial in such a FM as acoustic phonon and magnon modes originate from the same Brillouin zone center. Moreover, all spectra were examined carefully for spurious scattering, especially aluminium and copper contamination, and the corresponding regions were masked during the data evaluation. Magnetic excitations, both for the constant **Q** and constant E scans, were fitted with Gaussian functions.

The obtained magnon dispersion along the main three symmetry directions ((h00), (00l) and (hh0)) is shown in Fig. 4.5. While the magnon branches are found to be rather isotropic in the two basal plane directions (h00) and (hh0), a much steeper dispersion develops along (00l). The experimental spin-wave spectrum at low energies ($E \leq 5$ meV) can be described by a quadratic dispersion $E=\Delta + D_{(hkl)}q^2$, where Δ is the energy gap, $D_{(hkl)}$ is the spin-wave stiffness and q is the momentum transfer. The obtained values are Δ=0.71(25) meV, $D_{(h00)}$=30(4) meVÅ^2, $D_{(hh0)}$=46(4) meVÅ^2 and $D_{(00l)}$=310(30) meVÅ^2 for the in and out-of plane magnon branch, respectively. The obtained value for the spin gap is within the instrument resolution, which is approximately 0.5 meV for configuration "A". Therefore, in the present study it is difficult to draw firm conclusions about the existence of a spin gap.

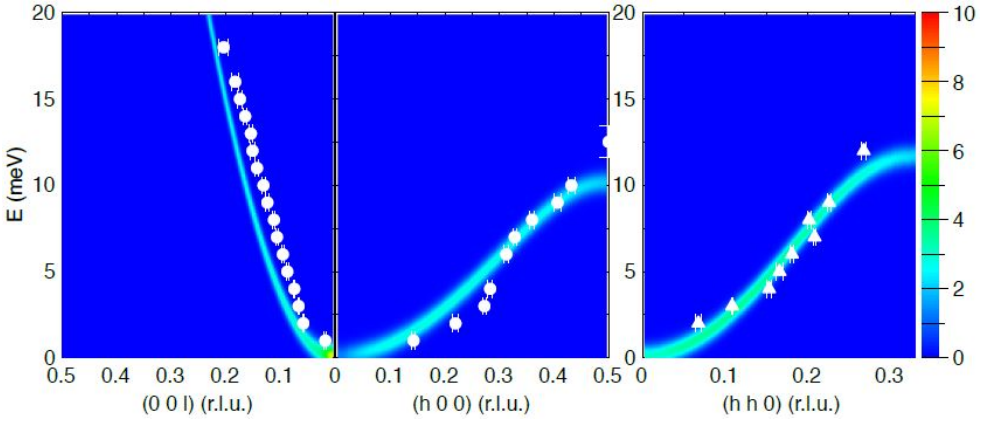

Figure 4.5: Magnon dispersion at T=1.5 K along (00l), (h00) and (hh0) directions from polarized (circles) and unpolarized (triangles) INS measurements. The colour-coded intensity corresponds to spin-wave simulation as described in the text.

To describe the spin-wave spectrum and to extract the relevant exchange interactions of this compound the SpinWave software package was used [86] (see also Appendix A.1). For the present study, the higher

symmetric $P6_3/mcm$ structure [47] proved to be a sufficient approximation. Since the experimental data revealed only the lower energy acoustic magnon dispersion for each direction, a simplified spin model was employed. Given the experimental uncertainty on the magnetic moment on the $4d$ site [56], one type of magnetic atoms carrying a spin S on the $6g$ sites of mixed occupancy was considered. As no significant differences are observed between the dispersion measured along the (h00) and (00l) directions at zero field and for H=1 T applied along the b-axis, one can assume for simplicity that the magnetic moments are lying along the b-axis. Furthermore the Zeeman effect is negligible being of the order of 0.09 meV for a magnetic moment of 1.5 μ_B under a magnetic field of 1 T. The spin model is described by a Heisenberg-type Hamiltonian, $H_H = \sum_{i,j} J_{ij} S_i S_j$, where J_{ij} denotes the exchange couplings between sites i and j.

The exchange interactions between the nearest neighbouring magnetic atoms located at WP $6g$ are shown in Fig. 4.6 and are described in Table 4.2. First, the coupling between magnetic atoms in the same distorted $[MnFe]_6$ octahedra are considered. This concerns $2SJ_0$, the exchange between the spins located on a triangle (distance 2.775 Å), $2SJ_2$ and $2SJ_3$ that couples two spin located on adjacent triangles separated by *c*/2 with distances 2.885 Å and 3.981 Å, respectively. Second, the exchange $2SJ_1$ concerns the shortest distance (4.304 Å) between spins located on adjacent distorted $[MnFe]_6$ octahedra. The experimental fact that the magnon dispersion is much steeper along the (00l) direction than in the basal plane, imposes that the exchange interaction with the highest ratio of out-of-plane to in-plane component, $2SJ_2$, is the dominant one. The second most important interaction concerning acoustic spin-waves is the one that connects the different octahedra, $2SJ_1$, which is mandatory to create the in-plane dispersion. The calculated dispersion using only the $2SJ_1$ and $2SJ_2$ interactions with the values indicated in Table 4.2 is shown in Fig. 4.5. This simplified model describes well the experimental dispersion and including further interactions is not relevant given the present set of data. In this respect, it should be pointed out that $2SJ_0$ does not participate in the out-of-plane dispersion by nature. The simulations show further that it does not contribute to the in-plane acoustic modes but only to the optic modes. Since these modes were not experimentally observed in the present study, $2SJ_0$ cannot be determined. In addition, it is found that the effect of $2SJ_3$ is redundant with the one of $2SJ_1$ and $2SJ_2$ and cannot be disentangled.

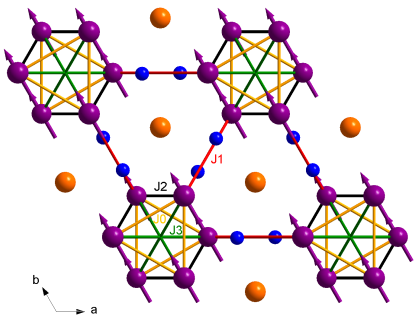

Figure 4.6: Projection on the hexagonal plane of the crystal structure of $MnFe_4Si_3$ in $P6_3/mcm$ space group. Sites occupied by Mn and Fe (WP $6g$, large purple) carry magnetic moments 1.5 μ_B parallel to b-axis, sites occupied by Fe (WP $4d$, large orange) and Si atoms (small blue) carry no magnetic moments. Yellow lines (J_0) connect atoms in the same plane, red lines (J_1), black lines (J_2) and green lines (J_3) in different planes.

Table 4.2: Exchange constant values, number of neighbours between magnetic sites (z_n), in-plane (IPP) and out-of-plane projections (OPP) of the vector linking the magnetic sites and distances between magnetic atoms (see Fig. 4.6). The symbol " − " means that the exchange interactions cannot be determined in the present work.

Exchange	value (meV)	z_n	IPP	OPP	Distance (Å)
$2SJ_0$	−	2	0.409	0	2.775
$2SJ_1$	−4	2	0.528	0.5	4.304
$2SJ_2$	−18	4	0.236	0.5	2.855
$2SJ_3$	−	2	0.472	0.5	3.981

4.4 Paramagnetic scattering

The spin dynamics of the MC compound $MnFe_4Si_3$ in the PM state was investigated with INS measurements, which were carried out with the scattering vectors along the (h00) and (00l) directions. For determining the extent of the spin-fluctuations in the PM region spectra have been collected with an unpolarized neutron beam at small q, using instrument configuration "C". The measured intensity was corrected by the Bose factor and a constant background was subtracted so that the obtained results correspond to the imaginary part of the dynamical spin susceptibility $\chi''(\mathbf{Q},\omega)$. A typical temperature dependence for **Q**=(0.25, 0, 0) for an energy transfer of E=0.3 meV is shown in Fig. 4.7(a). The spin-fluctuations show their maximum at T_C and extend for temperatures higher than $1.5T_C$. The inset in Fig. 4.7(a) shows the temperature dependence of the beam polarization P. Measurements were performed with the use of CRYOPAD and configuration "E" in non-spin flip NSF_{xx} and spin flip channel SF_{xx} at the **Q**=(0, 0, 2) Bragg peak. The calculated beam polarization was obtained by $P = \frac{NSF_{xx}-SF_{xx}}{NSF_{xx}+SF_{xx}}$ and equals to 86.6 % for T >305 K. It is clearly seen that a considerable beam depolarization occurs for $T \leq T_C$ due to the magnetic domain structure, indicating the transition from the PM state to the FM phase at T_C=305 K. Fig. 4.7(b) shows constant E spectra for an energy transfer of 1.5 meV around **Q**=(Q_h, 0, 0) at four different temperatures. The sharp peaks observed in the FM phase (T=80 K) at Q_h=1.8 r.l.u. and at Q_h=2.2 r.l.u. correspond to spin-waves. In the PM state the signal broadens as the temperature increases and the measured intensity is decreasing, consistently with Fig. 4.7(a). This is typical for PM scattering and indicates the diffusive nature of the spin-fluctuations. The ridges that are peaked at Q_h=2 r.l.u. and are present in the four different temperatures correspond to spurious scattering from the Bragg tail.

In order to get further insight into the spin dynamics near room temperature and above T_C, the PM scattering was studied at T=316 K corresponding to $1.036{\cdot}T_C$ along the (h00) and (00l) directions with constant **Q**-scans using instrument configuration "E". Spectra were collected in two non-spin flip channels NSF_{yy} and NSF_{xx} around the **G**=(2, 0, 0) and **G**=(0, 0, 2) zone centers. The magnetic fluctuations were extracted by taking the difference of intensity of the two non-spin flip channels taking into account higher order corrections of the monitor counts of each polarization channel. This gives access to the spin-fluctuations along the c-axis, $\langle \delta M_c \rangle$ (see Section 2.2.6.2 and below). A typical measurement is depicted in Fig. 4.8, where energy scans at **Q**=(2.2, 0, 0) and **Q**=(2.3, 0, 0) are shown. As expected the intensity decreases when q increases. The obtained spectra were convoluted with the 1D-instrument

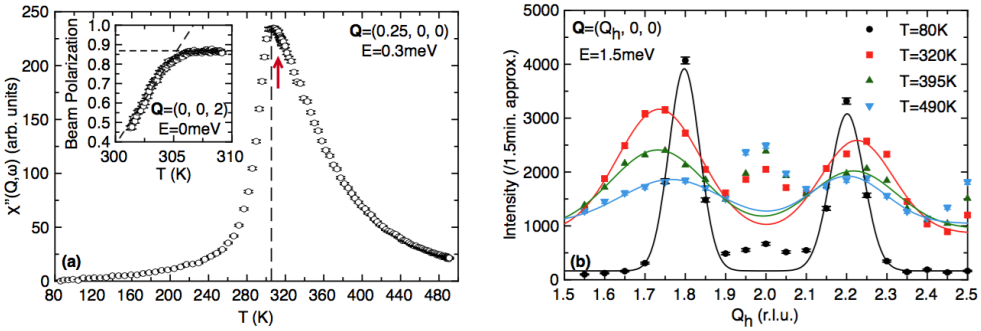

Figure 4.7: (a) Temperature dependence of dynamical spin susceptibility $\chi''(\mathbf{Q},\omega)$ at $\mathbf{Q}$=$(0.25, 0, 0)$ and E=0.3 meV. The dashed vertical line and the red arrow indicate T_C ≈305 K and $1.036T_C$ ≈316 K, respectively. The inset shows the temperature dependence of the beam polarization at $\mathbf{Q}$=(0, 0, 2) Bragg peak. (b) $\mathbf{Q}$ spectra around $\mathbf{Q}$=$(Q_h, 0, 0)$ at constant energy transfer of 1.5 meV at four different temperatures corresponding to the FM phase (80 K) and the PM state (320 K, 395 K, 490 K). The line at T=80 K corresponds to a fit with Gaussian functions and the lines connecting data points for the other temperatures are guides for the eyes. Spectra were measured with unpolarized neutrons at IN12 (configuration "C").

resolution and values for the q-dependent susceptibility χ_q and linewidth Γ_q were extracted as described below.

The measured intensity $I(\mathbf{Q},\omega)$ is the convolution of the resolution function $F(\mathbf{Q},\omega)$ and the scattering function $S(\mathbf{Q},\omega)$: $I(\mathbf{Q},\omega)$=$F(\mathbf{Q},\omega)\otimes S(\mathbf{Q},\omega)$. For simplicity one can assume for a signal not very strongly peaked in $\mathbf{Q}$-space that the resolution function is 1D in the ω direction and has a Gaussian shape with widths defined from measurements on a vanadium sample. The PM scattering function is given via Eq. 4.1. For all the obtained constant $\mathbf{Q}$ spectra at $1.036T_C$ ≈316 K (e.g. Fig. 4.8) the energy transfer was between -5≤E≤5 meV. For this energy range and temperature Eq. 4.1 is simplified to the double Lorentzian form:

$$S(\mathbf{q},\omega) = T\frac{\chi_0}{1+(q/\kappa)^2}\frac{\Gamma_q}{\omega^2+\Gamma_q^2} = T\chi_q\frac{\Gamma_q}{\omega^2+\Gamma_q^2}, \tag{4.8}$$

where ω and T are given in units of $\hbar$ and k_B, respectively. The resulting fit for the measured intensity $I(\mathbf{Q},\omega)$ can be realized as a Voigt function. From the Voigt's function amplitude χ_q can be extracted and the width of the Lorentzian part (HWHM) corresponds to Γ_q. The width of the Gaussian part is fixed to a constant value, defined from the vanadium sample measurement.

The obtained values for χ_q and Γ_q for (00l) and (h00) directions at 316 K are shown in Figs 4.9. χ_q decreases faster along the (00l) direction compared to (h00) indicating a shorter inverse correlation length. A Lorentzian fit for the q-dependent susceptibility χ_q gives values for the inverse correlation lengths κ_q: $\kappa_{(00l)}$=0.054(3) Å^{-1} and $\kappa_{(h00)}$=0.16(1) Å^{-1}. The energy range of the spin-fluctuations is of the same order of magnitude as the one of the spin-waves along these high symmetry directions. For q=0 the linewidth extrapolates to zero. In order to describe the experimental data for Γ_q at $1.036T_C$ two different models were used. For localized Heisenberg ferromagnets the linewidth of the magnetic fluctuations can be expressed as $\Gamma_q = A_{\text{loc}}q^{2.5}$ [80]. On the other hand for the weak itinerant model the expression is $\Gamma_q = A_{\text{wi}}q(1+(q/\kappa)^2)$, where κ refers to the inverse correlation length [80]. The obtained values for the

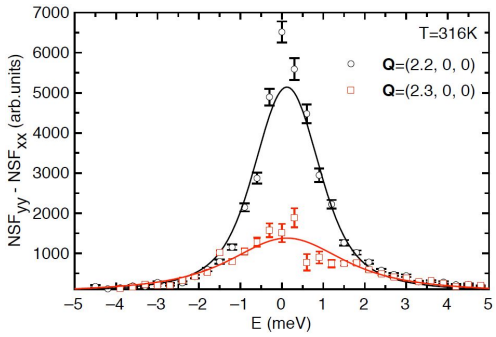

Figure 4.8: Spin-fluctuations $\langle \delta M_c \rangle$ obtained at IN22 (configuration "E") and measured at $\mathbf{Q}$=$(2.2, 0, 0)$ (black circles) and $\mathbf{Q}$=$(2.3, 0, 0)$ (red squares) at $1.036T_C$. Solid lines represent fits as explained in the text.

(00l) direction are $A_{\rm loc}$=183(6) meVÅ$^{2.5}$, $A_{\rm wi}$=1.3(5) meVÅ and $\kappa_{(00l)}$=0.054(12) Å^{-1} and for the (h00) direction $A_{\rm loc}$=24.6(5) meVÅ$^{2.5}$, $A_{\rm wi}$=0.80(22) meVÅ and $\kappa_{(h00)}$=0.16(3) Å^{-1}.

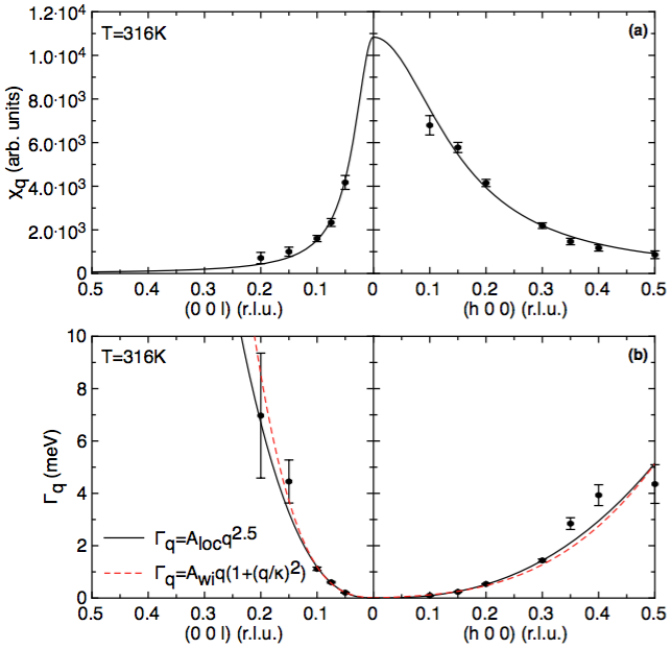

Figure 4.9: (a) q-dependent susceptibility χ_q and (b) linewidth Γ_q in the (00l) and (h00) directions at 316 K. The solid black lines for χ_q correspond to Lorentzian fits as described in the text. The solid black and dashed red line for Γ_q correspond to the localized and weak itinerant model of ferromagnetism, respectively.

Constant energy scans were performed for energy transfers $1.5 \leq E \leq 4$ meV along the directions (h00) and (00l) at 316 K in three non-spin flip channels NSF$_{xx}$, NSF$_{yy}$ and NSF$_{zz}$ around the $\mathbf{G}$=(2, 0, 0) and $\mathbf{G}$=(0, 0, 2) zone centers. For scattering vectors $\mathbf{Q}$ parallel to (h00), the scattering cross sections (see

Eq. 2.24 in Section 2.2.6.2) are for (a*,c) plane:

$$\left(\frac{d^2\sigma}{d\Omega dE}\right)^{x}_{\text{NSF}} \propto BG_{\text{NSF}} + \langle N\rangle$$
$$\left(\frac{d^2\sigma}{d\Omega dE}\right)^{y}_{\text{NSF}} \propto BG_{\text{NSF}} + \langle N\rangle + \langle \delta M_c\rangle$$
$$\left(\frac{d^2\sigma}{d\Omega dE}\right)^{z}_{\text{NSF}} \propto BG_{\text{NSF}} + \langle N\rangle + \langle \delta M_b\rangle$$

and for scattering vectors $\mathbf{Q}$ parallel to (00l), the scattering cross sections for (a*,c) plane become:

$$\left(\frac{d^2\sigma}{d\Omega dE}\right)^{x}_{\text{NSF}} \propto BG_{\text{NSF}} + \langle N\rangle$$
$$\left(\frac{d^2\sigma}{d\Omega dE}\right)^{y}_{\text{NSF}} \propto BG_{\text{NSF}} + \langle N\rangle + \langle \delta M_{a^*}\rangle$$
$$\left(\frac{d^2\sigma}{d\Omega dE}\right)^{z}_{\text{NSF}} \propto BG_{\text{NSF}} + \langle N\rangle + \langle \delta M_b\rangle.$$

Therefore, it is possible to determine the in-plane and out-of-plane components of the magnetic spin-fluctuations by using canonical subtraction of intensities measured in the different polarization channels. The results for the subtracted fluctuations for an energy transfer of 1.5 meV are shown in Figs 4.10. As can be seen the in-plane $\langle \delta M_b\rangle$ and the out-of plane fluctuations $\langle \delta M_c\rangle$ are found to be isotropic (Fig. 4.10(a)). The different in-plane component $\langle \delta M_{a^*}\rangle$ and $\langle \delta M_b\rangle$ are also isotropic (Fig. 4.10(b)). For this energy of 1.5 meV, the spectra show a maximum at a specific wave-vector **q**=(0.23, 0, 0) along (h00) and **q**=(0, 0, 0.08) along (00l) direction, respectively. This mimics the spin-wave dispersion. However the PM scattering is quasi-elastic, as can be seen in Figs 4.3(a) and 4.8, since there is no well-defined inelastic mode associated with a given wave-vector. Such "ridge" structure in ($\mathbf{Q}$, E)-space, i.e. maxima in constant-E spectra at finite q away from the Γ-point (see Figs 4.7(b) and 4.10) and maxima in constant-$\mathbf{Q}$ spectra for E=0 (Figs 4.3(a) and 4.8), is typical of PM scattering [80, 79]. One can also see that the peak widths are very anisotropic between the basal plane, where a broad peak spans the whole Brillouin zone (Fig. 4.10(a)) and perpendicular to the c-axis, where a narrow peak shape is found (Fig. 4.10(b)). The spectra measured at a constant energy of 1.5 meV were fitted by Lorentzian line shapes. The obtained effective inverse correlation lengths are $\kappa^*_{(h00)}$=0.161(2) Å^{-1} and $\kappa^*_{(00l)}$=0.0825(4) Å^{-1}. They compare well with the correlation lengths obtained through the q-dependence of the energy integrated PM scattering (see above and Fig. 4.9(a)).

The data shown in Figs 4.10 were fitted with Lorentzian functions independently of the parameters obtained by the analysis of the constant $\mathbf{Q}$-scans. An attempt to describe the spectra shown in Figs 4.11 by taking into account these parameters is described below. The out-of plane fluctuations $\langle \delta M_c\rangle$ along the (h00) direction and the in-plane fluctuations $\langle \delta M_b\rangle$ along the (00l) direction for three different energy transfers at T=316 K are shown in Figs 4.11(a) and 4.11(b), respectively. For both high symmetry directions the measured intensity is decreasing with increasing energy transfer, while the signal broadens, indicating the typical behaviour of the diffusive nature of the spin-fluctuations. Fitting the spectra with the general PM scattering function $S(\mathbf{Q},\omega)$ (see Eq. 4.1) with the linewidths expressed as $\Gamma_q = A_{\text{loc}}q^{2.5}$ and leaving all parameters free during the process, resulted to non realistic values for χ_0, A_{loc} and κ. To overcome this difficulty the amplitude was left as the only free parameter and the values for A_{loc} and κ for each direction were fixed to the ones obtained as described above expressed in meVr.l.u.$^{-2.5}$ and r.l.u.,

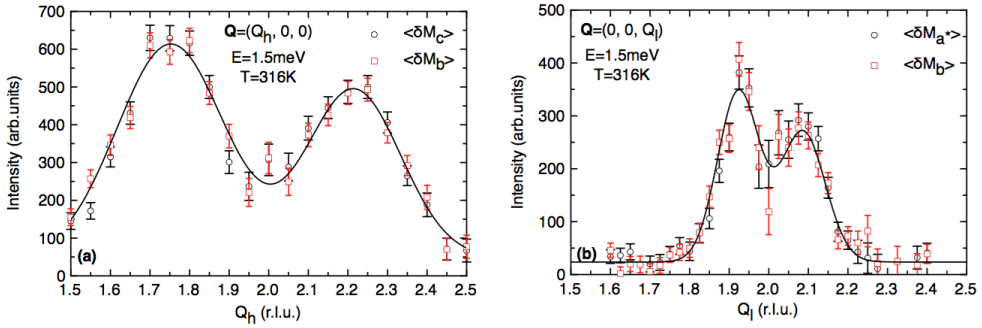

Figure 4.10: Subtracted spin-fluctuations spectra from constant energy scans at 1.5 meV at 316 K along (a) the (h00) and (b) the (00l) directions obtained at IN22 (configuration "E"). The indices i in $\langle \delta M_i \rangle$ indicates the direction of the spin-fluctuations (a^*, b and c). Solid lines correspond to fits with Lorentzian functions.

respectively ($A_{\rm loc}^{(h00)}$=29 meVr.l.u.$^{-2.5}$, $\kappa_{(h00)}$=0.15 r.l.u. and $A_{\rm loc}^{(00l)}$=375 meVr.l.u.$^{-2.5}$, $\kappa_{(00l)}$=0.041 r.l.u.). The obtained fits for each energy transfer and direction describe qualitatively well the experimental data. The observed disagreement between the data and the fits might be attributed to the fact that the scattering function (see Eq. 4.1) is not convoluted with the instrument resolution. Given this disagreement the 1.5 meV data shown in Figs 4.10 were fitted with Lorentzian functions.

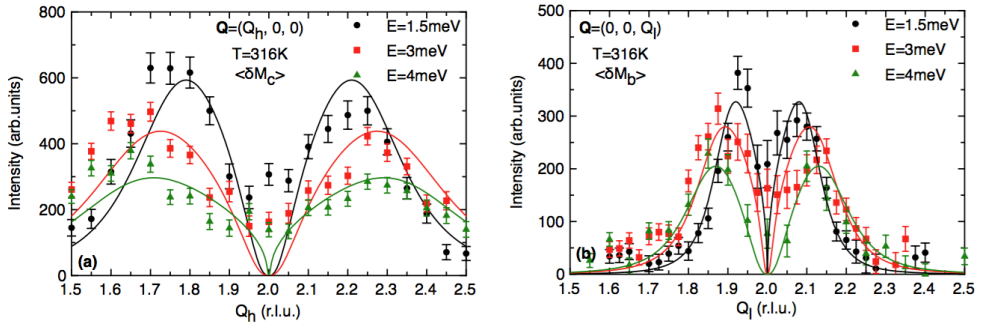

Figure 4.11: Subtracted spin-fluctuations spectra for different constant energy transfers at 316 K along (a) the (h00) and (b) the (00l) directions obtained at IN22 (configuration "E"). Solid lines correspond to fits as described in the text.

4.5 Spin dynamics under magnetic field

Fig. 4.12 shows the evolution of elastic scattering measured with configuration "F" as a function of magnetic field at three temperatures: close to T_C (300 K), above T_C (480 K) and below T_C (110 K) at the lowest accessible Q-range. In this very low Q-range the contribution to the intensity in the obtained spectra is attributed mainly to magnetic scattering. Consistently with Fig. 4.7(a), the magnetic scattering is significantly reduced at 110 and 480 K compared to 300 K. Around the critical temperature, a field of 2 T is sufficient to suppress the magnetic fluctuations. The spectra at 300 K are offset by the coercive field

(≈0.03 T) for ramping the magnetic field in positive or negative direction.

To get a qualitative description of the suppression of the magnetic fluctuations, the model of Ref. [87] was used and the calculated q-dependent susceptibility at T_C as a function of field is shown in the inset in Fig. 4.12. This model estimates the q-dependent susceptibility under a finite external magnetic field using the Landau theory for the magnetic fluctuations. In the vicinity of T_C the expressions of Ref. [87] are given by:

$$\left(\frac{\chi_q(0,T_C)}{\chi_q(H,T_C)} - 1\right)^3 = c\frac{P}{A^3}\frac{H^2}{q^6}, \tag{4.9}$$

where the constant c equals to 27 and 1 for the susceptibility parallel ($\chi_q^{\parallel}(H,T_C)$) and perpendicular ($\chi_q^{\perp}(H,T_C)$) to the field, respectively. The parameters P and A are constant in the critical region and are given by:

$$P = \frac{9}{10S^3(S+1)^3}\frac{V^3}{g^4\mu_B^4}k_BT_C$$
$$A = \frac{3V}{S(S+1)g^2\mu_B^2}\frac{k_BT_C}{\kappa_0^2},$$

where V refers to the volume of the cell and g to the Landé factor. The measurements shown in Fig. 4.12 probe the sum of the susceptibilities parallel and perpendicular to the magnetic field and are given by:

$$\chi_q^{\parallel}(H,T_C) = \frac{\chi_q(0,T_C)}{1+(\frac{27}{30})^{1/3}(\frac{\kappa_0}{q})^2(\frac{g\mu_BH}{k_BT_C})^{2/3}} \tag{4.10}$$

$$\chi_q^{\perp}(H,T_C) = \frac{\chi_q(0,T_C)}{1+(\frac{1}{30})^{1/3}(\frac{\kappa_0}{q})^2(\frac{g\mu_BH}{k_BT_C})^{2/3}}. \tag{4.11}$$

The field dependent susceptibility is calculated by inserting the parameters κ_0 obtained for ν=0.5 in Eq. 4.3 and by averaging the in and out-of plane correlation lengths (giving $(\frac{\kappa_0}{q})^2 \approx 100$). The obtained calculation is shown in the inset of Fig. 4.12 with an overall scale factor as the only free parameter. The calculated function describes qualitatively well the data, but the observed decrease with magnetic field is quantitatively stronger.

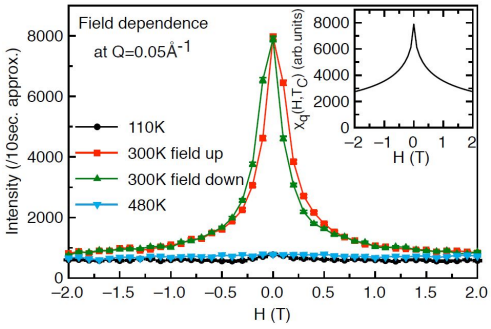

Figure 4.12: Evolution of elastic scattering at Q=0.05 Å^{-1} measured at MIRA (configuration "F") as a function of magnetic field at three temperatures. Lines can be used as guides for the eyes. The inset shows a calculation of the field dependence of $\chi_q(H,T_C)$ following Ref. [87].

4.6 Discussion

Polarized and unpolarized INS measurements performed on single crystals of the MC compound $MnFe_4Si_3$ reveal a strong anisotropy in the exchange interactions between the (h00) and (00l) directions of the hexagonal system, while the magnetic fluctuations (dynamical susceptibilities) in the PM state at T=1.036T_C=316 K are found to be isotropic. This anisotropy is reflected in the magnon spectrum as well as in the q-dependent linewidths Γ_q (see Figs 4.5 and 4.9(b)). The ratio of the spin-wave stiffness D and the constant $A_{\rm loc}$ for the two directions is about of the same magnitude $\left(D_{(00l)}/D_{(h00)}\right)$=10.3(1.7) and $\left(A_{\rm loc}^{(00l)}/A_{\rm loc}^{(h00)}\right)$=7.44(29). The obtained data at 1.5 K indicate that the magnetic exchange interactions within the basal plane between the (h00) and (hh0) directions are isotropic. The experimental data collected at 1.5K̇ could be well described by a Heisenberg-type Hamiltonian. In the used effective spin-wave model this translates into two FM exchange parameters with values $2SJ_2$=$-$18 meV and $2SJ_1$=$-$4 meV.

Strong anisotropy in the magnetic exchange interactions between the (h00) and (00l) directions has been reported for other FM compounds with hexagonal structure and lattice parameters comparable to $MnFe_4Si_3$ e.g. MnBi [88], MnSb [89, 90], MnP [91, 92] and Fe_2P [93]. Selected microscopic properties for representative hexagonal FM compounds are given in Table 4.3. A striking feature is the large value of $D_{(00l)}$ and the related strong anisotropy for $MnFe_4Si_3$. For the isostructural MnT FM (T= Bi, Sb, P) decreasing the size of the T-ion leads to a decrease of interatomic Mn-Mn distance resulting in lower magnetic moments and Curie temperatures. This behaviour might be attributed to a systematic shift from dominant itinerant to short-range exchange interactions with decreasing size of the T-ion [88]. In $MnFe_4Si_3$ the magnetic atoms that carry moments in WP 6g, which has a mixed occupancy of Mn and Fe, have an interatomic shortest nearest neighbours distance of ≈2.775 Å comparable to MnP. This could hint to short range exchange magnetic interactions in $MnFe_4Si_3$.

Table 4.3: Properties of selected ferromagnetic materials with hexagonal structure. Lattice parameters are given at around 300 K. M_s refers to the saturated magnetic moments. For MnP compound the parameters are given in the distorted hexagonal NiAs-type structure. The lattice parameters for $MnFe_4Si_3$ are the ones obtained in the present study and are in agreement with Ref. [56].

Compound	T_C (K)	M_s μ_B	a (Å)	c (Å)	c/a	$D_{(h00)}$ (meVÅ^2)	$D_{(00l)}$ (meVÅ^2)	$D_{(00l)}/D_{(h00)}$	Easy axis of magnetization
Fe_2P [93, 95, 96]	209	1.46	5.88	3.44	0.585	42	76	1.81 (at 77 K)	c
MnP [91]	292	1.33	3.17	5.26	1.659	70	145	2.07 (at 150 K)	a
$MnFe_4Si_3$	305	1.5	6.78	4.72	0.696	30	310	10.3 (at 1.5 K)	b

Further insight can be gained from the calculation of the correlation lengths. The order of the FM transition is not clarified and since experimentally no discontinuity of the temperature dependence of magnetization was reported [56, 59] and strong critical fluctuations are observed (Fig. 4.7(a)), the inverse of the spin correlation length κ can be assumed to follow the critical law of Eq. 4.3. The calculated values κ_0 for ν=0.5 result to: $\kappa_0^{(h00)}$=0.86(5) Å^{-1} and $\kappa_0^{(00l)}$=0.284(16) Å^{-1} and for ν=0.7 to: $\kappa_0^{(h00)}$=1.7(1) Å^{-1} and $\kappa_0^{(00l)}$=0.55(3) Å^{-1}. One alternative model for calculating the inverse spin correlation lengths κ_0 by taking into account the spin-wave stiffness and the transition temperature is the following [79]:

$$\kappa_0 = \sqrt{\frac{3k_BT_C}{(S+1)D}}, \tag{4.12}$$

which gives $\kappa_0^{(h00)}$=1.15(8) Å^{-1} and $\kappa_0^{(00l)}$=0.357(17) Å^{-1}. These values are of the same order of magnitude as the ones obtained by Eq. 4.3. It is clearly seen that the corresponding correlation lengths ξ_0=κ_0^{-1} (for ν=0.5: $\xi_0^{(h00)}$=1.16(7) Å and $\xi_0^{(00l)}$=3.5(2) Å and for ν=0.7: $\xi_0^{(h00)}$=0.59(3) Å and $\xi_0^{(00l)}$=1.8(1) Å) are smaller than the lattice parameters a and c, which points to a localized feature of the magnetism of $MnFe_4Si_3$. On the other hand for itinerant magnetic systems ξ_0 are expected to be significantly larger [79, 80].

Additional information can be given by the linewidths Γ_q. The experimental data for the Γ_q obtained at 316 K for the (h00) and (00l) directions could be well described both with a model for localized Heisenberg ferromagnets ($\Gamma_q = A_{\text{loc}} q^{2.5}$) as well as a model for weak itinerant ferromagnets ($\Gamma_q = A_{\text{wi}} q(1+(q/\kappa)^2)$). The difficulty to distinguish between both models near T_C was reported previously for Ni_3Al [94].

The maximum value for Γ_q in the zone boundary (q=0.5 r.l.u.) for each direction is $\Gamma_{\text{loc,max}}^{(h00)}$=5.15(12) meV and $\Gamma_{\text{loc,max}}^{(00l)}$=62(2) meV, which means that the overall $\langle\Gamma_q\rangle$ is not expected to be higher than $2k_BT_C$. Based on the fact that the characteristic linewidths are higher than k_BT_C one could expect an itinerant contribution to the magnetism. This is in agreement with Ref. [56], where the Rhodes-Wohlfarth model for the ratio of magnetic moments obtained from the Curie-Weiss law (M_c) to the low temperature saturation magnetization (M_s), M_c/M_s=1.7 points to itinerant magnetism.

Based on the Heisenberg model and the molecular field approximation the Curie temperature T_C^{MF} can be calculated by [80]:

$$T_C^{\text{MF}} = \frac{2S(S+1)}{3k_B} \sum_n J_n z_n, \tag{4.13}$$

where z_n is the number of the nth neighbours. Using Table 4.2 one can calculate the minimum T_C^{MF} assuming that there are no strong AF interactions between second, third, etc. nearest neighbours. The calculated value is giving T_C^{MF}=619 K leading to the ratio $T_C^{\text{MF}}/T_C \approx 2$. This ratio is typical for a ferromagnetic metal pointing to the existence of spin-fluctuations beyond the molecular field approximation and is also confirmed by the typical value of $\langle\Gamma_q\rangle$ with respect to T_C.

Short range magnetic correlations in the PM state were also observed in Fe_2P-based MC materials [97] and their importance for the MCE is not clearly demonstrated. However, the present study shows that the temperature and the magnetic field ranges, where the change of entropy is sizeable, matches the ones where the magnetic fluctuations are either critical (near T_C) or suppressed (near H=2 T). This points to the importance of such fluctuations for the MCE. In particular, the critical scattering observed near T_C is strongly suppressed by a magnetic field of 2 T. The calculated function (see inset in Fig. 4.12) describes qualitatively well the data, but the observed decrease with magnetic field is quantitatively stronger. Such disagreement could be attributed to different reasons: the finite integration in energy of our data (-0.1$\leq E \leq$0.1 meV), the isotropic nature of spin correlations in the model of Ref. [87] or a fluctuations pattern beyond the Landau theory. Since such studies on the effect of a magnetic field on the critical fluctuations are scarce, it is difficult to draw firm conclusions. The same model was used to describe the suppression of the critical fluctuations in Gd [98] and here also the agreement is semi-qualitative. In this context, further studies on the effect of the magnetic field on the magnetic critical fluctuations are necessary regarding their potential importance for the MCE.

4.7 Conclusions

In this study the obtained correlation lengths and linewidths point to both itinerant and localized contributions of the magnetism in the MC compound $MnFe_4Si_3$, a behaviour typical of many ferromagnets [80]. This detailed study of the spin dynamics of the MC compound $MnFe_4Si_3$ provides key microscopic information concerning the nature of the magnetism in this system. Among the specific features highlighted are the isotropic dynamical spin susceptibilities in the PM state, strong anisotropy between in and out-of plane magnetic exchange interactions, short range correlation lengths compared to typical distances and extended characteristic linewidths compared to T_C. So far it is not clear which ingredient is favourable to produce a large MCE. These results suggests that the strong response of the critical fluctuations in the PM state to a magnetic field of 2 T is an important feature. Thus a systematic study of the spin dynamics of various MC compounds in order to highlight the major components at play and to finally optimize the materials in view of applications is highly needed.

Chapter 5

Unravelling the underlying mechanisms of the inverse magnetocaloric compound Mn_5Si_3

5.1 Inverse magnetocaloric compounds

As described in Section 1.2, cooling by adiabatic demagnetization using materials that exhibit giant MCEs near room temperature magneto-structural phase transitions can be potentially used for magnetic refrigeration applications in daily life. Alternatively, in some compounds cooling can be achieved by adiabatic magnetization, a less common effect, the inverse MCE. The discovery of large inverse MCE around room temperature has attracted interest since it provides added flexibility in the material and functional device design [36, 39]. The inverse MCE potentially occurs in any PM to AF phase transition [99, 100]. However, this effect is usually not large and systems in which the inverse MCE is of interest undergo a first-order magnetic transformation between distinct magnetic phases. Representative examples of inverse MCE compounds are to be found in AF to ferrimagnetic (FI) transitions (e.g. $Mn_{1.95}Cr_{0.05}Sb$ [43], $Mn_{1.82}V_{0.18}Sb$ [101]), in AF to FM transitions (e.g. $Fe_{0.49}Ni_{0.51}$ [102], Mn_3GaC [103], DySb [104]), in austenite to martensite transitions in FM Heusler alloys (e.g. $Ni_{0.50}Mn_{0.50-x}Sn_x$ [36]) and in collinear to non-collinear AF transitions like in Mn_5Si_3 [46], the subject of this chapter.

Both the crystal and the magnetic structure of Mn_5Si_3 were described in detail in Section 1.3.2. The magnetic structure of Mn_5Si_3 for $66 \leq T \leq 100$ K (AF2 phase) consists of collinear antiparallel arrangements of magnetic moments, while below 66 K (AF1 phase) the orientation of the magnetic moments becomes highly non-collinear and non-coplanar due to magnetostructural distortion. The crystal structure of the two AF phases can be described with an orthorhombic cell (space group $Ccmm$ and $Cc2m$ for the AF2 and AF1 phase, respectively). The inverse MCE in this compound is detected in the vicinity of the AF1-AF2 phase transition and it should be noted that the negative sign of the MCE has only been observed in the range where non-collinear magnetic structures prevail. According to Ref. [43], it is speculated that an applied magnetic field decouples some of the antiparallel aligned magnetic moments of the AF1 phase which results in increasing disorder of the spin system, raising the magnetic entropy.

Up to nowadays the magneto-thermodynamic effects for materials that exhibit the direct, as well as the inverse MCE are experimentally studied mostly by bulk measurements, e.g. specific heat and magneti-

zation as a function of T and H, which quantify the MCE and provide a basis for a phenomenological description. However, the microscopic mechanisms at play are to be revealed and the key ingredients are to be identified. The present microscopic investigation using as probe INS, will attempt to address the dynamical magnetic response, which is at the origin of magneto-thermodynamic effects .

5.2 Experimental details

For synthesising polycrystalline samples of Mn_5Si_3, elementary manganese (Aldrich, 99.99 %) and silicon (Aldrich, 99.99 %) were used. The manganese pieces were etched prior to the synthesis in hydrochloric acid to obtain a clean unoxidized surface. All raw materials were heated under vacuum to remove remaining impurities, such as surface water. The elements were mixed in stoichiometric ratios and melted in argon atmosphere by induction heating in a levitation cold crucible. The resulting product was cooled and heated four times to ensure maximum homogeneity of the sample. In order to confirm the formation of the Mn_5Si_3 phase, part of the polycrystalline sample was characterized by X-ray powder diffraction at room temperature.

Once the the formation of the Mn_5Si_3 phase was confirmed, a single crystal was grown from the polycrystalline samples using the Czochralski method in an aluminum oxide crucible with a tungsten crystal as seed. The final single crystal had a diameter of about 13 mm and was cut by spark erosion into two large single crystal samples of about 7 g each. These single crystals were mounted on an aluminium sample holder and oriented in the (a,b) and (b,c) scattering plane of the orthorhombic symmetry, respectively. The linewidths of the rocking curves of the samples consist of single Gaussian peaks of widths of about 1.25 ° as measured by neutron scattering. In order to reduce the scattering of the aluminium sample holder a cadmium foil was placed around it.

INS measurements were carried out on the cold and thermal TAS ThALES, IN12, IN20 and IN22 at the Institut Laue Langevin (ILL), as well as on 2T1 at the Laboratoire Léon Brillouin (LLB). All spectrometers used for INS studies were setup in W configuration with a fixed final energy. Focusing setups were employed for all spectrometers except IN22 were the analyzer was set flat. Additional information regarding each configuration is given in Table 5.1.

Table 5.1: Instrument configurations. Higher order contamination was removed using a velocity selector (VS) before the monochromator on ThALES and IN12 and a PG filter in the scattered neutron beam on IN20, IN22 and 2T1. The symbol " * " refers to polarized setup.

Config.	TAS	Monoch.	Anal.	k_f (Å^{-1})	Filter
G	ThALES	Si(111)	Si(111)	1.4	VS
H	IN12	PG(002)	PG(002)	1.5, 1.8, 2	VS
I	IN20	Si(111)	PG(002)	2.662, 4.1	PG
J	IN22	PG(002)	PG(002)	2.662	PG
K	2T1	PG(002)	PG(002)	2.662	PG
L	IN12*	PG(002)	Cu_2MnAl(111)	1.8	VS

For unpolarized INS measurements below room temperature, the sample was cooled down with a ^{4}He flow cryostat (for TAS at ILL) or a closed cycle cryostat (for TAS at LLB), covering the temperature region of $10 \leq T \leq 120$ K. In order to map extended ranges of the ($\mathbf{Q}$, E)-space the FlatCone multianalyzer

option [75] was used (configuration "G" in Table 5.1). The rotation step width of the sample was 0.5 ° and the measuring time per step 2 minutes.

Spin dynamics investigations with unpolarized neutrons under magnetic field were carried out using a 10 T vertical field magnet. The single crystal was oriented in the (a,b) scattering plane of the orthorhombic structure and the analyzer was set at fixed k_f=1.8 Å^{-1}. The field was applied along the c-axis (configuration "H" in Table 5.1) and 80'-open-open collimations were installed.

Polarized INS measurements were performed with configuration "L" in Table 5.1, using the spherical polarization analysis setup CRYOPAD [84]. The incident neutron beam spin state was prepared with a transmission polarizing cavity located after the velocity selector [81]. All along the neutron beam path guide fields were installed to maintain the polarization of the beam. A flipping ratio of about 14 has been determined from a graphite sample.

5.3 Preliminary measurements

Preliminary INS experiments with unpolarized beam were performed at IN12 spectrometer with configuration "H" (see Table 5.1) and the analyzer set at fixed k_f=1.5 Å^{-1}. The single crystal was oriented in the (a*,b*) scattering plane of the hexagonal symmetry at room temperature. During cooling the reduction of symmetry from hexagonal to orthorhombic due to the onset of long-range magnetic order was not observed [105]. This could be attributed to the small changes of the lattice parameters [105] and the poor resolution of TAS IN12 compared to a single crystal diffractometer. Once the sample reached base temperature, the lattice parameters were readjusted with elastic measurements at (2, 0, 0) and (0, 2, 0) Bragg positions and the single crystal was realigned in the hexagonal symmetry.

Spectra at constant energy transfers were collected in the AF1 phase at T=1.5 K and excitations were measured around the Bragg positions ($\frac{3}{2}$, 0, 0) and (2, 0, 0). Such typical measurements are shown in Fig. 5.1(a). In an antiferromagnet with non-zero propagation vector as Mn_5Si_3, acoustic phonons and magnons originate from different zone centers. Consistently, magnons originate from the magnetic zone center ($\frac{3}{2}$, 0, 0), while phonons originate from the structural zone center (2, 0, 0) [105, 106].

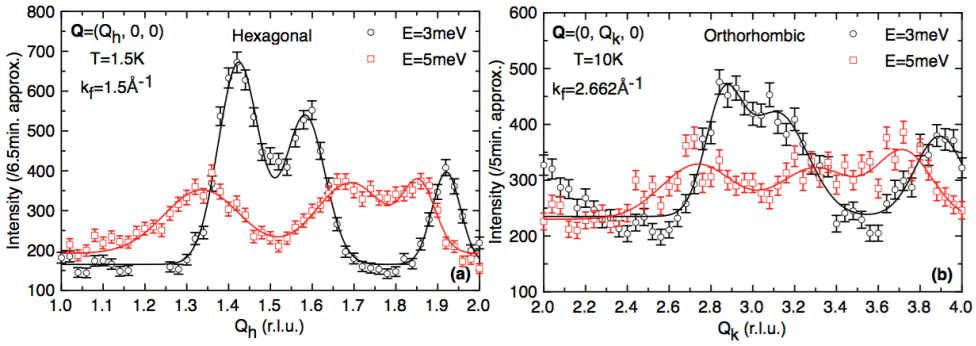

Figure 5.1: Unpolarized inelastic neutron scattering spectra at constant energy transfer of 3 and 5 meV obtained at (a) IN12 and (b) 2T1 in the AF1 phase of Mn_5Si_3. The equivalence between the hexagonal and the orthorhombic symmetry is described in the text. The solid lines correspond to fits with Gaussian functions.

The hexagonal symmetry (PM state) of Mn_5Si_3 can be described with an ortho-hexagonal (orthorhombic) cell with three possible choices, which can be derived from the following expressions:

$$\mathbf{a}_{\rm o}^{\rm I} = \mathbf{a}_{\rm h}, \mathbf{b}_{\rm o}^{\rm I} = \mathbf{a}_{\rm h} + 2\mathbf{b}_{\rm h}, \mathbf{c}_{\rm o}^{\rm I} = \mathbf{c}_{\rm h} \tag{5.1}$$

$$\mathbf{a}_{\rm o}^{\rm II} = \mathbf{b}_{\rm h}, \mathbf{b}_{\rm o}^{\rm II} = -2\mathbf{a}_{\rm h} - \mathbf{b}_{\rm h}, \mathbf{c}_{\rm o}^{\rm II} = \mathbf{c}_{\rm h} \tag{5.2}$$

$$\mathbf{a}_{\rm o}^{\rm III} = -\mathbf{a}_{\rm h} - \mathbf{b}_{\rm h}, \mathbf{b}_{\rm o}^{\rm III} = \mathbf{a}_{\rm h} - \mathbf{b}_{\rm h}, \mathbf{c}_{\rm o}^{\rm III} = \mathbf{c}_{\rm h} \tag{5.3}$$

In what follows in the present study and for being consistent with the more recent single crystal diffraction data [49, 51, 52] the ortho-hexagonal representation of the cell derived from Eq. 5.1 will be used. The transformation from the hexagonal to the corresponding ortho-hexagonal reciprocal coordinates is given through the matrix:

$$\begin{pmatrix} h_{\rm o}^{\rm I} \\ k_{\rm o}^{\rm I} \\ l_{\rm o}^{\rm I} \end{pmatrix} = \begin{pmatrix} 1 & 0 & 0 \\ 1 & 2 & 0 \\ 0 & 0 & 1 \end{pmatrix} \begin{pmatrix} h_{\rm h} \\ k_{\rm h} \\ l_{\rm h} \end{pmatrix} \tag{5.4}$$

The ortho-hexagonal cell dimensions are related to those of the hexagonal cell by $a_{\rm o}$=$a_{\rm h}$, $b_{\rm o}$=$\sqrt{3}a_{\rm h}$ and $c_{\rm o}$=$c_{\rm h}$. The lattice parameters of Mn_5Si_3 are a=6.88 Å, b=11.91 Å and c=4.81 Å at 10 K. The scattering vector $\mathbf{Q}$ is expressed in Cartesian coordinates $\mathbf{Q}$=(Q_h, Q_k, Q_l) given in reciprocal lattice units (r.l.u.). The wave-vector $\mathbf{q}$ is related to the momentum transfer through $\hbar\mathbf{Q}$=$\hbar\mathbf{G}$+$\hbar\mathbf{q}$, where $\mathbf{G}$ is a Brillouin zone center and $\mathbf{G}$=(h, k, l).

Below T_{N_2} the onset of long-range magnetic order reduces the crystal symmetry to orthorhombic and the relations written above between ($a_{\rm o}$, $b_{\rm o}$, $c_{\rm o}$) and ($a_{\rm h}$, $b_{\rm h}$, $c_{\rm h}$) lattice parameters hold approximately. Every structural peak in the (a, b) plane is the superposition of three peaks, that are generated from three equivalent orthorhombic cells. Within the TAS instrumental resolution, these three peaks are not resolved. By adding and subtracting the propagation vector, one can find two magnetic peaks in the coordinate system of each orthorhombic cell. The overall pattern of the magnetic peaks around the structural Bragg positions maintains an approximate sixfold symmetry, since the three orthorhombic cells are generated from one initial cell with hexagonal symmetry.

In Fig. 5.1(b) one can see INS spectra where the orthorhombic representation of the cell is used. Spin-waves and phonons originate from the magnetic and structural zone center (0, 3, 0) and (0, 4, 0), respectively. The differences in the lineshapes of the spectra measured in the two equivalent symmetries in Figs 5.1 is attributed to resolution effects between the IN12 and 2T1 spectrometers. However, the peak positions of the elementary excitations as found from Gaussian fits are in quantitative agreement between the two symmetries e.g. $\mathbf{q}_{\rm h}$=(0.09, 0, 0) and $\mathbf{q}_{0}$=(0, 0.18, 0) for the magnons for E=3 meV.

5.4 Determination of phonon and spin-wave dispersion curves in the non-collinear AF1 phase

For extracting the magnon and the phonon branches, constant energy and constant $\mathbf{Q}$ scans with unpolarized neutrons were carried out at energy transfers below 30 meV at T=10 K along the high symmetry directions (0k0) and (00l) of the orthorhombic symmetry. $\mathbf{Q}$-scans for $3 \leq E \leq 7$ meV are added up to a colour map and are shown in Fig. 5.2(a). The magnetic and phonon excitations that originate from different Bragg positions, seem to cross at $\mathbf{Q}$=(0, 3.5, 0) at about E=6 meV and for higher energy transfers

it is not easy to distinguish the individual branches. However, this observation might be misleading since the use of polarized neutrons was not employed. In order to overcome this difficulty and to drive firm conclusions concerning the dispersion curves of the phonons and the spin-waves, measurements were performed around zone centers where only one type of excitation was observed. Such measurements are depicted in Fig. 5.2(b) where the longitudinal acoustic (LA) phonons originate from the structural center **G**=(0, 0, 2), while no modes were observed from **G**=(0, 0, 1) and **G**=(0, 0, 3) (structural zone centers with $l \neq 2n$ are not allowed in the space groups $P6_3/mcm$, $Ccmm$ and $Cc2m$ [107], see also Table 1.1 in Section 1.3.2).

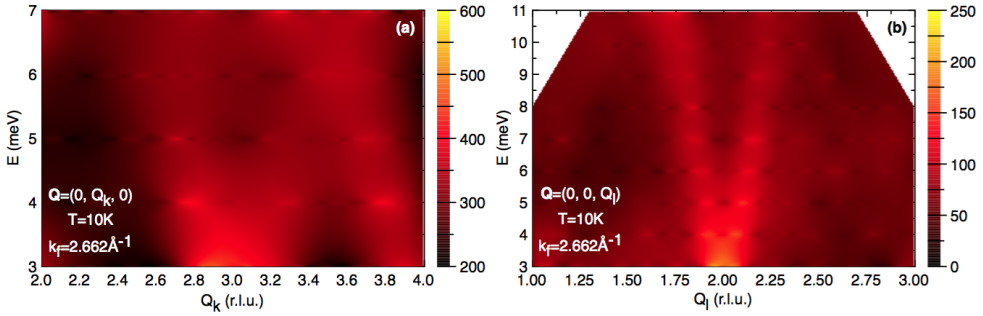

Figure 5.2: Colour maps constructed from **Q** scans at constant energy transfers $3 \leq E \leq 11$ meV at T=10 K. The spectra shown in (a) and (b) were obtained at 2T1 and IN20, respectivelly. (a) Branches originating from **G**=(0, 3, 0) and **G**=(0, 4, 0) correspond to magnons and LA phonons propagating along (0k0), respectively. (b) The dispersion curves originating from **G**=(0, 0, 2) correspond to LA phonons propagating along (00l).

In order to obtain the acoustic phonon dispersion curves, spectra were collected in transverse and longitudinal geometry around nuclear zone centers and away from magnetic Bragg positions. Every peak generated from a phonon excitation was fitted with a Gaussian function. It should be noted that the peaks observed at constant **Q** scans were fitted also with damped harmonic oscillator (DHO) functions, which give the same centers (within the error bars) as the fits with Gaussian functions. Before fitting, every spectrum was analyzed carefully looking for accidental scattering, in particular aluminium contamination, and the corresponding regions were cut out. E-scans were conducted only in the focussing side in order to determine excitations close to the zone boundary where the dispersion curves become flat.

The transverse acoustic (TA) phonon propagating along (0k0) and polarized in (00l) was measured around **G**=(0, 0, 2). The LA phonon propagating along (0k0) for energy transfers $3 \leq E \leq 5$ meV was measured around **G**=(0, 4, 0) and for $E \geq 5$ meV around **G**=(0, 12, 0). The TA phonon propagating along (00l) and polarized in (0k0) was measured around **G**=(0, 8, 0) and **G**=(0, 10, 0). The LA phonon propagating along (00l) for $3 \leq E \leq 10$ meV was measured around **G**=(0, 0, 2) and for $E \geq 10$ meV around **G**=(0, 0, 4). The resulting phonon dispersion curves at T=10 K are shown in Fig. 5.3. Data points with horizontal error bars correspond to constant E scans and vertical error bars correspond to constant **Q** scans. As can be seen in Fig. 5.3, only the TA[0 1 0]$_{\langle 001 \rangle}$ phonon has been determined up to the Brillouin zone boundary. All the other acoustic phonons have been measured only to about half way to the zone boundaries, since no peaks were observed in the constant **Q** scans in the investigated Brillouin zones for $E \geq 12$ meV that could be assigned to acoustic modes.

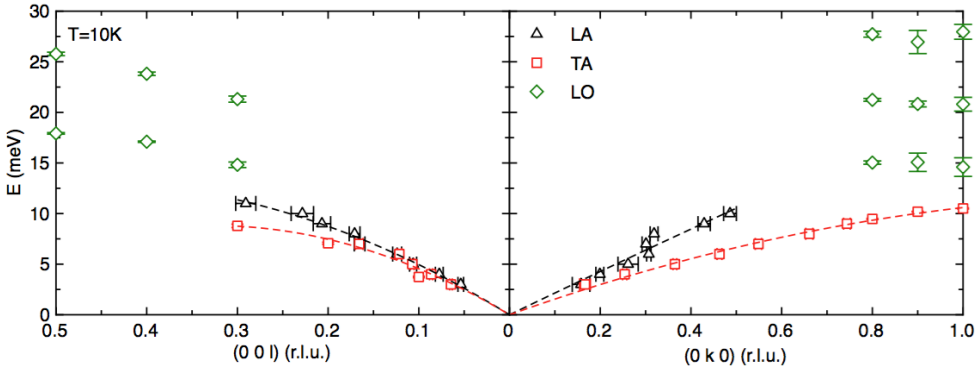

Figure 5.3: Phonon dispersion curves of Mn_5Si_3 at T=10 K along the (00l) and (0k0) directions from unpolarized INS. Triangles and squares correspond to longitudinal (LA) and transverse (TA) acoustic phonons, respectively. Symbols at $E \geq 13$ meV correspond to optic phonons with longitudinal character (LO). The dashed lines can be used as guide for the eyes and extrapolate the acoustic phonon dispersions to q=0.

From the obtained phonon dispersion curves further parameters can be deduced. The orthorhombic crystal symmetry implies that 9 elastic moduli C_{ij} are independent and non-zero [108]:

$$C_{ij} = \begin{pmatrix} C_{11} & C_{12} & C_{13} & 0 & 0 & 0 \\ C_{12} & C_{22} & C_{23} & 0 & 0 & 0 \\ C_{13} & C_{23} & C_{33} & 0 & 0 & 0 \\ 0 & 0 & 0 & C_{44} & 0 & 0 \\ 0 & 0 & 0 & 0 & C_{55} & 0 \\ 0 & 0 & 0 & 0 & 0 & C_{66} \end{pmatrix} \tag{5.5}$$

The elastic moduli C_{ii} are calculated via [108]:

$$C_{ii} = \rho v^2, \tag{5.6}$$

where v refers to the velocity of each mode and ρ to the density (ρ=6.06 g/cm^3 for Mn_5Si_3). The phonon velocities can be determined from linear fits of the experimental acoustic phonon dispersions at low energy transfers ($E \leq 5$ meV). The orthorhombic crystallographic directions (h00), (0k0) and (00l) are pure mode directions and all acoustic wave velocities measured along these directions are related to single elastic constants only. Determining the wave velocities of longitudinal and transverse acoustic phonons along these three high symmetry directions results to the isolation of the diagonal elements in the elastic constant matrix. From the available experimental data three of them could be determined, namely C_{22}, C_{33} and C_{44}. In order to derive the remaining diagonal elements it is necessary to measure the LA[1 0 0] (for C_{11}), the TA[1 0 0]$_{\langle 010 \rangle}$ or the TA[0 1 0]$_{\langle 100 \rangle}$ (for C_{66}) and the TA[1 0 0]$_{\langle 001 \rangle}$ or the TA[0 0 1]$_{\langle 100 \rangle}$ (for C_{55}). Table 5.2 summarizes the experimental results of the phonon velocities and the elastic moduli of Mn_5Si_3 derived at T=10 K, which are found to correspond to typical values of solids. The calculated constant C_{44} deduced from two different TA modes, results to the same number within the value of uncertainty. To the knowledge of the author, results for the parameters v and C_{ii} cannot be found in literature for comparison.

For obtaining the magnon dispersion along the (h00), (0k0) and (00l) directions, **Q** scans at constant energies below 25 meV were carried out around the magnetic Bragg peaks (2, 1, 0), (0, 3, 1) and (0, 1, 1).

Table 5.2: Summary of investigated acoustic branches of Mn_5Si_3 with the direction of the propagation and polarization vectors of phonons. Parameters υ and C_{ii} refer to the acoustic wave velocity and elastic moduli derived at T=10 K, respectively.

Mode	Propagation vector	Polarization vector	υ (m/s)	C_{ii} (GPa)
LA[0 0 1]	[0 0 1]	⟨0 0 1⟩	5211(115)	C_{33}=165(7)
TA[0 0 1]$_{\langle 010\rangle}$	[0 0 1]	⟨0 1 0⟩	4200(300)	C_{44}=107(15)
LA[0 1 0]	[0 1 0]	⟨0 1 0⟩	5900(250)	C_{22}=211(18)
TA[0 1 0]$_{\langle 001\rangle}$	[0 1 0]	⟨0 0 1⟩	3860(180)	C_{44}=90(8)

Because very steep magnon branches were observed, the analyser was set up in flat mode for all scans in order to improve the Q resolution (configuration "J" in Table 5.1). Such scans were mostly conducted between intervals of +q and -q. Therefore every peak was measured in the focusing and the defocusing mode. The exact position of a magnon was evaluated by fitting the excitation spectrum with a double Gaussian with same center at the focusing and defocusing side, but with different widths and amplitudes. Such typical scans with the corresponding fits are shown in Fig. 5.4 at different constant energy transfers in the AF1 phase (T=10 K) along the two high symmetry orthorhombic directions (0k0) and (00l). The spectra show a maximum at finite q, which shifts to higher values with increasing energy transfers. This behavior indicates that the peaks correspond to dispersive spin-waves.

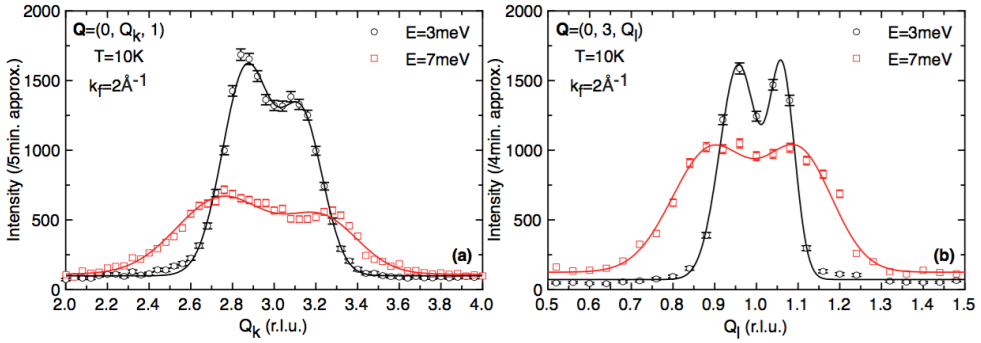

Figure 5.4: Unpolarized neutron spectra obtained at IN12. The raw data depict spin-wave scattering at different constant energy transfers around (a) **Q**=(0, Q_k, 1) and (b) **Q**=(0, 3, Q_l) at T=10 K (AF1 phase). The solid lines correspond to fits with double Gaussian functions as described in the text.

The magnon dispersion along the (00l) and (0k0) directions is very steep and up to the investigated energy transfer of 22 meV the zone boundaries are not reached. A remarkable feature is that along all three high symmetry directions ((00l), (0k0) and (h00)) the low energy spin-waves ($E\leq$8 meV) of Mn_5Si_3 are isotropic in contrast to $MnFe_4Si_3$ (see Section 4.3). For energy transfers $E\geq$7 meV a broadening of the spin-waves is observed. The broadening could be attributed to crossing of spin-waves from different domains (see Section 5.5.1). Attempts to describe the experimental magnon spectrum with the empirical dispersion relations $E=\sqrt{\Delta^2 + {c^{sw}_{(hkl)}}^2 q^2}$ and $E=\sqrt{\Delta^2 + {c^{sw}_{(hkl)}}^2 sin^2 q}$ [109] were not successful. In these relations Δ is the energy gap, $c^{sw}_{(hkl)}$ is the spin-wave velocity and q is the momentum transfer. However, when fitting only the low energy part of the magnon dispersion ($E\leq$8 meV) one can obtain for the energy gap Δ=1.6(3) meV, but the values for the spin-wave velocities are almost equal to the standard deviation

and therefore are not reliable. To verify experimentally the existence of an energy gap measurements at low energy transfers ($E \leq 2$ meV) are essential. At this stage simulating the spin-wave spectrum is not an easy task, because the magnetic structure of the AF1 phase is complicated and the experimental data limited.

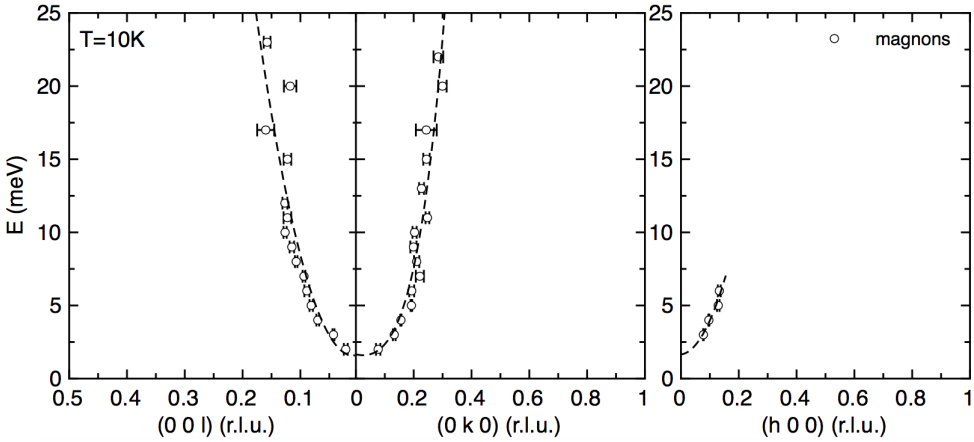

Figure 5.5: Spin-wave dispersion curves of Mn_5Si_3 at T=10 K (AF1 phase) along the (00l), (0k0) and (h00) directions from unpolarized INS. The dashed lines can be used as guide for the eyes.

5.5 Spin dynamics in the collinear AF2 phase

5.5.1 Unpolarized INS data

The temperature dependence of the purely magnetic (1, 2, 0), (0, 3, 0) and (0, 3, 1) Bragg peak intensities are shown in Figs 5.6(a)-(b). (1, 2, 0) and (0, 3, 1) mark the onset of AF2 ordering. Neutron scattering is sensitive to magnetic moments or fluctuations perpendicular to the scattering vector. The $\mathbf{Q}$ vector of (0, 3, 0) is almost parallel to the magnetic moments of the AF2 phase and the associated Bragg peak intensity is therefore nearly extinguished. However, it is convenient to detect the AF1 transition. A colour-coded intensity map of the INS intensities measured for a constant energy transfer of E=5 meV as a function of $\mathbf{Q}$=(Q_h, 2, 0) and T is shown in Fig. 5.6(c). The PM scattering is constituted of a broad peak centered at the magnetic center Q_h=1 r.l.u., the signature of a correlated diffuse signal. The shape of the scattering of the AF2 phase resembles the one of the PM state, no marked change in the dynamical response occurs at T_{N_2}. In contrast, AF1 ordering is characterized by a strong modification of the spectrum leading to sharp spin-wave peaks identified through the ridges at Q_h=0.87 r.l.u. and Q_h=1.13 r.l.u., the former being more prominent due to the instrumental resolution focusing conditions. The same observation stems from the colour-coded intensity map for a constant energy transfer of E=6 meV as a function of $\mathbf{Q}$=(0, 3, Q_l) and T (see Fig. 5.6(d)), where spin-wave peaks appear in the AF1 phase, while the signal in the AF2 phase and in the PM state seems identical.

Measurements at the energy transfer of E=3 meV for selected temperatures corresponding to the different phases along the (0k0) and (00l) directions are shown in Figs 5.7. Consistently with Figs 5.6(c)-(d) the shape of the scattering of the AF2 phase (T=80 K) resembles the one of the PM state (T=120 K).

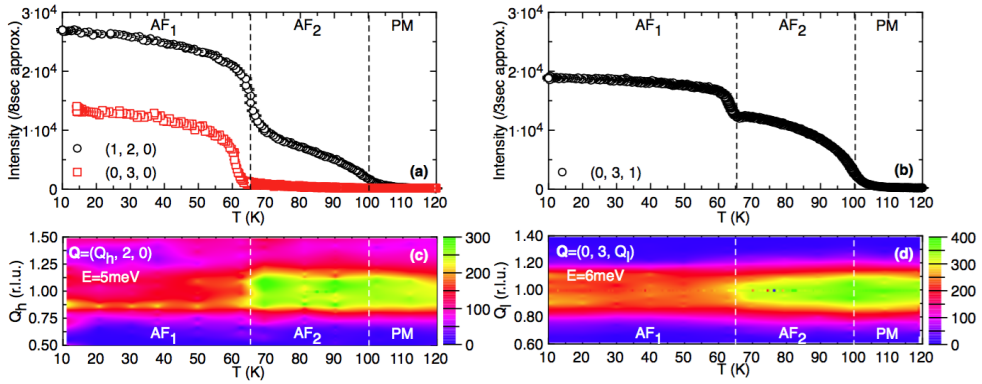

Figure 5.6: Neutron scattering results in the two AF phases and in the PM state of Mn_5Si_3. Temperature dependence of the purely magnetic (a) (1, 2, 0) and (0, 3, 0) and (b) (0, 3, 1) Bragg peak intensities. Colour-coded intensity plot of the INS data collected (c) at E=5 meV as a function of **Q**=(Q_h, 2, 0) and T and (d) at E=6 meV as a function of **Q**=(0, 3, Q_l) and T. Data were collected with unpolarized neutron beam at 2T1 and at IN22. In the inelastic spectra the background was subtracted and the measured intensity was corrected by the detailed balance factor.

The clear peaks in the AF1 phase (T=10 K) at finite q away from the magnetic center correspond to spin-wave scattering. It is demonstrated that the spin excitation spectrum is markedly different in the two magnetically ordered phases along all the three orthorhombic high symmetry directions, namely (h00), (0k0) and (00l).

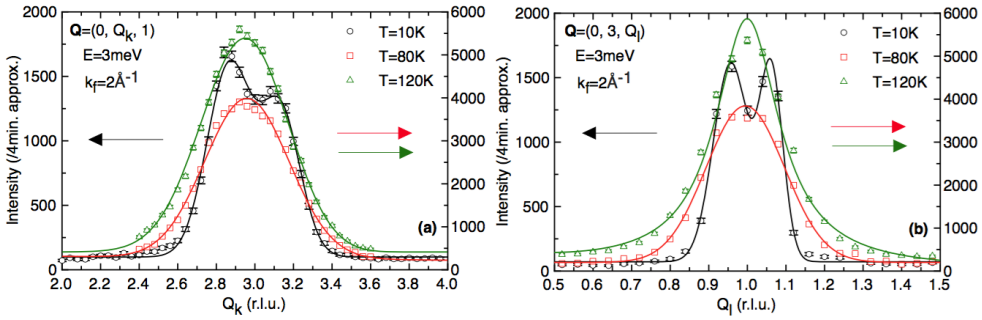

Figure 5.7: Spectra obtained at IN12 with unpolarized neutrons around (a) **Q**=(0, Q_k, 1) and (b) **Q**=(0, 3, Q_l) in the AF1 (T=10 K), AF2 (T=80 K) phase and in the PM (T=120 K) state at constant energy transfer of 3 meV. Neutron intensity for T=10 K is given on the left and for T=80 K and T=120 K on the right vertical axis. Lines in the AF1 phase and in the PM state indicate fits with Gaussian and Lorentzian functions, respectively. The line in the AF2 phase can be used as guide for the eyes.

To confirm further this observation, additional INS spectra were collected in large portions of the reciprocal space with FlatCone setup (configuration "G" in Table 5.1) in (a, b) and (b, c) scattering planes for E=3 meV at three different temperatures corresponding to the PM state (T=120 K), the collinear AF2 phase (T=80 K) and the non-collinear AF1 phase (T=10 K) (see Figs 5.8(a)-(e)). In the AF1 phase, the rings in the Figs 5.8(a) ((b,c) scattering plane) and 5.8(d) ((a,b) scattering plane) represent intense phonon

and spin-wave scattering originating from the structural ($h + k$ even) and magnetic ($h + k$ odd) zone centers, respectively. Apart from these rings, similar signal is also observed around half integer h and k positions in the (a,b) plane (see e.g. Fig. 5.8(d)). These additional rings are assigned to spin-wave scattering originating from other magnetic domains, the domain structure being reminiscent of the sixfold symmetry of the high temperature hexagonal phase. Consistently with Figs 5.6(c)-(d) and 5.7, the spin excitation spectrum is different in the AF1 and AF2 phases for the inelastic spectra that originate from the magnetic Bragg peaks that exist in the two phases (e.g. (1, 2, 0), (1, 4, 0), (0, 3, 1), (0, 1, 1)). While in the AF1 phase clear rings indicate spin-wave scattering (see Figs 5.8(a) and 5.8(d)), the signal in the AF2 phase (bright yellow spots in Figs 5.8(b) and 5.8(e)) resembles the one of the PM state (Fig. 5.8(c)).

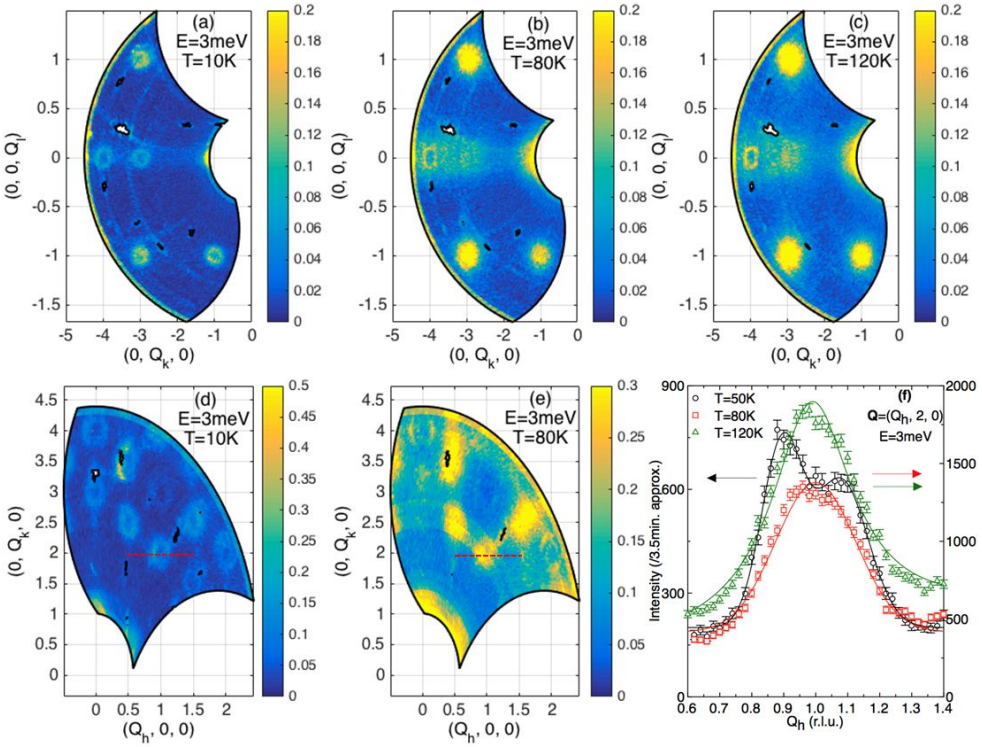

Figure 5.8: (a)-(e) FlatCone measurements at ThALES in the AF1 (T=10 K), AF2 (T=80 K) phase and in the PM (T=120 K) state at constant energy transfer of 3 meV. Figs (a)-(c) and (d)-(e) correspond to the scattering planes (b,c) and (a,b), respectively. The "holes'" in the spectra correspond to spurious scattering that has been masked during the data evaluation. (f) Raw data obtained at IN12 (k_f=1.8 Å^{-1}) with unpolarized neutron beam around $\mathbf{Q}$=(Q_h, 2, 0). The corresponding $\mathbf{Q}$ range of the cuts is indicated with horizontal red dashed lines in Figs (d) and (e) for the AF1 and AF2 phases. Neutron intensity for 50 K is given on the left and for 80 K and 120 K on the right vertical axis. Lines in the AF1 phase (T=50 K) and in the PM state (T=120 K) indicate fits with Gaussian and Lorentzian functions, respectively. The line in the AF2 phase (T=80 K) is a guide for the eyes.

The spin dynamics of the AF1 phase sustains only propagating spin-waves (see Figs 5.4 and 5.9(a)) along the three high symmetry orthorhombic directions, namely (0k0), (00l) and (h00). All spectra show a maximum at finite q, which shifts to higher values with increasing energy transfers. On the contrary, for

the spectra in the PM state (T=120 K) (see Fig. 5.9(b)) there is no well-defined inelastic mode associated with a given wave vector, all spectra are centered at the magnetic center and the intensity is decreasing with increasing energy transfers while the signal broadens. This is typical for PM scattering and indicates the diffusive nature of the spin-fluctuations. The observed behavior for the AF1 phase and the PM state is expected, but the spin dynamics of the AF2 phase is very peculiar. Additional spectra in the AF2 phase can be found in Appendix A.2.1.

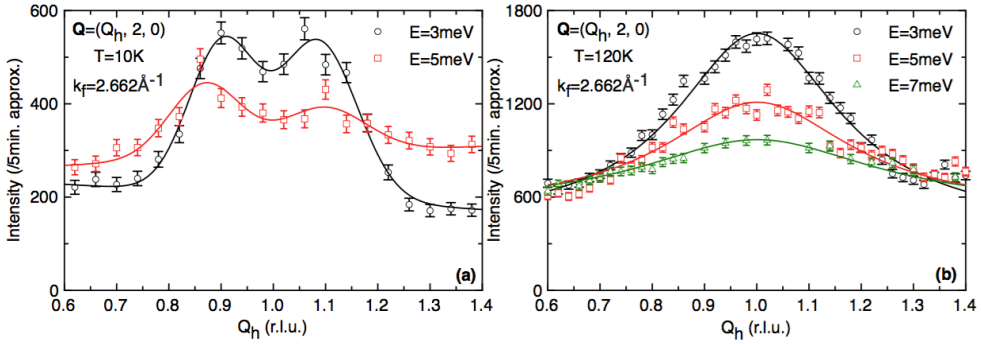

Figure 5.9: (a) Raw data depicting spin-wave scattering at different constant energy transfers along the (h00) high symmetry direction of the orthorhombic system at T=10 K (AF1 phase). Lines represent fits with Gaussian functions. (b) PM scattering at different constant energy transfers along the (h00) high symmetry direction of the orthorhombic system at T=120 K. Lines represent fits with Lorentzian functions. Data were obtained at 2T1.

5.5.2 Polarized INS data

The AF2 phase is at first sight not constituted of discrete modes, but of a broad continuum of states. In order to get more insight concerning this behavior and to compare it with the seemingly identical PM spin dynamics, spectra were collected using polarized INS methods. In such an experiment the neutron beam polarization is prepared in different states which gives access to different neutron cross sections. The conventions are the same as defined in Section 2.2.6.2: (i) the momentum transfer $\mathbf{Q}$ is parallel to x-axis, (ii) the initial polarization was prepared parallel to x-axis, perpendicular to $\mathbf{Q}$ in the scattering plane (y-axis) and perpendicular to the scattering plane (z-axis) and (iii) the final polarization was analyzed for a scattering process reversing the initial polarization by 180 °. The corresponding measurement channels are canonically labelled SF_{xx}, SF_{yy} and SF_{zz}, where SF stands for Spin-Flip.

Figs 5.10 illustrate spectra collected around $\mathbf{Q}$=(Q_h, 2, 0) at T=80 K (AF2) and T=120 K (PM) for SF_{xx}, SF_{yy} and SF_{zz} channels. The spectra in the PM state at T=120 K are identical for the two polarization channels SF_{yy} and SF_{zz}, which indicates isotropic spin-fluctuations (see Fig. 5.10(a)). In contrast, the spectra in the AF2 phase at T=80 K are different for the two polarization channels concerning intensities and lineshapes (see Fig. 5.10(c)). This indicates that the magnetic excitation spectrum is different in the AF2 phase and PM state, a fact that was not evidenced by the unpolarized INS data shown above. Moreover, the better wave-vector resolution achieved with the setup used to collect the polarized INS data (configuration "L" in Table 5.2) allows to reveal the flat top shape of the peaks at T=80 K. This hints to a signal composed of several ill-resolved peaks. The difference of the spin dynamics in the AF2

phase and the PM state is also reflected in the spectra for the polarization channel SF_{xx} (see Fis 5.10(b) and 5.10(d)). Altogether these information point to the fact that the signal in the AF2 phase is composed of different components.

The simplest hypothesis is to consider that the signal is composed of spin-fluctuations coexisting with spin-waves. This natural assumption stems from the nature of the AF2 magnetic phase with mixed magnetic and non-magnetic sites. It is expected that it sustains both kind of excitations: spin-waves, collective precession of spins around the ordered moment and spin-fluctuations, which correspond to weakly correlated spin relaxation of non-ordered moments. Each of these excitations is the landmark of magnetically ordered and disordered phases, respectively.

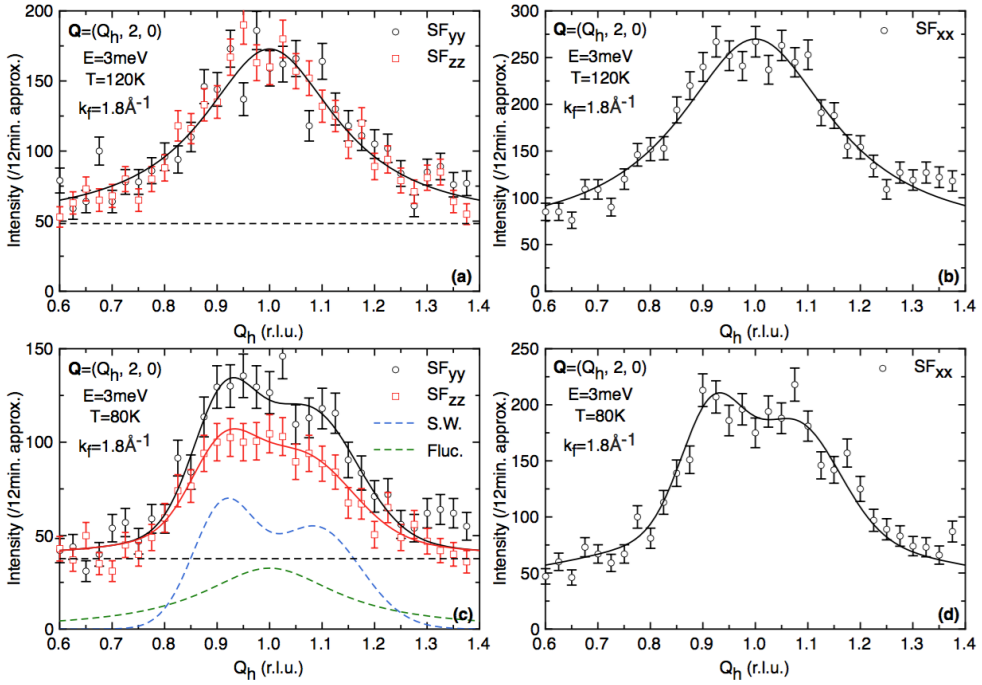

Figure 5.10: Inelastic spectra obtained with polarized neutrons in the PM state (T=120 K) and in the AF2 phase (T=80 K). (a)-(b) In the PM state (T=120 K) the solid line corresponds to a Lorentzian function fit. (c)-(d) In the AF2 phase (T=80 K) the solid lines represent overall fits and the dashed lines the individual signal from spin-waves (S.W.) and spin-fluctuations (Fluc.) (see details in text). The horizontal dashed line indicates the background level. Data were obtained at IN12 at constant energy transfer of 3 meV around $\mathbf{Q}$=(Q_h, 2, 0).

Neutron scattering experiments probe only the magnetism perpendicular to the scattering vector $\mathbf{Q}$, the measured magnetic fluctuations are $\langle \delta M_y \rangle$ and $\langle \delta M_z \rangle$ (see Section 2.2.6.2). In order to have a quantitative result concerning the spin-wave and the spin-fluctuation contributions to the spectra in the AF2 phase of Mn_5Si_3 several assumptions were made. Assuming that the background is the same for the three spin-flip channels (BG_{SF}) and in the crystal frame for $\mathbf{Q}$ in the (a,b) plane, the double differential cross-sections

become (see Eq. 2.24 in Section 2.2.6.2):

$$\mathrm{SF}_{yy} : \left(\frac{d^2\sigma}{d\Omega dE}\right)^{y}_{\mathrm{SF}} \propto BG_{\mathrm{SF}} + \langle \delta M_c \rangle \tag{5.7}$$

$$\mathrm{SF}_{zz} : \left(\frac{d^2\sigma}{d\Omega dE}\right)^{z}_{\mathrm{SF}} \propto BG_{\mathrm{SF}} + cos^2\theta \langle \delta M_b \rangle + sin^2\theta \langle \delta M_a \rangle, \tag{5.8}$$

with θ the angle between **Q** and the [100] direction which can be calculated by θ=arctan($\frac{2}{Q_h}\frac{a}{b}$) for **Q**=(Q_h, 2, 0). In the AF2 phase the magnetic moments lie parallel and antiparallel to the b-axis. Spin-waves correspond to precession perpendicular to the ordered moment so their components will appear in $\langle \delta M_c \rangle$ and $\langle \delta M_a \rangle$. Assuming that the signal in this phase consists of spin-waves (sw) and spin-fluctuations (f), the cross sections can be rewritten as:

$$\mathrm{SF}_{yy} : \left(\frac{d^2\sigma}{d\Omega dE}\right)^{y}_{\mathrm{SF}} \propto BG_{\mathrm{SF}} + \langle \delta M_c^{sw} \rangle + \langle \delta M_c^{f} \rangle \tag{5.9}$$

$$\mathrm{SF}_{zz} : \left(\frac{d^2\sigma}{d\Omega dE}\right)^{z}_{\mathrm{SF}} \propto BG_{\mathrm{SF}} + cos^2\theta \langle \delta M_b^{f} \rangle + sin^2\theta \langle \delta M_a^{f} \rangle + sin^2\theta \langle \delta M_a^{sw} \rangle \tag{5.10}$$

Assuming that the spin-waves and the spin-fluctuations are isotropic, Eq. 5.9 and Eq. 5.10 can be simplified further to:

$$\mathrm{SF}_{yy} : \left(\frac{d^2\sigma}{d\Omega dE}\right)^{y}_{\mathrm{SF}} \propto BG_{\mathrm{SF}} + \langle \delta M^{sw} \rangle + \langle \delta M^{f} \rangle \tag{5.11}$$

$$\mathrm{SF}_{zz} : \left(\frac{d^2\sigma}{d\Omega dE}\right)^{z}_{\mathrm{SF}} \propto BG_{\mathrm{SF}} + \langle \delta M^{f} \rangle + sin^2\theta \langle \delta M^{sw} \rangle \tag{5.12}$$

The measured intensity for the spin-fluctuations and the spin-waves can be described by a Lorentzian and a set of two Gaussians, respectively. In order to reduce the number of fitted parameters, we assume that the Lorentzian function is centered at Q_h=1 r.l.u. and that its width equals to the one obtained from the fitting in the PM state (see Fig. 5.10(a) and Appendix A.2.2). The resulting fits for the AF2 phase are shown in Figs 5.10(c)-(d) for SF_{yy}, SF_{zz} and SF_{xx}. Consistently the spin-wave scattering in the polarization channel SF_{zz} is reduced due to the angle prefactor $sin^2\theta$, which decreases with increasing **Q**. The magnons in the AF2 phase are peaked at about the same Q_h position as in the AF1 phase for E=3 meV. In order to draw firm conclusions concerning the spin-wave stiffness along the (h00) direction, measurements are needed in higher energy transfers in both AF phases. It is to be noted that SF_{yy} and SF_{zz} are fitted simultaneously in order to reduce the space of accessible parameters. The data are well described by this model and since the polarized INS cross-sections conveys stringent fitting conditions, it gives credit to the hypothesis of the coexistence of spin-waves and spin-fluctuations.

5.6 Field induced spin-fluctuations

Previous neutron diffraction measurements performed under magnetic field in powder and single crystal samples indicate a transition from the AF1 to the AF2 phase at H=3.5 T for T=58 K [50, 52]. The full magnetic phase diagram as a function of temperature and magnetic field up to 10 T applied along the c-axis was established by electrical transport and magnetization measurements [53] and is shown in Fig. 5.11. Below T=60 K, the increasing magnetic field induces transitions from the AF1 to another intermediate AF1' phase before reaching the AF2 phase. The intermediate AF1' phase will not be addressed in

the present study (to the knowledge of the author the magnetic structure of the AF1' phase is not yet established with neutron diffraction experiments). Above T=60 K, the AF2 phase is stable up to the maximum investigated field of 10 T.

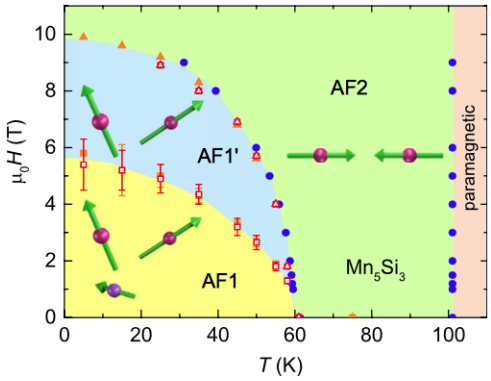

Figure 5.11: (T-H) magnetic phase diagram of Mn_5Si_3 for $\vec{H} \parallel c$ (taken from [53]).

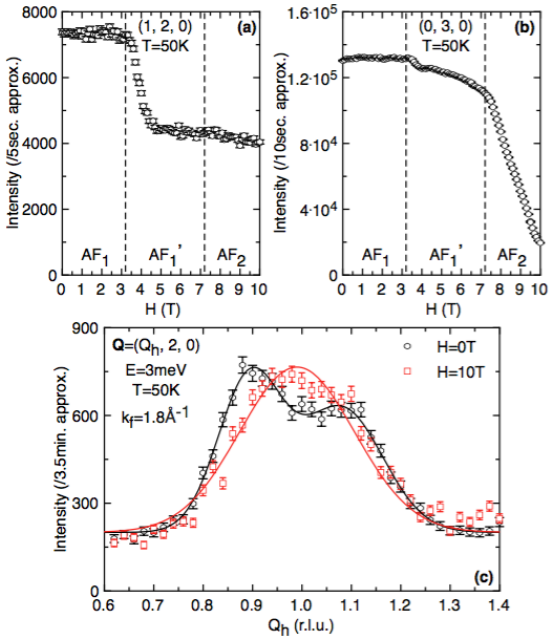

Figure 5.12: (a)-(b) Field dependence of the magnetic Bragg peaks of Mn_5Si_3 at T=50 K for $\vec{H} \parallel c$. For (1, 2, 0), a 9 mm plexiglass attenuator was in place. (c) Inelastic spectra obtained at T=50 K around $\mathbf{Q}$=(Q_h, 2, 0) under H=0 T and H=10 T for an energy transfer of 3 meV. The red line is guide for the eyes and the black line correspond to fits with Gaussian functions. Data were obtained with unpolarized neutron beam at IN12.

Building up on these results, an investigation of the field dependence of the magnetic Bragg peak intensities (1, 2, 0) and (0, 3, 0) at T=50 K for a magnetic field applied along the c-axis was performed (see

Figs 5.12(a)-(b)). Starting at H=0 T in the AF1 phase, two anomalies at approximatively 3 and 7 T mark the onset of different magnetic phases that are identified as AF1' and AF2 phases, roughly consistent with the (T-H) phase diagram of Ref. [53]. Above 7 T, the system re-enters into the AF2 phase characterized by a drop of a factor ≈2 compared to AF1 in the intensity of the Bragg peak (1, 2, 0) and a continuous diminution of the (0, 3, 0) Bragg peak intensity. Up to the maximum investigated field of 10 T, the PM state is not reached, which is related to the very steep $T_{N_2}(H)$ phase boundary. The field induced AF2 phase at 50 K consists of AF coupled magnetic moments lying perpendicular to H with an additional increasing induced FM component, which is evidenced in magnetization measurements [53].

Fig. 5.12(c) shows INS spectra collected around **Q**=(Q_h, 2, 0) at T=50 K at a constant energy transfer of E=3 meV for H=0 and 10 T. The typical spin-wave spectra with two peaks in the AF1 phase at H=0 T transforms into a broad peak centered at the magnetic center Q_h=1 r.l.u. at H=10 T. Drawing a parallel between the spectra at T=50 K as a function of field (Fig. 5.12(c)) with the ones at H=0 T as a function of temperatures (Fig. 5.8(f)), one concludes that the field restores the fluctuations pattern associated with the AF2 phase. This leads to the unusual feature that a high enough magnetic field of 10 T applied in the AF1 phase induces spin-fluctuations. In contrast, a field of 10 T applied in the AF2 phase and PM state reduces the intensity of the magnetic excitations without changing their lineshapes. This is shown in Figs 5.13 for the AF2 phase and the PM state for the same **Q** range and energy transfer of 3 meV as in Fig. 5.12(c).

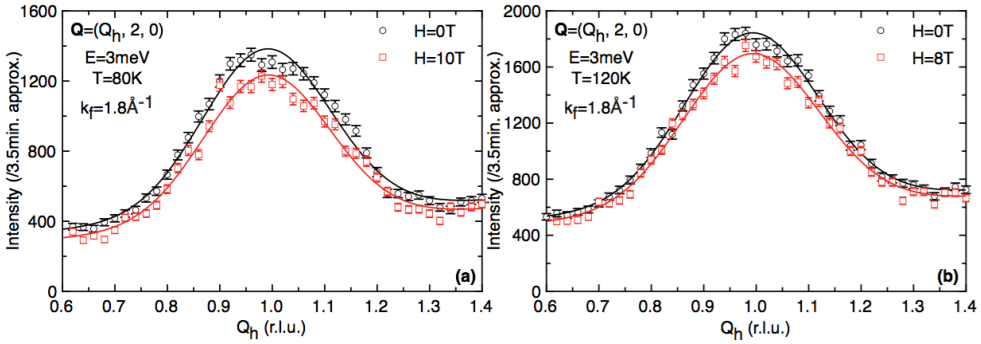

Figure 5.13: Inelastic spectra obtained with unpolarized neutrons at IN12 in (a) the AF2 phase (T=80 K) and (b) the PM state (T=120 K) around **Q**=(Q_h, 2, 0) for E=3 meV energy transfer. Data points in black and red indicate measurements with zero and high magnetic field, respectively. The lines are guides for the eyes.

5.7 Discussion

The microscopic ingredients giving rise to the stability of the mixed magnetism of the AF1 and AF2 phases, constituted of the coexistence of magnetic and non-magnetic sites, were discussed in previous studies on Mn_5Si_3 [49, 50, 51, 52, 53]. Namely, a first ingredient at play is the Mn1-Mn1 distance with respect to the critical value corresponding to the instability in the competition between bonding and magnetism. The shortest Mn1-Mn1 distance in Mn_5Si_3 equals c/2 and is too small in the AF2 state to lead to a magnetic configuration for Mn1. Below T_{N1}, an abrupt change of the lattice parameter value c occurs and this allows to stabilize the magnetic configuration of the Mn1 site. Under magnetic field, it was

shown by neutron diffraction experiment performed at 50 K and 4 T [50], that $c/2$ decreases below the critical value for Mn1 moment stability. The other shortest distances between Mn2-Mn1 and Mn2-Mn2 are above the critical value and are also modified during the transition from AF2 to AF1. A second ingredient common to the AF1 and AF2 phases is the geometrical frustration associated with the triangular arrangement of Mn2 atoms which leads to the occurrence of two ordered moments out of the three Mn2 sites (see Fig. 1.5).

Such mixed magnetic phases occur in other Mn-based compounds. The most extensively studied ones are the Laves phases RMn_2 (R being a rare earth element) for fundamental properties concerning magnetism [110], as well as, for the MCE [42]. The presence of a $4f$ element adds complexity to the magnetic properties, however it is possible to discuss in first approximation only the Mn subsystem, which sustains the leading magnetic interactions. In RMn_2 systems, the same ingredients as in Mn_5Si_3 are at play: instability of Mn magnetism and magnetic frustration. The switch from conventional to mixed AF phase as a function of magnetic field was theoretically predicted and verified by neutron diffraction experiments in $TbMn_2$ [111]. This situation bears similarity to Mn_5Si_3 and the results presented here find echo in the broader context of mixed magnetic systems studies. The present study goes one step further by evidencing the properties of the excitation spectrum of the mixed magnetic phases revealing the coexistence of two dynamical responses, spin-waves and spin-fluctuations.

Another important result of this study is the evidence of magnetic field induced spin-fluctuations. Starting from the AF1 phase, which sustains only spin-waves, the field restores the AF2 phase and its associated spin-fluctuations. In contrast to the discrete spin-wave spectrum, such spin-fluctuations which consist of a continuum of excitations involve more microscopic states. This leads to an increase of the magnetic entropy and thus plays a major role in the inverse-MCE. It is to be noted that the observed behaviour is opposite to the most common magnetic field effect that usually suppresses the spin-fluctuations and consequently decreases the magnetic entropy. The latter leads to the direct MCE although microscopic demonstrations of this more common mechanism are scarce as well. The suppression of spin-fluctuations with magnetic field was demonstrated in the FM MCE compound $MnFe_4Si_3$ (see Section 4.5).

Finally, the non-collinear AF1 phase of Mn_5Si_3 is also responsible of the anomalous Hall effect with a switch in electronic transport properties between AF1 and AF2 [53, 55, 112]. Therefore the search for complex magnetic structures is not only motivated by magneto-thermodynamic, but also by electronic properties.

5.8 Conclusions

In this study it is shown that among the two stable AF phases of Mn_5Si_3, the magnetic excitation spectrum is different. The low temperature AF1 phase ($T \leq 66$ K) is characterized by well-defined spin-waves, while the high temperature AF2 phase ($66 \leq T \leq 100$ K) has an unusual magnetic excitation spectrum. In the AF2 phase it is shown with polarized INS that propagative spin-waves and diffuse spin-fluctuations coexist. In addition, a magnetic field of 10 T applied in the AF1 phase restores the fluctuations pattern associated with the AF2 phase. It is evidenced that the modification of the magnetic excitation spectrum induced by the magnetic field tracks the inverse MCE of Mn_5Si_3, the cooling by adiabatic magnetization, via the associated change of magnetic entropy. Therefore, the need of designing functional materials for caloric applications connects with fundamental questions of magnetism.

Chapter 6

Investigation of phonon-magnon interaction in the magnetocaloric compound $MnFe_4Si_3$

6.1 Interaction between lattice and magnetic degrees of freedom

During the magnetocaloric cooling process an isothermal entropy change ΔS_{iso}, which is the entropy change at constant temperature T induced by a magnetic field change, takes place (see details in Section 1.2.2). ΔS_{iso} is expressed as the sum of the individual entropies of the magnetic, lattice and electronic degrees of freedom, ΔS_{iso}=ΔS_m+ΔS_l+ΔS_e. The individual entropies are related to the configurational entropy arising from magnetic disorder, excitation of lattice vibrations, and thermal occupation changes of the electronic states, respectively. Interactions between them are usually not considered (in first approximation), although the MCE requires an entropy transfer between the crystal lattice and the magnetic spin system (the electronic contribution ΔS_e is considered negligible). A possible mechanism that could describe this entropy transfer is the phonon-magnon coupling.

Magnons and phonons are propagating disturbances of the ordered magnetic moment and the atomic positions, respectively. The coupling or interaction between spin-waves and phonons is responsible for several interesting phenomena which are reported in the condensed matter physics. For example, one possible consequence of such coupling is the enhancement of anharmonic effects, as seen in the triangular antiferromagnet (Y,Lu)MnO_3 [113]. A magnetoelastic (magnon-phonon) coupling is believed also to be responsible for the observed low-temperature anomalous spin dynamical behaviour in the ferromagnetic manganese perovskites $A_{0.7}B_{0.3}MnO_3$ (where A and B are rare-earth and alkaline-earth elements, respectively) [114].

In general, the spin-wave and the phonon excitation spectrum can be modified in different ways due to phonon-magnon coupling. A strong spin-phonon interaction can give rise to the broadening of spin-waves [114] or phonon modes [115]. Another consequence of such coupling is the creation of energy gaps in the magnon dispersion at the intersecting point of phonon and magnon branches, as reported in the multiferroic $YMnO_3$ [116]. Finally, the coupling between magnetic and lattice degrees of freedom can generate dynamic mixed magnon-phonon excitations called electromagnons [117], which can be excited by the electric field of light at the resonant frequency [118].

6.2 Experimental details

To study the spin and lattice dynamics and their interactions, a combination of IXS and INS experiments is ideal to be carried out. To this aim, such experiments have been undertaken in single crystals of the MC compound $MnFe_4Si_3$. IXS measurements were performed on the beamline ID28 at the European Synchrotron Radiation Facility (ESRF). The incident photon energy of 17794 eV was produced by the Si(9, 9, 9) Bragg reflection. The overall energy resolution was of 3 meV at full width at half maximum (FWHM). A detailed description of the experimental setup can be found in Ref. [119]. The direction and the size of the momentum transfer were selected by an appropriate choice of the scattering angle and the sample orientation in the horizontal scattering plane. The analyzer arm was equipped with nine Si analyzers allowing to record IXS spectra at nine momentum transfers simultaneously. It should be noted that only the spectra from the second analyzer were evaluated, since for this analyzer **Q** is along a high symmetry direction. The momentum resolution was about 0.26 nm^{-1} and 0.8 nm^{-1} in the horizontal and vertical plane, respectively. The dimensions of the focused X-ray beam at the sample position were $30\times60\ \mu m^2$ (horizontal$\times$vertical), which allowed the selection of a single crystal domain with a typical mosaic spread of about 0.1 ° FWHM for the (3, 0, 0) and (0, 0, 2) Bragg reflections of $MnFe_4Si_3$. The determined lattice parameters at T=300 K, a=6.8048 Å and c=4.728 Å, are in good agreement with Ref. [56]. The sample was cooled down to T=90 K with a cryostream cold-nitrogen-gas blower and all measurements were performed in transmission. The thickness of the single crystal was about 100 μm.

Unpolarized and polarized INS measurements were carried out on the cold TAS IN12 at the ILL. IN12 was setup in W configuration with a fixed k_f=2 $Å^{-1}$ and a fully focusing setup was employed. The single crystal of $MnFe_4Si_3$ was mounted on an aluminium sample holder and oriented in the (a*,c) scattering plane of the hexagonal lattice. For unpolarized INS measurements the sample was cooled down to the base temperature $T\approx$1.5 K with a ^{4}He flow cryostat (configuration "A" in Table 4.1 in Section 4.2). For polarized INS measurements the same procedure as described in Section 4.2 was followed.

6.3 Investigating the lattice dynamics of $MnFe_4Si_3$ with IXS

In this chapter the same convention as described in Section 4.3 will be used: **Q=G+q** (all vectors are expressed in reciprocal hexagonal coordinates). To determine the low-lying ($E\leq$40 meV) lattice excitations along the high symmetry hexagonal directions, IXS measurements were mainly carried out around the zone centers **G**=(3, 0, 0), **G**=(5, 0, 0) and **G**=(0, 0, 4). Therefore, the $MnFe_4Si_3$ single crystal was oriented in two different scattering planes. For measuring the transverse phonon propagating along [1 0 0] and polarized in $\langle 1\ \bar{2}\ 0\rangle$ and the phonons along the $\Gamma-K-M$ directions the sample was oriented in the (a*,b*) scattering plane of the hexagonal lattice. In order to measure phonon branches along the $\Gamma-A$ and $\Gamma-M$ directions the (a*,c) scattering plane was selected. All IXS measurements were performed in the Stokes ($E>0$) and the anti-Stokes ($E<0$) side.

In order to fit the IXS spectra the Fit28 software (provided at the ID28 beamline) was used. The elastic line was fitted with a Lorentzian function centered at E=0 meV. The phonon energies (centers), linewidths (FWHM) and amplitudes were determined by using a damped harmonic oscillator (DHO) profile function. The functions (Lorentzian and DHO) were then convoluted with the experimentally determined resolution function. The ID28 instrumental energy resolution has a pseudo-Voigt profile with 2.71(2) and 3.3(1) meV FWHM of the Gaussian and Lorentzian components and a mixing parameter

of 0.63(2). The detailed balance of the model was taken into account by the Bose factor and a constant background with zero slope was assumed. The IXS spectra were fitted by keeping all the fit parameters of the excitations unconstrained and by using a χ^2 minimization routine.

A characteristic energy scan of IXS with the best fit results measured at **q**=0.3 r.l.u. around the **G**=(5, 0, 0) zone center is shown in Fig. 6.1(a). For clarity only the Stokes side is plotted. The first peak centered at E=0 meV is the elastic line. Three additional peaks that are identified as phonon excitations are very well pronounced. The peaks found at 12.6(2), 22.5(4) and 29.5(3) meV correspond, respectively, to a LA, LO1 and LO2 mode along the $\Gamma-$M direction. Fig. 6.1(b) shows selected IXS spectra for the out-of-plane polarized transverse acoustic phonons propagating along the $\Gamma-$M direction (TA[1 0 0]$_{\langle 001\rangle}$) for the indicated **Q**=(0+**q**, 0, 4) values. The scans are characterized by a weak elastic contribution and two symmetric features, the Stokes and anti-Stokes peaks of the corresponding phonons.

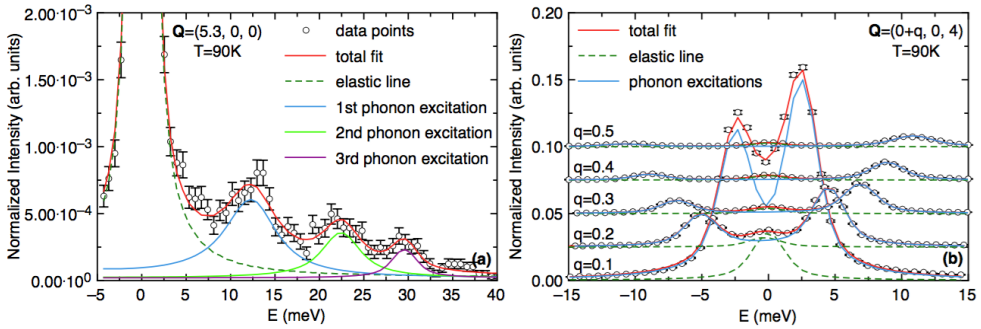

Figure 6.1: IXS spectra obtained at ID28 at T=90 K around (a) **Q**=(5.3, 0, 0) and (b) **Q**=(0+**q**, 0, 4). The experimental data are shown with the best fit results (full red lines: total fit, dashed lines: elastic lines, individual full lines: phonon excitations). The counting time per point was 1 minute. The spectra in (b) are shifted for clarity along the vertical direction by 0.025 normalized counts, conserving the same intensity scale.

Fig. 6.2 shows the phonon dispersion curves collected along the $\Gamma-$A, $\Gamma-$M and $\Gamma-$K$-$M directions of the hexagonal symmetry. Points belonging to the same acoustic branch are connected with dashed lines, which extrapolate the acoustic phonon dispersion curves to q=0. The remaining experimental data points belong to longitudinal (LO) or transverse (TO) optic modes. The majority of the acoustic phonon branches along the $\Gamma-$A, $\Gamma-$M and $\Gamma-$K high symmetry directions could be traced throughout the Brillouin zone.

The sound velocity was derived from the slope of the acoustic phonon dispersion in the low q limit and for low energy transfers ($E\leq$10 meV) by a linear fit. The elastic tensor for hexagonal symmetry contains 5 independent elastic moduli C_{ij} [108]:

$$C_{ij} = \begin{pmatrix} C_{11} & C_{12} & C_{13} & 0 & 0 & 0 \\ C_{12} & C_{11} & C_{23} & 0 & 0 & 0 \\ C_{13} & C_{23} & C_{33} & 0 & 0 & 0 \\ 0 & 0 & 0 & C_{44} & 0 & 0 \\ 0 & 0 & 0 & 0 & C_{44} & 0 \\ 0 & 0 & 0 & 0 & 0 & C_{66} = \frac{C_{11}-C_{12}}{2} \end{pmatrix} \tag{6.1}$$

From the available experimental data four of them could be determined, namely C_{11}, C_{33}, C_{44} and C_{66} (or C_{12} indirectly). Table 6.1 provides the list of the investigated phonon branches, the Brillouin zones

were they were measured and the calculated sound velocities and elastic moduli of the acoustic modes. The calculated elastic moduli are in reasonable agreement (within 98 %) with the reported results from resonant ultrasound spectroscopy of Ref. [59]. The largest deviation (of about 10 %) is found for C_{11} (and correspondingly for C_{12}).

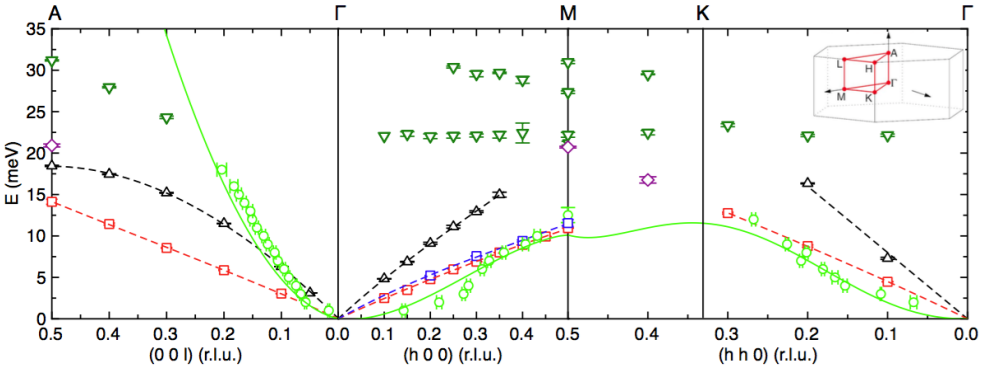

Figure 6.2: Experimental phonon and magnon dispersion curves for $MnFe_4Si_3$ along the high symmetry (hexagonal) Γ−A, Γ−M and Γ−K−M directions. Upward triangles, squares, downward triangles and diamonds correspond, respectively, to LA, TA, LO and TO phonons measured with IXS at T=90 K. Dashed lines are guides for the eyes that extrapolate the acoustic phonon dispersion curves to q=0. Circles correspond to magnons measured with INS. The solid line represents the spin model described by a Heisenberg-type Hamiltonian (see details in Section 4.3). The inset shows a sketch of the high symmetry hexagonal reciprocal directions.

Table 6.1: Summary of the investigated phonon branches of $MnFe_4Si_3$ with IXS at T=90 K with the direction of the momentum transfer, the propagation and polarization vectors of the phonons, and the calculated sound velocity (v) and elastic moduli (C_{ii}). The parameter q is always positive. The density for $MnFe_4Si_3$ is ρ=6.368 g/cm^3.

Mode	Brillouin zone Momentum Transfer	Propagation vector	Polarization vector	v (m/s)	C_{ii} (GPa)
LA[0 0 1]	(0, 0, 4)	(0, 0, q)	[0 0 1]	⟨0 0 1⟩	7056(5)	C_{33}=317(1)
LO[0 0 1]	(0, 0, 4)	(0, 0, q)	[0 0 1]	⟨0 0 1⟩	–	–
TA[0 0 1]$_{\langle 100\rangle}$	(3, 0, 0)	(0, 0, q)	[0 0 1]	⟨1 0 0⟩	3460(3)	–
TO[0 0 1]$_{\langle 100\rangle}$	(3, 0, 0)	(0, 0, q)	[0 0 1]	⟨1 0 0⟩	–	–
LA[1 0 0]	(5, 0, 0)	(q, 0, 0)	[1 0 0]	⟨1 0 0⟩	6773(14)	C_{11}=292(1)
LO1[1 0 0]	(5, 0, 0)	(q, 0, 0)	[1 0 0]	⟨1 0 0⟩	–	–
LO2[1 0 0]	(5, 0, 0)	(q, 0, 0)	[1 0 0]	⟨1 0 0⟩	–	–
TA[1 0 0]$_{\langle 001\rangle}$	(0, 0, 4)	(q, 0, 0)	[1 0 0]	⟨0 0 1⟩	3320(1)	C_{44}=70(1)
TA[1 0 0]$_{\langle 1\bar{2}0\rangle}$	(3, 0, 0)	($-q$, q, 0)	[1 0 0]	⟨1 $\bar{2}$ 0⟩	3613(4)	C_{66}=83(1)
LA[1 1 0]	(3, 0, 0)	(q, q, 0)	[1 1 0]	⟨1 1 0⟩	6430(190)	–
LO1[1 1 0]	(3, 0, 0)	(q, q, 0)	[1 1 0]	⟨1 1 0⟩	–	–
LO2[1 1 0]	(3, 0, 0)	(q, q, 0)	[1 1 0]	⟨1 1 0⟩	–	–
TA[1 1 0]$_{\langle 1\bar{1}0\rangle}$	(3, 0, 0)	($-q$, 2q, 0)	[1 1 0]	⟨1 $\bar{1}$ 0⟩	3671(5)	–
TO[1 1 0]$_{\langle 1\bar{1}0\rangle}$	(3, 0, 0)	($-q$, 2q, 0)	[1 1 0]	⟨1 $\bar{1}$ 0⟩	–	–

6.4 Investigating possible phonon-magnon interaction in $MnFe_4Si_3$ with INS and IXS

The combination of INS (see Section 4.3) and IXS measurements allowed to unambiguously determine the magnetic and lattice excitations of the MC compound $MnFe_4Si_3$. The individually measured excitations indicate that the spin-waves intersect with the phonon branches along the $\Gamma-A$ and $\Gamma-M$ directions (see Fig. 6.2). Along the $\Gamma-A$ direction the magnon crosses the TA[0 0 1]$_{\langle 100\rangle}$ and the LA[0 0 1] phonon at q=0.05 r.l.u. and q=0.10 r.l.u., respectively. For the $\Gamma-M$ direction a more remarkable feature is evidenced; the magnon branch close to the zone boundary falls exactly between the two TA phonons, namely the TA[1 0 0]$_{\langle 001\rangle}$ (red squares in Fig. 6.2) and the TA[1 0 0]$_{\langle 1\bar{2}0\rangle}$ (blue squares in Fig. 6.2).

The widths of the phonons in the vicinity of the crossing area with the magnons along these two high symmetry direction show a different behaviour. Along the $\Gamma-A$ direction the widths of the phonon peaks remain unchanged with increasing q (see Appendix A.3) in contrast to a remarkable q-dependent width broadening of the TA modes along $\Gamma-M$ (see Fig. 6.1(b)). The large broadening is better visualized in Fig. 6.3(a), where the convoluted with the instrumental resolution FWHM of the TA[1 0 0]$_{\langle 001\rangle}$ and the TA[1 0 0]$_{\langle 1\bar{2}0\rangle}$ phonon as a function of q throughout the whole Brillouin zone are shown. The increasing broadening of the widths coincides with the magnon crossing and in fact the TA phonon linewidths increase more by a factor of 10 from that measured at $q \leq 0.40$ r.l.u..

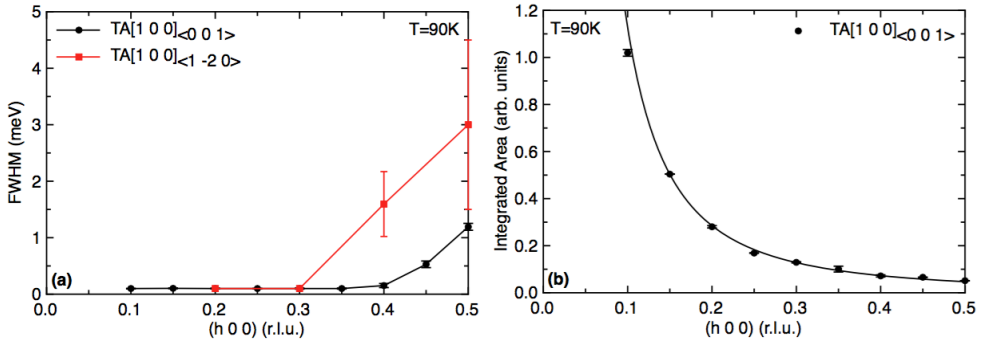

Figure 6.3: (a) FWHM and (b) integrated area as a function of q for the TA phonons (measured with IXS) along the $\Gamma-M$ direction at T=90 K. The lines in Fig. (a) are guides for the eyes. The line in Fig. (b) corresponds to a fit as explained in the text.

In Fig. 6.3(b) one can find the energy integrated area of the TA[1 0 0]$_{\langle 001\rangle}$ as a function of q. For an acoustic phonon the energy integrated phonon intensity for a constant $\mathbf{Q}$ scan can be written as [120]:

$$\int_{-\infty}^{\infty} I(\mathbf{Q},\hbar\omega)d(\hbar\omega) = A\frac{1}{1-e^{-\frac{\hbar\omega(q)}{k_BT}}}\frac{(\hbar\mathbf{Q})^2}{\hbar\omega(q)}cos^2\beta, \tag{6.2}$$

where $\omega(q)$ refers to the acoustic phonon frequency, β is the angle between $\mathbf{Q}$ and the unit vector along the phonon polarization direction and A is assumed to be a constant. In Eq. 6.2 the $\hbar\omega(q)$ term can be substituted by $v\hbar q$, since the experimentally determined dispersion curve for the TA[1 0 0]$_{\langle 001\rangle}$ seems to be linear in most part of the Brillouin zone. The experimental data in Fig. 6.3(b) are well described by such a fit. This indicates that around $\mathbf{G}$=(0, 0, 4) in transverse geometry ($\mathbf{q} \parallel$[1 0 0]) and in the energy

transfer range of $-15 < E < 15$ meV only single phonon excitations are measured. Therefore, the large width broadening shown in Fig. 6.3(a) might not be caused by a merging of the TA[1 0 0]$_{\langle 001 \rangle}$ with low lying TO phonons that cannot be resolved due to instrumental resolution limitations.

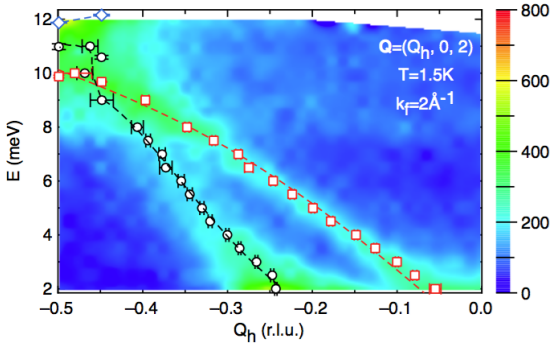

Figure 6.4: Colour map constructed from **Q** scans around **Q**=(Q_h, 0, 2) at constant energy transfers $2 \leq E \leq 12$ meV at T=1.5 K. Data were obtained with unpolarized neutrons at IN12. Circles, squares and diamonds correspond, respectively, to magnons, TA and TO phonons, as determined from unpolarized and polarized INS data (see details in text). The lines are guides for the eyes.

To clarify if the broadening of the TA[1 0 0]$_{\langle 001 \rangle}$ phonon is due to spin-phonon interaction, INS measurements were performed in a Brillouin zone where both types of excitations are observed with good resolution. To this aim, constant E scans around **Q**=(Q_h, 0, 2) were carried out at energy transfers below 14 meV at T=1.5 K with unpolarized neutron beam at IN12. The resulting TA phonon and magnon dispersion curves are shown in Fig. 6.4 in the form of a colour map. For energy transfers $2 \leq E \leq 7$ meV the phonon and the magnon are well separated, although they originate from the same zone center **G**=(0, 0, 2). Magnetic and lattice excitations for the constant E scans (for $E \leq 7$ meV) were fitted with Gaussian functions. Consistently with the dispersion curves along the $\Gamma-$M direction (see in Fig. 6.2), the dispersion relations as a function of q (see Fig. 6.4) for the TA[1 0 0]$_{\langle 001 \rangle}$ phonon and the magnon for $E \leq 7$ meV are linear and quadratic, respectively. For increasing energy transfers and close to the Brillouin zone boundary, an increase of intensity is observed. However, the signal arising from the individual excitations cannot be distinguished from the unpolarized INS data.

To disentangle the lattice and magnetic excitations at $E > 7$ meV, constant E and constant **Q** scans with polarized neutrons were carried out at IN12. Figs 6.5(a)-(e) show such characteristic scans around **Q**=(Q_h, 0, 2) in the NSF$_{zz}$ and SF$_{zz}$ channels (see Eq. 2.24 in Section 2.2.6.2 and further details in Section 4.3). In the **Q** scans shown in Figs 6.5(a)-(c) as the energy transfer increases both excitations approach the Brillouin zone boundary and until E=9 meV they do not intersect. The crossing of the TA[1 0 0]$_{\langle 001 \rangle}$ phonon and the magnon is observed at E=10 meV and at the intersecting point the intensities of the modes are almost equal (see Fig. 6.5(c)). For measurements close to the zone boundaries where the dispersions become flat, constant **Q** scans were employed (see Figs 6.5(d)-(e)). Such scans are characterized by a broad peak observed in the SF$_{zz}$ channel that corresponds to spin-wave scattering and by two very well defined peaks observed in the NSF$_{zz}$ channel identified as phonon excitations. The peaks appearing in the NSF$_{zz}$ channel were fitted with DHO functions and correspond to a TA and a TO mode. Commonly with Fig. 6.3(a) the linewidth of the TA[1 0 0]$_{\langle 001 \rangle}$ phonon is increasing with q, but to draw firm conclusions

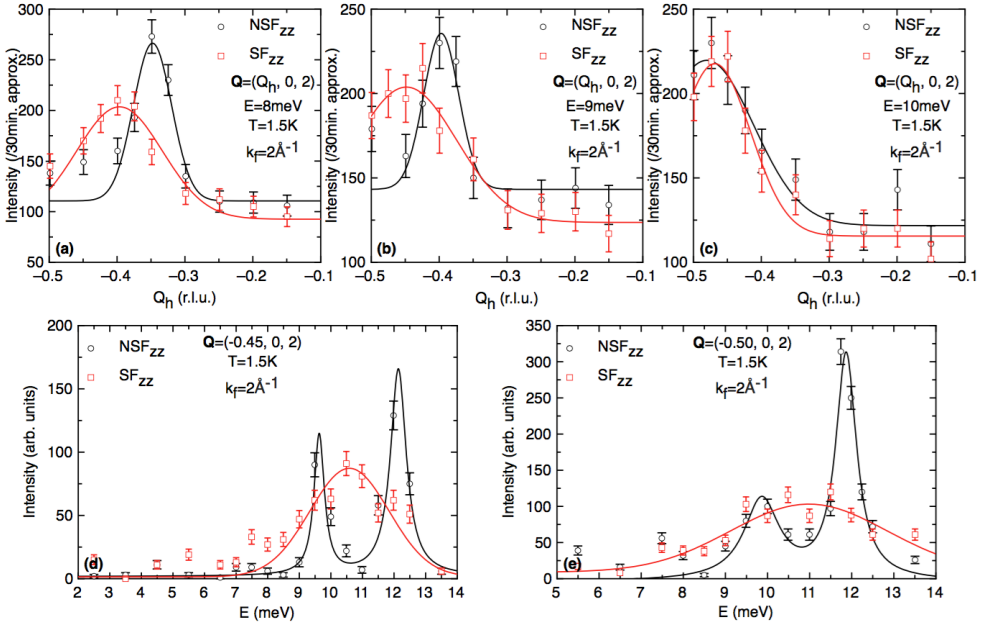

Figure 6.5: Typical polarized INS spectra obtained at IN12 at T= 1.5K around **Q**=(Q_h, 0, 2) in the NSF$_{zz}$ and SF$_{zz}$ channels. A vertical magnetic field of H_z=1 T is applied parallel to the b-axis of the hexagonal system. The monitor counts for all scans were 2·10^6. Figs (a)-(c) show raw data from constant E scans and the lines indicate fits with Gaussian functions. Figs (d)-(e) show constant **Q** scans where the background is subtracted and the lines for the NSF$_{zz}$ and SF$_{zz}$ channels represent fits with DHO and Gaussian functions, respectively.

concerning the intrinsic linewidth the scattering function should be convoluted with the 4D instrument resolution. In addition, it should be noted that the combination of the constant E and constant **Q** scans points to a "kink" in the magnon spectrum along the $\Gamma-$M direction occurring around the crossing points of the phonon and magnon modes at q=0.45 r.l.u. (see Fig. 6.4). This observation might hint to an opening of an energy gap or discontinuity in the magnon spectrum which could indicate possible phonon-magnon coupling.

6.5 Nuclear-magnetic interference

In order to further investigate a possible phonon-magnon interaction, polarized INS experiments were performed using spin flippers before and after the sample to access the four possible longitudinal polarized INS cross-sections NSF$_{zz}^{++}$, NSF$_{zz}^{--}$, SF$_{zz}^{+-}$ and SF$_{zz}^{-+}$, where $+$ and $-$ stands for flipper on and off, respectively. The polarized INS experiments were undertaken under a vertical magnetic field of H_z=1 T giving rise to a single domain FM sample (see details in Section 4.2). Figs 6.6 show unpolarized and polarized constant E neutron spectra obtained at T=1.5 K around **Q**=(Q_h, 0, 2). The peaks observed in both spectra are peaked in the same Q_h positions and are more prominent at Q_h <0 due to the instrumental resolution focusing conditions. As can be seen in Fig. 6.6(b) the magnon has equal intensity in both SF channels (SF$_{zz}^{+-}$ and SF$_{zz}^{-+}$) as expected, in contrast to the TA[1 0 0]$_{\langle 001\rangle}$ phonon that has significant

intensity in only one NSF channel (NSF_{zz}^{++}), while in the other NSF channel (NSF_{zz}^{--}) the intensity is equal to the background level. Such unbalance of intensities between the two NSF channels could be attributed to the nuclear-magnetic interference (NMI) term: $I_{NSF}^{++} - I_{NSF}^{--} = 2 \mid P_0 R_z \mid$ (see Eq. 2.25 in Section 2.2.6.2). This complete cancellation of intensity in the NSF_{zz}^{--} channel is observed in the TA[1 0 0]$_{\langle 001 \rangle}$ phonon mode for low energy transfers, e.g. at E <6 meV, far below the crossing point of phonons and magnons (see Fig. 6.7(a)). Close to the Brillouin zone boundary and at the intersecting point of phonons and magnons (see Fig. 6.4 and Fig. 6.5(c)) the intensity is restored in the NSF_{zz}^{--} channel as can be seen in Fig. 6.7(b).

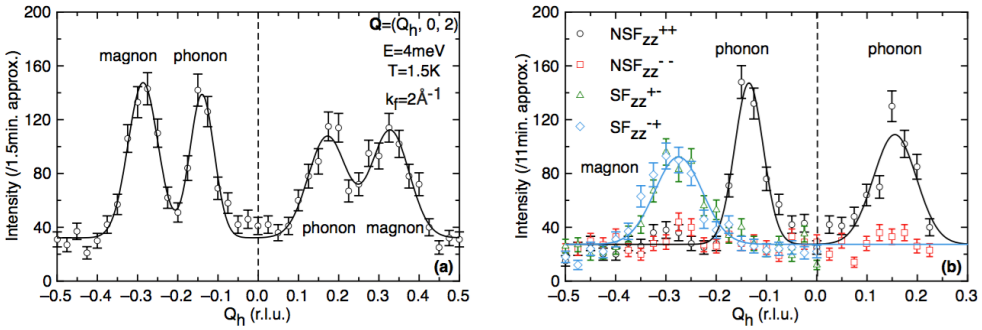

Figure 6.6: Inelastic spectra obtained with (a) unpolarized and (b) polarized neutron beam at IN12 around $\mathbf{Q}$=(Q_h, 0, 2) for E=4 meV energy transfer at T=1.5 K. The symbols + and − refer to flipper on and off, respectively. For the polarized spectra a constant vertical magnetic field of H_z=1 T is applied. The lines indicate fits with Gaussian functions.

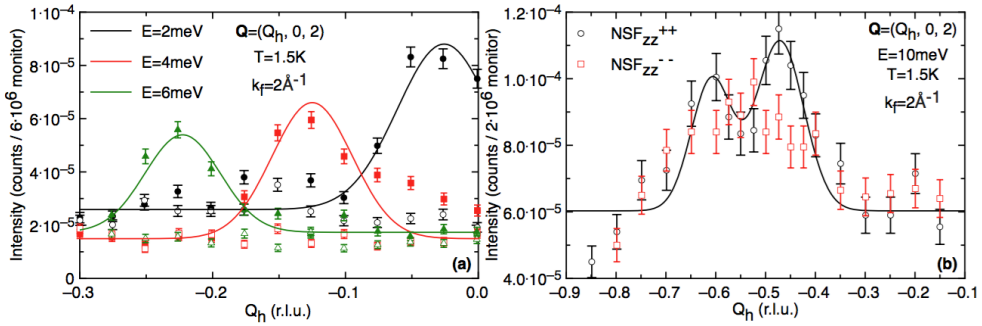

Figure 6.7: Raw data obtained at IN12 with polarized neutrons from two NSF channels at T=1.5 K (a) below and (b) at the crossing point of phonons and magnons. The spectra were measured around $\mathbf{Q}$=(Q_h, 0, 2) at different constant energy transfers and under constant vertical magnetic field H_z=1 T. In Fig. (a) the full and open symbols correspond to the NSF_{zz}^{++} and NSF_{zz}^{--} channel, respectively. The lines indicate fits with Gaussian functions.

To characterize the evidenced NMI term in $MnFe_4Si_3$, its temperature dependence was studied above and below T_C (see Figs 6.8). Inelastic (around $\mathbf{Q}$=(Q_h, 0, 2) at constant energy transfer E=4 meV) and elastic (around the Bragg position $\mathbf{Q}$=(0, 0, 2)) spectra were collected in the NSF_{zz}^{++} and NSF_{zz}^{--} channels under a vertical magnetic field of H_z=1 T. During the temperature change the lattice parameters were corrected when necessary. As can be seen in Fig. 6.8(a) in the PM state (T=315 K) an unbalance of

intensities is observed between the two NSF channels for the TA[1 0 0]$_{\langle 001 \rangle}$ phonon. As the temperature decreases, the intensity I^{--}_{NSF} decreases drastically and at T=290 K equals almost to the background level. Fig. 6.8(e) shows the temperature dependence of the NMI term. It depicts the difference of the phonon intensities in the two NSF channels in the peak position $\mathbf{Q}$=(−0.15, 0, 2) at 4 meV. The background measured at $\mathbf{Q}$=(−0.30, 0, 2) at 4 meV was subtracted and the measured intensity was corrected by the detailed balance factor. For the elastic scans at the Bragg position $\mathbf{Q}$=(0, 0, 2) a similar unbalance of intensities is evidenced in the two NSF channels, however, a complete cancelation in intensity is not observed. For elastic scattering the difference of intensities between the two polarization channels equals ${}^{\mathrm{el}}I^{++}_{\mathrm{NSF}} - {}^{\mathrm{el}}I^{--}_{\mathrm{NSF}} = 4F_N(\mathbf{Q})F_M(\mathbf{Q})$ (see Eq. 3.1 in Section 3.2) and its temperature dependence is shown in Fig. 6.8(f). It seems that the temperature dependence of the inelastic and elastic NMI term mimics the one of the magnetic order parameter (with finite value above T_C due to the finite magnetic field of H_z=1 T, see Appendix A.4). Measurements of the LA[1 0 0] and TA[0 0 1]$_{\langle 100 \rangle}$ branches and in other Brillouin zones reveal NMI term as well, but with sizeable intensity in both I^{++}_{NSF} and I^{--}_{NSF} channels. The corresponding raw data and the temperature dependence of the inelastic and elastic NMI term can be found in the Appendix A.4.

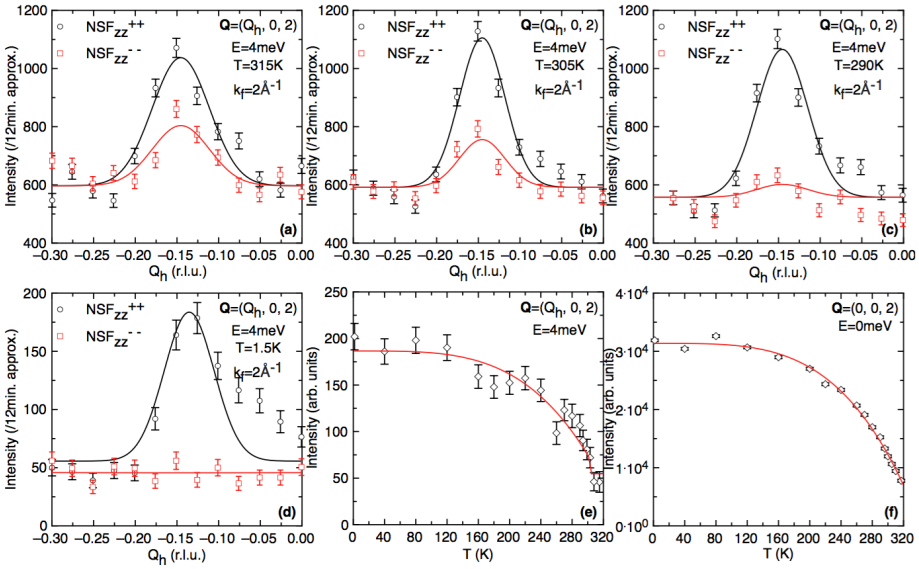

Figure 6.8: (a)-(d) Polarized INS spectra around $\mathbf{Q}$=(Q_h, 0, 2) at constant E=4 meV obtained at different temperatures. Temperature dependence of (e) $2|\ P_0R_z\ | = I^{++}_{\mathrm{NSF}} - I^{--}_{\mathrm{NSF}}$ and (f) $4F_N(\mathbf{Q})F_M(\mathbf{Q}) = {}^{\mathrm{el}}\mathbf{I}^{++}_{\mathrm{NSF}} - {}^{\mathrm{el}}\mathbf{I}^{--}_{\mathrm{NSF}}$ (see details in text). The lines in Figs (a)-(d) and Figs (e)-(f) indicate fits with Gaussian functions and guides for the eyes, respectively. All data have been collected under a vertical magnetic field of 1 T at IN12.

6.6 Discussion

The combination of IXS and INS measurement allowed to determine the low lying lattice and magnetic excitations in $MnFe_4Si_3$ single crystals. The observed broadening of the phonon linewidths at the crossing

points of TA phonons and magnons along the $\Gamma-$M might be attributed to phonon-magnon coupling [115]. Indications of a "jump" in the spin-wave spectrum close to the Brillouin zone boundary also point to this direction. While performing longitudinal polarized INS experiments in order to establish phonon-magnon interaction, an unbalance of intensities between the two NSF polarization channels was observed for the TA[1 0 0]$_{\langle 001 \rangle}$ phonon mode. This effect is ascribed to the NMI [78].

The NMI term is reported in polarized neutron diffraction experiments aiming to measure magnetic form factors and spin densities [78]. The NMI terms are not often reported in INS experiments and, to the knowledge of the author, were never observed for magnetic excitations. This is related to the fact that NMI correlation functions are linear in the magnetic operator and their observation is conditional upon the breaking of certain symmetry in the system (time reversal or/and parity). In the present case, the applied magnetic field (resulting in a single FM domain in the sample) meets this condition. Among other ferromagnets, a similar unbalance of intensities as the one observed here in the two NSF channels was reported in the phonon spectrum of Ni and Fe [121] and of $Fe_{65}Ni_{35}$ [122]. Its origin was attributed to magneto-vibrational scattering; a term which is elastic in the magnetic system and inelastic with respect to the phonons [70].

In the case of $MnFe_4Si_3$, a rather unusual feature is observed. It is evidenced that for the TA[1 0 0]$_{\langle 001 \rangle}$ phonon mode a complete cancelation of intensity in the NSF$^{--}_{zz}$ channel occurs in the whole energy range of the phonon spectrum before the crossing point with the magnon. At the intersecting point of phonons and magnons the intensity is partly restored in the NSF$^{--}_{zz}$ channel and a significant NMI term is still remaining. The temperature dependence of the NMI term in the low lying part of the dispersion mimics the one of the magnetic order parameter. This might suggest that the observed NMI term is elastic in the magnetic subsystem, which in return could hint to magneto-vibrational scattering. However, it is not clear yet if it is originating from magneto-vibrational scattering as claimed for other FM compounds [121, 122] or from more "exotic" scattering involving in a different manner interaction between magnetic and lattice degrees of freedom. Since changes in temperature and low magnetic fields are major parameters for the MCE, further studies of the inelastic NMI term in $MnFe_4Si_3$ are necessary under the influence of the above mentioned external parameters. This might be an essential step towards understanding the origin of the behaviour of the NMI term in this compound.

6.7 Conclusions

In the MC compound $MnFe_4Si_3$ the phonon modes were unambiguously determined by IXS measurements, while the magnon modes were unambiguously determined by a combination of unpolarized and polarized INS data. It is demonstrated that along the $\Gamma-$M high symmetry direction of the hexagonal system, the magnon branch close to the zone boundary intersects with the TA[1 0 0]$_{\langle 001 \rangle}$ phonon branch. At the intersecting point there are hints of a "kink" in the magnon spectrum, while the phonon linewidths increase abruptly. Moreover, it is evidenced that for this particular phonon mode the complete cancelation of intensity observed in the NSF$^{--}_{zz}$ channel in the low energy part of its dispersion, that is attributed to NMI, is lifted exactly at the intersecting point of the modes. Altogether these observations could point to possible phonon-magnon interaction. Establishing the origin of the observed NMI in this system could pave the way for first microscopic explanations of the MCE not only in $MnFe_4Si_3$, but also in other MC compounds.

Chapter 7

Summary and Outlook

Caloric effects are inherent to magnetization processes. The degree of order of a magnetic system determines the number of accessible states, which in turn defines its magnetic entropy. The Maxwell relation $\left(\frac{\partial S}{\partial H}\right)_{T,p} = \left(\frac{\partial M}{\partial T}\right)_{H,p}$ relates the entropy $S(T,H)$ and the magnetization $M(T,H)$ of a system under constant pressure. This shows that any temperature dependence of the magnetization is coupled to an entropy change when varying the magnetic field. Two well-known realizations are the adiabatic demagnetization of PM salts to reach sub-Kelvin temperatures and the giant MCE observed near room temperature magneto-structural phase transitions.

The MCE can be potentially exploited for magnetic refrigeration. Several MC materials made for abundant, cheap and non-toxic elements, such as the $Mn_{5-x}Fe_xSi_3$ series, have been proposed for solid state cooling devices. In order to highlight the major components at play and to finally optimize the MC materials in view of applications, microscopic studies with a probe that reveals the magnetic response of a system as a function of the wave-vector $\mathbf{q}$ and energy E could be ideal. To this aim, INS measurements were performed on single crystals of the MC compounds $MnFe_4Si_3$ and Mn_5Si_3.

The FM compound $MnFe_4Si_3$ could be used for application if optimized, since it exhibits a transformation from the PM state to the FM phase close to room temperature (T_C=305 K). Spin-wave measurements at T=1.5 K reveal a strong anisotropy of the magnetic exchange interactions along the (h00) and (00l) reciprocal directions of the hexagonal system. Spin-wave simulations using the Heisenberg model for magnetism and two FM exchange interactions with values $2SJ_1$=$-$4 meV and $2SJ_2$=$-$18 meV are sufficient to describe the experimentally obtained acoustic magnon spectrum. The strong anisotropy of the magnetic exchange interactions along the in plane and out-of plane hexagonal directions manifests also in the q-dependent linewidths (Γ_q) in the PM state. The experimental data obtained at T=315 K for the Γ_q could be well described both with a model for localized Heisenberg FM, as well as, a model for weak itinerant FM. On the other hand the bare spin correlation lengths ξ_0 are smaller than the lattice parameters a and c, which points to a localized feature of the magnetism of $MnFe_4Si_3$. Such short range magnetic correlations in the PM state might be important ingredient for the MCE in $MnFe_4Si_3$. In the present study it is also demonstrated that the in- and out-of-plane spin-fluctuations, which are isotropic around T_C, can be suppressed by a magnetic field of 2 T. The observed suppression of the spin-fluctuations is qualitatively well described by a model that estimates the q-dependent susceptibility under a finite external magnetic field using the Landau theory for the magnetic fluctuations.

The parent compound Mn_5Si_3 exhibits two first order phase transitions towards AF phases at

T_{N_2}≈100 K (AF2) and T_{N_1}≈66 K (AF1), respectively. The inverse MCE, the cooling by adiabatic magnetization, is associated in Mn_5Si_3 with the AF1-AF2 phase transition. In this study, INS experiments reveal that the low temperature AF1 phase (T <66 K) is characterized by well-defined spin-waves, while the higher temperature AF2 phase (66< T <100 K) is characterized by a coexistence of spin-waves and diffuse spin-fluctuations. It is also demonstrated that the modification of the magnetic excitation spectrum at 50 K as a function of magnetic field is identical to the one as a function of temperature at H=0 T. Therefore, one concludes that an external applied magnetic field in the AF1 phase restores the fluctuations pattern associated with the AF2 phase. In contrast to the discrete spin-wave spectrum of the AF1 phase, such spin-fluctuations consist of a continuum of excitations involving more microscopic states. Consistently, this leads to an increase of the magnetic entropy and thus plays a major role in the inverse MCE in Mn_5Si_3. The observed behaviour is opposite to the most common magnetic field effect that usually suppresses the spin-fluctuations and consequently decreases the magnetic entropy (direct MCE) as demonstrated by INS in the FM compound $MnFe_4Si_3$.

To investigate possible interaction between the lattice and magnetic degrees of freedom in $MnFe_4Si_3$, a combination of IXS and INS measurements was used. The low lying phonon modes were unambiguously determined by the IXS data, while the magnon modes were unambiguously determined by a combination of unpolarized and polarized INS data. The up to now measured excitations hint to a "kink" in the magnon spectrum along the (h00) direction occurring at the crossing point of the TA phonons and magnon branches. It is worthwhile to note that the spin-waves near the Brillouin zone boundary along (h00) fall exactly on the two TA phonons. Furthermore, one TA mode shows in polarized INS measurements an unusual behaviour for both NSF channels, i.e. complete cancellation of intensity for one channel, which could be assigned to a NMI term. The temperature dependence of the inelastic NMI term mimics the one of the magnetic order parameter. This suggests that the observed NMI term is elastic in the magnetic subsystem, which in return might hint to a magneto-vibrational scattering term like it was suggested for other FM compounds, e.g., Fe and Ni. Further studies of the inelastic NMI term in $MnFe_4Si_3$ under the influence of temperature and magnetic field are necessary in order to understand its origin and relate it with the MCE.

In future one next step for both compounds could be the combination of experimental and theoretical studies. Determining further the low energy optic phonons along the high symmetry reciprocal directions and comparing the experimentally obtained dispersions with DFT calculations might help to understand the electronic ground states of these systems. Exploring possible optic magnon branches with INS will allow to determine all exchange interactions for Mn_5Si_3 and $MnFe_4Si_3$. Additional studies of the effect of temperature and magnetic field on the lattice and magnetic excitations, as well as phonon-magnon interactions can be envisaged. The knowledge of the fundamental interactions like the lattice excitations in parallel to the spin-wave spectrum could be an essential step towards understanding the mechanisms of the MCE (direct and inverse) and might help designing new materials in the future.

Appendix A

Appendix

A.1 Spin-wave simulations of $MnFe_4Si_3$

A.1.1 Input file for SpinWave software package

The SpinWave software package uses linear spin-wave theory for simulating magnon spectra [86]. The SpinWave input file is a simple .text file that can be edited with any standard editor. Below one can find the .text file used to describe the magnon spectrum of $MnFe_4Si_3$.

```
! ———————————————————-
! MnFe4Si3
!
! definition of the magnetic unit cell
!
AX = 6.78
AY = 6.78
AZ = 4.72
ALFA= 90.0
BETA= 90.0
GAMA= 120.0
!
! ———————————————————-
! position of the spins
! NOM=name of the spin, SD2 = spin 1/2
! (SX,SY,SZ) or PHI, THETA initial guess of the spin directions
! (CX,CY,CZ) CEF axis, B20 = stevens coefficient, describing the anisotropy
!
I=1, NOM=S1, X= 0.23556, Y= 0.00000, Z=0.75, PHI=120, THETA=90, CZ=1, B20=0.1
I=2, NOM=S1, X= 0.00000, Y= 0.23556, Z=0.75, PHI=120, THETA=90, CZ=1, B20=0.1
I=3, NOM=S1, X= 0.76444, Y= 0.76444, Z=0.75, PHI=120, THETA=90, CZ=1, B20=0.1
!
I=4, NOM=S1, X= 0.76444, Y= 0.00000, Z=0.25, PHI=120, THETA=90, CZ=1, B20=0.1
I=5, NOM=S1, X= 0.00000, Y= 0.76444, Z=0.25, PHI=120, THETA=90, CZ=1, B20=0.1
```

```
I=6, NOM=S1, X= 0.23556, Y= 0.23556, Z=0.25, PHI=120, THETA=90, CZ=1, B20=0.1
!
! ———————————————————-
! couplings (anisotropic in that case but diagonal)
!
I1=1, I2=5, J1=−18, D1=2.9
I1=2, I2=6, J1=−18, D1=2.9
I1=3, I2=4, J1=−18, D1=2.9
!
I1=1, I2=6, J1=−18, D1=2.9
I1=2, I2=4, J1=−18, D1=2.9
I1=3, I2=5, J1=−18, D1=2.9
!
I1=1, I2=4, J1=0, D1=4, J2=−4, D2=4.4
I1=2, I2=5, J1=0, D1=4, J2=−4, D2=4.4
I1=3, I2=6, J1=0, D1=4, J2=−4, D2=4.4
!
! ———————————————————-
! definition of the scan
!
Q0X=0.00, Q0Y=0.00, Q0Z=0.00
DQX=0.01, DQY=0.00, DQZ=0.00
NP=1001
!
! ———————————————————-
! calculation
!
! name of the output file
FICH=Fout.txt
!
FFORM
! method, with REG a regularization term (should be small compared to J)
CALC=2, REG1=0.05, REG2=0.05, REG3=0.05
!
! MF iterations to find the stable structure
MF, NITER=100
! WMAX= max energy, NW number of energy points, SIG=energy width
WMAX=100, NW=100, SIG=1
```

A.1.2 Simulation of optic magnons and powder average of $MnFe_4Si_3$

The spin-wave model using two FM exchange interactions with values $2SJ_2$=−18 meV and $2SJ_1$=−4 meV generates optic magnons at energy transfers $30<E<60$ meV along the (00l), (h00) and (hh0) directions. Fig. A.1(a) shows optic magnons along the (h00) direction. The corresponding calculation of the powder-averaged spin-wave spectrum of $MnFe_4Si_3$ is shown in Fig. A.1(b).

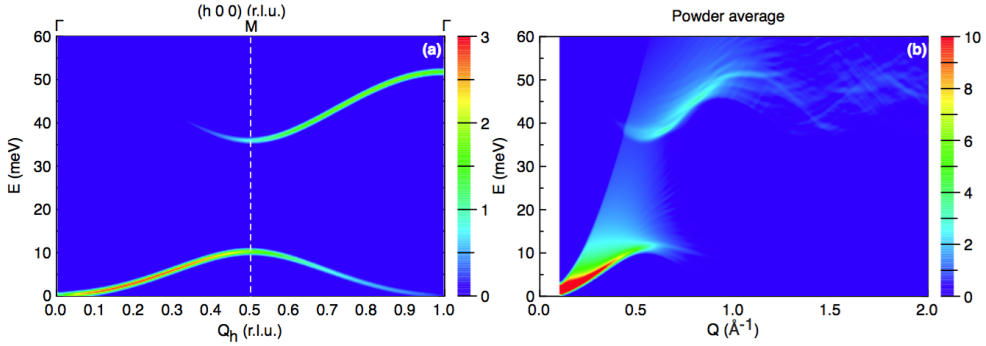

Figure A.1: Simulation of (a) optic magnons along the (h00) direction and (b) powder average of $MnFe_4Si_3$ using two FM exchange parameters with values $2SJ_2$=−18 meV and $2SJ_1$=−4 meV. The vertical white dashed line indicates the Brillouin zone boundary.

The optic magnon modes are strongly affected by introducing in the spin-wave model an additional coupling $2SJ_0$ between the magnetic atoms located on a triangle (shortest distance 2.775 Å) in the same distorted $[MnFe]_6$ octahedra (see Fig. 4.6 and Table 4.2 in Section 4.3). If the exchange interaction is FM, e.g. $2SJ_0$=−50 meV, then the optic modes shift to higher energies, while the in-plane acoustic magnon modes remain unaffected (see Fig. A.2(a)). If the exchange interaction is AF, e.g. $2SJ_0$=10 meV, then the optic modes shift to lower energies and the acoustic modes are also modified (see Fig. A.2(b)). From the obtained data shown in Fig. 4.5 in Section 4.3 it is not possible to determine the interaction $2SJ_0$.

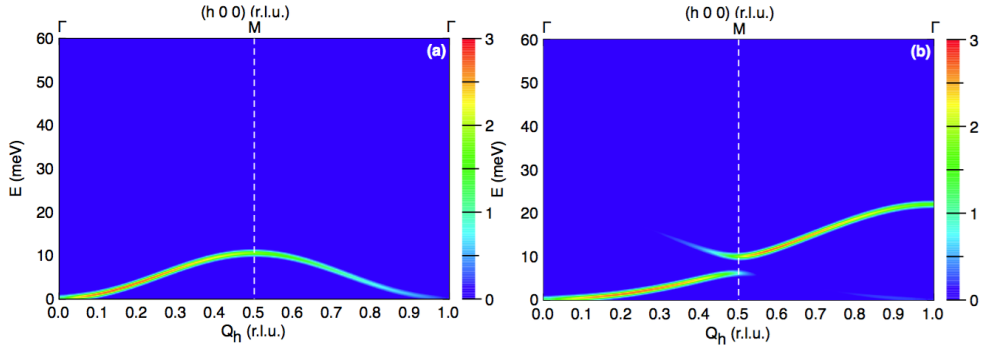

Figure A.2: Simulation of the magnon spectrum of $MnFe_4Si_3$ along the (h00) direction using FM exchange parameters with values $2SJ_2$=−18 meV and $2SJ_1$=−4 meV and introducing another exchange interaction $2SJ_0$. Resulting spin-wave simulations (a) for $2SJ_0$=−50 meV (FM exchange interaction) and (b) for $2SJ_0$=10 meV (AF exchange interaction). The vertical white dashed line indicates the Brillouin zone boundary.

A.2 Additional INS spectra of Mn_5Si_3

A.2.1 Unpolarized INS spectra of Mn_5Si_3 in the AF2 phase

Fig. A.3 shows unpolarized INS spectra around $\mathbf{Q}=(Q_h, 2, 0)$ at different constant energy transfers in the AF2 phase. It seems that the overall signal consists of several ill-resolved peaks.

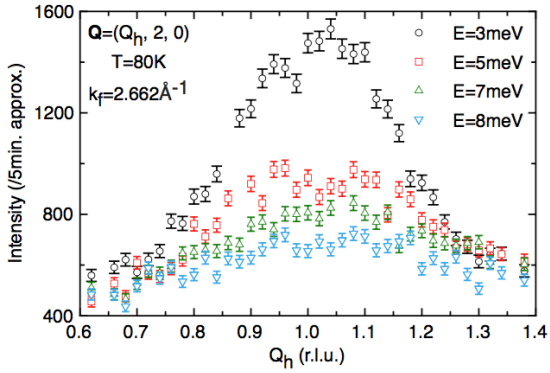

Figure A.3: Raw data obtained at 2T1 with unpolarized neutron beam around $\mathbf{Q}=(Q_h, 2, 0)$ at different constant energy transfers in the AF2 phase (T=80 K).

A.2.2 Unpolarized INS spectra of Mn_5Si_3 in the PM state

INS spectra in the PM state with the corresponding HWHM (as obtained from fits with Lorentzian functions) are shown in Figs A.4. Concerning the signal arising from the spin-fluctuations (see Section 5.5.2), the width of the fluctuations in the AF2 phase in Fig. 5.10(c) is fixed to the one of the PM state (see Fig. 5.10(a)). This is the simplest possible hypothesis and it is rationalised by the temperature and energy

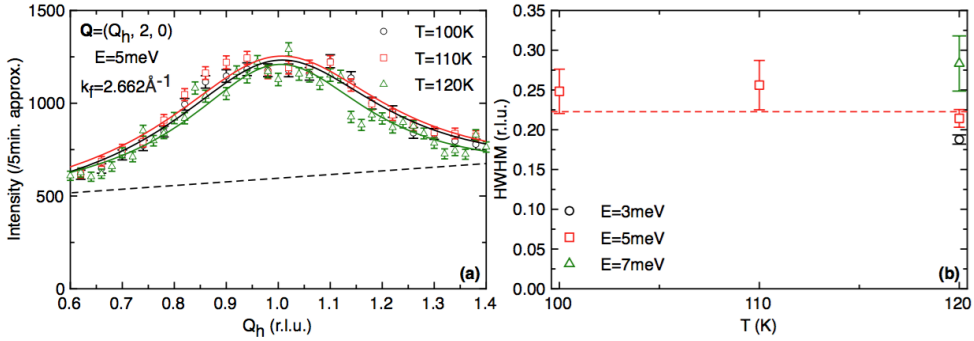

Figure A.4: (a) PM scattering at different temperatures at constant energy transfers of 5 meV around $\mathbf{Q}=(Q_h, 2, 0)$. Solid lines represent fits with Lorentzian functions and the black dashed line the background. Data were obtained at 2T1. (b) HWHM as obtained from fits with Lorentzian functions at different temperatures at E=5 meV (raw data shown in Fig. (a)) and at different energy transfers at T=120 K (raw data shown in Fig. 5.9(b)). The red dashed line indicates the average value of HWHM for 5 meV energy transfer.

variation of this width in the PM state shown in Figs A.4. In the limited range of the studied parameters (3, 5, 7 meV), this width is weakly temperature and energy dependent. It is then dominated by "a constant" term, which could be seen as an intrinsic parameter of the system. This value is assumed to be robust to the AF2 phase.

A.3 Additional IXS spectra of $MnFe_4Si_3$

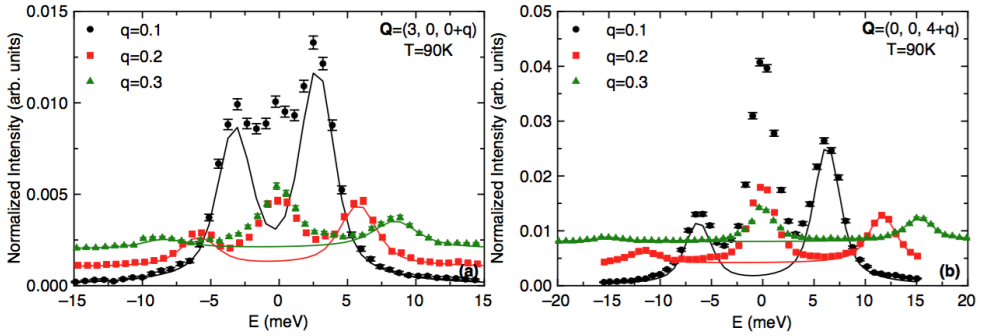

Figure A.5: IXS spectra obtained at ID28 at T=90 K around (a) **Q**=(3, 0, Q_l) and (b) **Q**=(0, 0, Q_l). The solid lines indicate phonon excitations. The counting time per point was 1 minute. The spectra in (a) and (b) are shifted for clarity along the vertical direction by 0.001 and 0.004 normalized counts, respectively, conserving the same intensity scale.

A.4 Additional polarized elastic and inelastic neutron spectra and temperature dependence of the magnetization of $MnFe_4Si_3$

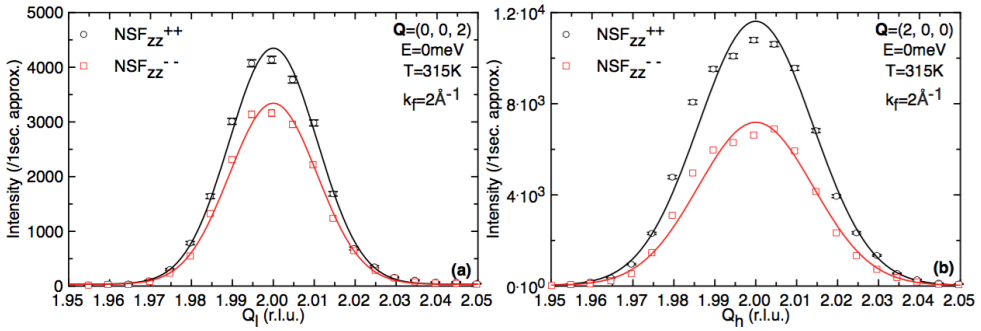

Figure A.6: Raw data obtained at IN12 with polarized neutrons from two NSF channels at T=315 K around the Bragg positions (a) **Q**=(0, 0, 2) and (b) **Q**=(2, 0, 0). The lines indicate fits with Gaussian functions.

A.4. Additional polarized elastic and inelastic neutron spectra and temperature dependence of the magnetization of $MnFe_4Si_3$

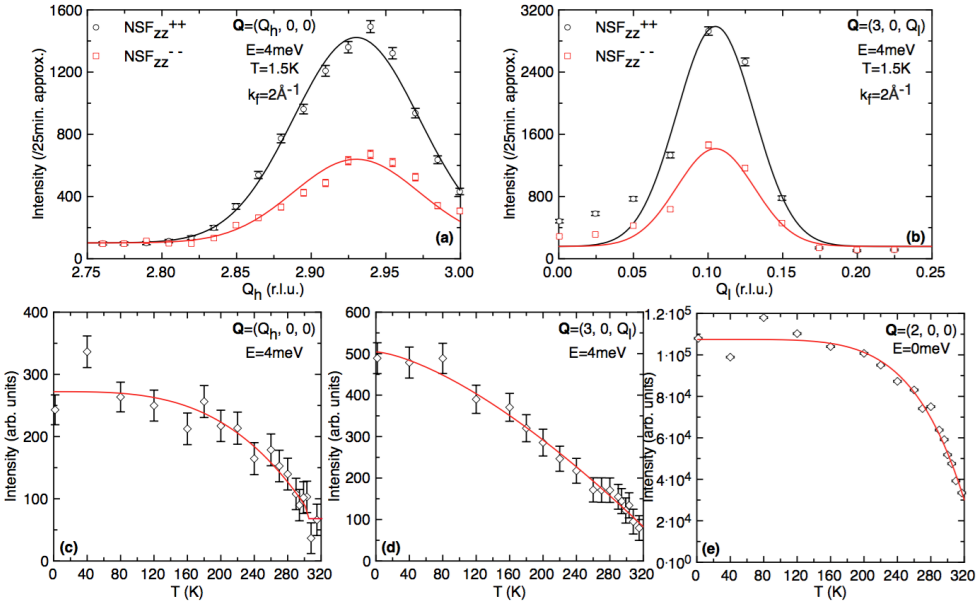

Figure A.7: Polarized INS spectra around (a) **Q**=(Q_h, 0, 0) and (b) **Q**=(3, 0, Q_l) at constant E=4 meV obtained at T=1.5 K. Temperature dependence of the NMI term for the (c) LA[1 0 0] and (d) TA[0 0 1]$_{\langle 100 \rangle}$ phonon modes. (e) Temperature dependence of the NMI term for the Bragg position **Q**=(2, 0, 0). Data points in Figs (c) and (d) correspond to the difference of phonon intensities $I_{\mathrm{NSF}}^{++} - I_{\mathrm{NSF}}^{--}$ in the peaks **Q**=(2.925, 0, 0) and **Q**=(3, 0, 0.1) at 4 meV, respectively. During the temperature change the lattice parameters were corrected when necessary. The counting time was 8 minutes per point. The lines in Figs (a)-(b) and Figs (c)-(e) indicate fits with Gaussian functions and guides for the eyes, respectively. All data have been collected under a vertical magnetic field of 1 T at IN12.

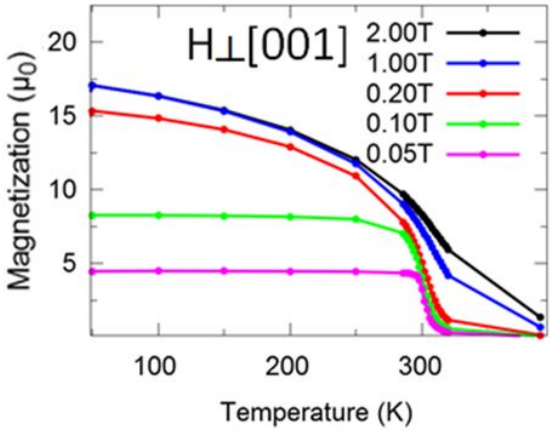

Figure A.8: Temperature dependence of the magnetization of $MnFe_4Si_3$ under different magnetic fields (courtesy of P. Hering). The magnetic fields are applied parallel to the b-axis of the hexagonal system of the single crystal sample.

Appendix B

List of abbreviations

ADM	adiabatic demagnetization
AF	antiferromagnetic
BG	background
ΔS_{iso}	isothermal entropy change
ΔT_{ad}	adiabatic temperature change
DHO	damped harmonic oscillator
ESRF	European Synchrotron Radiation Facility
FI	ferrimagnetic
FM	ferromagnetic
FOPT	first-order phase transition
FWHM	full width at half maximum
HWHM	half width at half maximum
ILL	Institut Laue Langevin
INS	inelastic neutron scattering
IXS	inelastic X-ray scattering
LA	longitudinal acoustic
LLB	Laboratoire Léon Brillouin
LO	longitudinal optic
loc	localized
LPA	longitudinal polarization analysis
MC	magnetocaloric
MCE	magnetocaloric effect
MF	molecular field
MLZ	Heinz Maier-Leibnitz Zentrum

NMI	nuclear-magnetic interference
NSF	non-spin flip
PG	pyrolytic graphite
PM	paramagnetic
SF	spin flip
SOPT	second-order phase transition
TA	transverse acoustic
TAS	triple axis spectrometer
TO	transverse optic
VS	velocity selector
wi	weak itinerant
WP	Wyckoff position

Bibliography

[1] S. Fähler, U. Rössler, O. Kastner, J. Eckert, G. Eggeler, H. Emmerich, P. Entel, S. Müller, E. Quandt & K. Albe. Caloric effects in ferroic materials: new concepts for cooling. Adv. Eng. Mater., **14**, 10 (2012).

[2] X. Moya, S. Kar-Narayan & N. D. Mathur. Caloric materials near ferroic phase transitions. Nat. Mater. **13**, 439 (2014).

[3] I. Takeuchi & K. Sandeman. Solid-state cooling with caloric materials. Physics Today **68**, 48 (2015).

[4] H. Ursic, V. Bobnar, B. Malic, C. Filipic, M. Vrabelj, S. Drnovsek, Y. Jo, M. Wencka & Z. Kutnjak. A multicaloric material as a link between electrocaloric and magnetocaloric refrigeration. Scientific Reports **6**, 26629 (2016).

[5] V. Franco, J. S. Blázquez, B. Ingale & A. Conde. The magnetocaloric effect and magnetic refrigeration near room temperature: materials and models. Annu. Rev. Mater. Res. **42**, 305 (2012).

[6] E. Warburg. Magnetische Untersuchungen über einige Wirkungen der Koerzitivkraft. Ann. Phys. (Leipzig) **13**, 141 (1881).

[7] N. Tesla. Pyromagneto-electric generator. US patent 0,428,057 (May 18, 1890).

[8] T. A. Edison. Pyromagnetic generator. US patent 0,476,983 (June 14, 1892).

[9] P. Weiss & A. Piccard. Sur un nouveau phénoméne magnétocalorique. Compt. Rend. Ac. Sci. **166**, 352 (1918).

[10] P. Debye. Einige Bemerkungen zur Magnetisierung bei tiefer Temperatur. Ann. Phys., **81**, 1154 (1926).

[11] W. F. Giauque. A thermodynamic treatment of certain magnetic excess. A proposed method of producing temperatures considerably below 1 ° absolute J. Amer. Chem. Soc., **49**, 1864 (1927).

[12] W. F. Giauque & I. P. D. McDougall. Attainment of temperatures below 1 ° absolute by demagnetization of $Gd_2(SO_4)_3 \cdot 8H_2O$. Phys. Rev., **43**, 768 (1933).

[13] G. V. Brown. Magnetic heat pumping near room temperature. J. Appl. Phys. **47**, 3673 (1976).

[14] C. Zimm, A. Jastrab, A. Sternberg, V. Pecharsky, K. Gschneidner Jr., M. Osborne & I. Anderson. Description and performance of a near-room temperature magnetic refrigerator. Adv. Cryog. Eng. **43**, 1759 (1998).

[15] K. A. Gschneidner, Jr. & V. K. Pecharsky. Magnetocaloric materials. Annu. Rev. Mater. Sci. **30**, 387 (2000).

[16] A. M. Tishin & Y. I. Spichkin. The magnetocaloric effect and its applications. IOP Publishing, Bristol (2003).

[17] V. K. Pecharsky & K. A. Gschneidner, Jr.. Giant magnetocaloric effect in $Gd_5(Si_2Ge_2)$. Phys. Rev. Lett. **78**, 4494 (1997).

[18] O. Tegus, E. Brück, K. H. J. Buschow & F. R. de Boer. Transition-metal-based magnetic refrigerants for room-temperature applications. Nature **415**,150 (2002).

[19] B. Yu, M. Liu, P. W. Egolf & A. Kitanovski. A review of magnetic refrigerator and heat pump prototypes built before the year 2010. Int. J. Refrig. **33**, 1029 (2010).

[20] N. A. de Oliveira, P. J. von Ranke & A. Troper. Magnetocaloric and barocaloric effects: Theoretical description and trends. Int. J. Refrig. **37**, 237 (2014).

[21] V. K. Pecharsky, K. A. Gschneidner Jr., A. O. Pecharsky & A. M. Tishin. Thermodynamics of the magnetocaloric effect. Phys. Rev., **64**, 144406 (2001).

[22] J. Lyubina, M. D. Kuz'min, K. Nenkov, O. Gutfleisch, M. Richter, D. L. Schlagel, T. A. Lograsso & K. A. Gschneidner Jr. Magnetic field dependence of the maximum magnetic entropy change. Phys. Rev., **83**, 012403 (2011).

[23] J. Liu, T. Gottschall, K. P. Skokov, J. D. Moore & O. Gutfleisch. Giant magnetocaloric effect driven by structural transitions. Nature Mater. **11**, 620 (2012).

[24] K. Engelbrecht, J. B. Jensen & C. R. H. Bahl. Experiments on a modular magnetic refrigeration device. Stroj. Vestn. J. Mech. E **58**, 3 (2012).

[25] J. D. Moore, K. Morrison, G. K. Perkins, D. L. Schlagel, T. A. Lograsso, K. A. Gschneidner Jr., V. K. Pecharsky & L. F. Cohen. Metamagnetism seeded by nanostructural features of single-crystalline $Gd_5Ge_2Si_2$. Adv. Mater. **21**, 3780 (2009).

[26] J. Lyubina, K. Nenkov, L. Schultz & O. Gutfleisch. Multiple metamagnetic transitions in the magnetic refrigerant $La(Fe,Si)_{13}H_x$. Phys. Rev. Lett. **101**, 177203 (2008).

[27] A. Fujita, S. Fujieda, Y. Hasegawa & K. Fukamichi. Itinerant-electron metamagnetic transition and large magnetocaloric effects in $La(Fe_xSi_{1-x})_{13}$ compounds and their hydrides. Phys Rev. B **67**, 104416 (2003).

[28] F. X. Hu, B. G. Shen, J. R. Sun, Z. H. Cheng, G. H. Rao & X. X. Zhang. Influence of negative lattice expansion and metamagnetic transition on magnetic entropy change in the compound $LaFe_{11.4}Si_{1.6}$. Appl. Phys. Lett. **78**, 3675 (2001).

[29] A. Yan, K. H. Müller, L. Schultz & O. Gutfleisch. Magnetic entropy change in melt-spun MnFePGe. J. Appl. Phys. **99**, 08K903 (2006).

[30] M. Phan & S. Yu. Review of the magnetocaloric effect in manganite materials. J. Magn. Magn.Mater. **308**, 325 (2007).

[31] X. X. Zhang, J. Tejada, Y. Xin, G. F. Sun, K. W. Wong & X. Bohigas. Magnetocaloric effect in $La_{0.67}Ca_{0.33}MnO_{\delta}$ and $La_{0.67}Y_{0.07}Ca_{0.33}MnO_{\delta}$ bulk materials. Appl. Phys. Lett. **69**, 3596 (1996).

[32] M. Pekala, V. Drozd, J. F. Fagnard & P. Vanderbemden. Magnetocaloric effect in nano- and polycrystalline manganites $La_{0.5}Ca_{0.5}MnO_3$. J. Alloys Compd. **507**, 350 (2010).

[33] K. S. Kim, S. G. Min, S. C. Yu, S. K. Oh, Y. C. Kim & K. Y. Kim. The large magnetocaloric effect in amorphous $Fe_{91-x}Y_xZr_9$ (x = 0, 5, 10) alloys. J. Magn. Magn. Mater. **304**, E642 (2006).

[34] V. Franco, C. F. Conde, J. S. Blázquez, A. Conde, P. Švec, D. Janičkovič & L. F. Kiss. A constant magnetocaloric response in FeMoCuB amorphous alloys with different Fe/B ratios. J. Appl. Phys. **101**, 093903 (2007).

[35] S. G. Min, K. S. Kim, S. C. Yu, Y. C. Kim, K. Y. Kim, K. W. Lee, J. R. Rhee, S. Y. Cha & Y. S. Kim. The magnetic entropy change on amorphous FeMnZr alloys. J. Magn. Magn. Mater. **310**, 2820 (2007).

[36] T. Krenke, E. Duman, M. Acet, E. F. Wassermann, X. Moya, L. Mañosa & E. Planes. Inverse magnetocaloric effect in ferromagnetic Ni-Mn-Sn alloys. Nature Mater. **4**, 450 (2005).

[37] M. Khan, N. Ali & S. Stadler. Inverse magnetocaloric effect in ferromagnetic $Ni_{50}Mn_{37+x}Sb_{13-x}$ Heusler alloys. J. Appl. Phys. **101**, 053919 (2007).

[38] S. Aksoy, T. Krenke, M. Acet, E. F. Wassermann, X. Moya, L. Mañosa & E. Planes.. Tailoring magnetic and magnetocaloric properties of martensitic transitions in ferromagnetic Heusler alloys. Appl. Phys. Lett. **91**, 241916 (2007).

[39] J. Liu, T. Gottschall, K. P. Skokov, J. D. Moore & O. Gutfleisch. Giant magnetocaloric effect driven by structural transitions. Nature Mater. **11**, 620 (2012).

[40] S. Khmelevskyi & P. Mohn. The order of the magnetic phase transitions in RCo_2 (R = rare earth) intermetallic compounds. J. Phys. Condens. Matter **12**, 9453 (2000).

[41] N. K. Singh, K. G. Suresh, A. K. Nigam, S. K. Malik, A. A. Coelho & S. Gama. Itinerant electron metamagnetism and magnetocaloric effect in RCo_2-based Laves phase compounds. J. Magn. Magn. Mater. **317**, 68 (2007).

[42] W. Zuo, F. Hu, J. Sun & B. Shen. Large reversible magnetocaloric effect in RMn_2 (R = Tb, Dy, Ho, Er) compounds. J. Alloys Compounds **575**, 162 (2013).

[43] O. Tegus, E. Brück, L. Zhang, Dagula, K. H. J. Buschow & F. R. de Boer. Magnetic phase transitions and magnetocaloric effects. Physica B **319**, 174 (2002).

[44] K. Mandal, A. Yan, P. Kerschl, A. Handstein, O. Gutfleisch & K. H. Muller. The study of magnetocaloric effect in R_2Fe_{17} (R = Y, Pr) alloys. J. Phys. D Appl. Phys. **37**, 2628 (2004).

[45] M. P. Annaorazov, K. A. Asatryan, G. Myalikgulyev, S. A. Nikitin, A. M. Tishin & A. L. Tyurin. Alloys of the Fe-Rh system as a new class of working material for magnetic refrigerators. Cryogenics **32**, 872 (1992).

[46] Songlin, Dagula, O. Tegus, E. Brück, J. C. P. Klaasse, F. R. de Boer & K. H. J. Buschow. Magnetic phase transition and magnetocaloric effect in $Mn_{5-x}Fe_xSi_3$. J. Alloys Compd. **334**, 249 (2002).

[47] H. Bińczycka, Ž. Dimitrijević, B. Gajić, A. Szytula. Atomic and magnetic structure of $Mn_{5-x}Fe_xSi_3$. Phys. stat. sol. **19**, K13 (1973).

[48] B. Aronsson. A note on the compositions and crystal structures of MnB_2, Mn_3Si, Mn_5Si_3 and $FeSi_2$. Acta Chem. Scand. **14**, 1414 (1960).

[49] P. J. Brown & J. B. Forsyth. Antiferromagnetism in Mn_5Si_3: the magnetic structure of the AF2 phase at 70 K. J. Phys.: Condens. Matter. **7**, 7619 (1995).

[50] M. Gottschilch, O. Gourdon, J. Persson, C. de la Cruz, V. Petricek & T. Brückel. Study of the antiferromagnetism of Mn_5Si_3: an inverse magnetocaloric effect material. J. Mater. Chem. **22**, 15275 (2012).

[51] P. J. Brown, J. B. Forsyth, V. Nunez & F. Tasset. The low-temperature antiferromagnetic structure of Mn_5Si_3 revised in the light of neutron polarimetry. J. Phys.: Condens. Matter. **4**, 10025 (1992).

[52] M. R. Silva, P. J. Brown & J. B. Forsyth. Magnetic moments and magnetic site susceptibilities in Mn_5Si_3. J. Phys.: Condens. Matter. **14**, 8707 (2002).

[53] C. Sürgers, T. Wolf, W. Adelmann, W. Kittler, G. Fischer & H. v. Löhneysen. Switching of a large anomalous Hall effect between metamagnetic phases of a non-collinear antiferromagnet. Scientific Reports **7**, 42982 (2017).

[54] L. Vinokurova, V. Ivanov, E. Kulatov & A. Vlasov. Magnetic phase transitions and electronic structure of the manganese silicides. J. Magn. Magn. Mater. **90 − 91**, 121 (1990).

[55] C. Sürgers, G. Fischer, P. Winkel & H. v. Löhneysen. Large topological Hall effect in the non-collinear phase of an antiferromagnet. Nat. Commun. **5**, 3400 (2014).

[56] P. Hering, K.Friese, J. Voigt, J. Persson, N. Aliouane, A. Grzechnik, A. Senyshyn & T. Brückel. Structure, magnetism, and the magnetocaloric effect of $MnFe_4Si_3$ single crystals and powder samples. Chem. Mater. **27**, 7128 (2015).

[57] A. Candini, O. Moze, W. Kockelmann, J. M. Cadogan & E. Brück, O. Tegus. Revised magnetic phase diagram for $Fe_xMn_{5-x}Si_3$ intermetallics. J. Appl. Phys. **95**, 6819 (2004).

[58] O. Gourdon, M. Gottschlich, J. Persson, C. de la Cruz, V. Petricek, M. A. McGuire & T. Brückel. Toward a better understanding of the magnetocaloric effect: An experimental and theoretical study of $MnFe_4Si_3$. J. Solid State Chem. **216**, 56 (2014).

[59] M. Herlitschke, B. Klobes, I. Sergueev, P. Hering, J. Persson & R. P. Hermann. Elasticity and magnetocaloric effect in $MnFe_4Si_3$. Phys. Rev. B **93**, 094304 (2016).

[60] M. F. J. Boeije, M. Maschek, X. F. Miao, N. V. Thang, N. H. van Dijk & E. Brück. Mixed magnetism in magnetocaloric materials with first-order and second-order magnetoelastic transitions. J. Phys. D: Appl. Phys. **50**, 174002 (2017).

[61] G. Jaeger. The Ehrenfest classification of phase transitions: introduction and evolution. Arch. Hist. Exact Sci. **53**, 51 (1998).

[62] M. Angst. T. Brückel, D. Richter & R. Zorn. Lecture notes of the 43rd IFF spring school 2012, Scattering methods for condensed matter research: towards novel applications at future sources. Forschungszentrum Jülich GmbH (2012).

[63] N. W. Ashcroft & N. D. Mermin. Solid State Physics. New York (1976).

[64] T. Chatterji. Neutron scattering from magnetic materials. Elsevier, Amsterdam; London (2006).

[65] S. Blundell. Magnetism in condensed matter. Oxford: Oxford University Press (2001).

[66] Th. Strässle, S. Janssen, F. Juranyi, A. Furrer, O. Moze, A. O. Pecharsky, V. K. Pecharsky & K. A. Gschneidner, Jr. Inelastic neutron scattering study of the intra-lanthanide alloys Er_xPr_{1-x} (x=0.6, 0.8). Phys. Rev. B **68**, 134411 (2003).

[67] C. Vecchini, O. Moze, A. O. Pecharsky, V. K. Pecharsky, K. A. Gschneidner Jr., E. Brück, R. Bewley & A. Klesnikov. Dynamic magnetic susceptibility of $Gd_5Si_2Ge_2$ and $Gd_4YSi_{1.9}Ge_{2.1}$. J. Appl. Phys. **95**, 7207 (2004).

[68] M. E. Gruner, W. Keune, B. Roldan Cuenya, C. Weis, J. Landers, S. I. Makarov, D. Klar, M. Y. Hu, E. E. Alp, J. Zhao, M. Krautz, O. Gutfleisch & H. Wende. Element-resolved thermodynamics of magnetocaloric $LaFe_{13-x}Si_x$. Phys. Rev. Lett. **114**,, 057202 (2015).

[69] G. Shirane, S. M. Shapiro & J. M. Tranquada. Neutron scattering with a triple-axis spectrometer: basic techniques. Cambridge University Press, New York (2002).

[70] G. L. Squires. Introduction to the theory of thermal neutron scattering. Cambridge University Press (2012).

[71] S. Raymond. Magnetic excitations. Collection SFN **13**, 02003 (2014).

[72] B. T. M. Willis & C. J. Carlile. Experimental neutron scattering. Oxford University Press (2009).

[73] F. Hippert, E. Geissler, J. L. Hodeau, E. Leliévre-Berna & J. -R. Regnard. Neutron and X-ray spectroscopy. Springer (2006).

[74] Z. Yamani, Z. Tun & D. H. Ryan. Neutron scattering study of the classical antiferromagnet MnF_2: a perfect hands-on neutron scattering teaching course. Can. J. Phys. **88**, 771 (2010).

[75] M. Kempa, B. Janousova, J. Saroun, P. Flores, M. Boehm, F. Demmel & J. Kulda. The FlatCone multianalyzer setup for ILL's three-axis spectrometers. Phys. B Condens. Matter **385**, 1080 (2006).

[76] E. Farhi, Y. Debab & P. Willendrup. iFit: A new data analysis framework. Applications for data reduction and optimization of neutron scattering instrument simulations with McStas. Journal of Neutron Research **17**, 5 (2014).

[77] B. Dorner. Coherent inelastic neutron scattering in lattice dynamics. Springer-Verlag, Berlin, Heidelberg, New York (1982).

[78] B. Roessli & P. Böni. Polarized Neutron Scattering. arXiv:cond-mat/0012180 (2000).

[79] T. Moriya. Spin fluctuations in itinerant electron magnetism. Springer Series in Solid-State Sciences **56** (1985).

[80] Y. Endoh & P. Böni. Magnetic excitations in metallic ferro- and antiferromagnets. J. Phys. Soc. Jpn. **75**, 111002 (2006).

[81] K. Schmalzl, W. Schmidt, S. Raymond, H. Feilbach, C. Mounier, B. Vettard & T. Brückel. The upgrade of the cold neutron three-axis spectrometer IN12 at the ILL. Nucl. Instr. Methods A **819**, 89 (2016).

[82] Heinz Maier-Leibnitz Zentrum et al. MIRA: Dual wavelength band instrument. J. of Large-Scale Res. Facil., **1**, A 3 (2015).

[83] Heinz Maier-Leibnitz Zentrum et al. PUMA: Thermal three axes spectrometer. J. of Large-Scale Res. Facil., **1**, A 13 (2015).

[84] L. P. Regnault, B. Geffray, P. Fouilloux, B. Longuet, F. Mantegazza, F. Tasset, E. Leliévre-Berna, S. Pujol, E. Bourgeat-Lami, N. Kernavanois, M. Thomas & Y. Gibert. Spherical neutron polarization analysis on the three-axis spectrometer IN22. Physica B **350**, E811 (2004).

[85] E. J. Fisher & J. B. Forsyth. Analytic approximations to form factors. Acta Cryst. A **27**, 545 (1971).

[86] S. Petit & F. Damay. SpinWave, a software dedicated to spin wave simulations. Neutron News **27**, 27 (2016).

[87] J. Villain. Influence d'un champ magnétique sur la diffusion des neutrons par les corps ferromagnétiques au point critique. J. Phys. France **24**, 622 (1963).

[88] T. J. Williams, A. E. Taylor, A. D. Christianson, S. E. Hahn, R. S. Fishman, D. S. Parker, M. A. McGuire, B. C. Sales & M. D. Lumsden. Extended magnetic exchange interactions in the high-temperature ferromagnet MnBi. Appl. Phys. Lett. **108**, 192403 (2016).

[89] Y. Yamaguchi, S. Tomoyoshi, M. Harada & G. Shirane. Magnons and phonons in MnSb. J. Magn. Magn. Mater. **103**, 50 (1992).

[90] P. Radhakrishna & J. W. Cable. Inelastic-neutron-scattering studies of spin-wave excitations in the pnictides MnSb and CrSb. Phys. Rev. B **54**, 11940 (1996).

[91] Y. Todate, K. Yamada, Y. Endoh & Y. Ishikawa. Spin-Waves in MnP. J. Phys. Soc. Jpn. **56**, 36 (1987).

[92] S. Yano, S. Itoh, T. Yokoo, S. Satoh, D. Kawana, Y. Kousaka, J. Akimitsu & Y. Endoh. Magnetic excitations in ferromagnetic phase of MnP. J. Magn. Magn. Mater. **347**, 33 (2013).

[93] S. Komura, K. Tajima, H. Fujii, Y. Ishikawa & T. Okamoto. Spin wave excitations in Fe_2P. J. Magn. Magn. Mater. **15 − 18**, 351 (1980).

[94] F. Semadeni, B. Roessli, P. Böni, P. Vorderwisch & T. Chatterji. Critical fluctuations in the weak itinerant ferromagnet Ni_3Al: A comparison between self-consistent renormalization and mode-mode coupling theory. Phys. Rev. B **62**, 1083 (2000).

[95] H. Fujii, Y. Uwatoko, K. Motoya, Y. Ito & T. Okamoto. Neutron scattering investigation of itinerant electron system Fe_2P. J. Phys. Soc. Jpn. **57**, 2143 (1988).

[96] C. Wilkinson, R. Wäppling & K. R. A. Ziebeck. Spin fluctuations in Fe_2P above its Curie temperature. J. Magn. Magn. Mater. **78**, 269 (1989).

[97] X. F. Miao, L. Caron, J. Cedervall, P. C. M. Gubbens, P. Dalmas de Réotier, A. Yaouanc, F. Qian, A. R. Wildes, H. Luetkens, A. Amato, N. H. van Dijk & E. Brück. Short-range magnetic correlations and spin dynamics in the paramagnetic regime of $(Mn,Fe)_2(P,Si)$. Phys. Rev. B **94**, 014426 (2016).

[98] J. W. Cable & R. M. Nicklow. Spin dynamics of Gd in an applied magnetic field. J. Phys. Condens. Matter. **1**, 7425 (1989).

[99] R. J. Joenk. Adiabatic magnetization of antiferromagnets. J. Appl. Phys. **34**, 1097 (1963).

[100] P. J. von Ranke, N. A. de Oliveira, B. P. Alho, E. J. Plaza, V. S. de Sousa, L. Caron & M. S. Reis. Understanding the inverse magnetocaloric effect in antiferro- and ferrimagnetic arrangements. J. Phys. Condens. Matter. **21**, 056004 (2009).

[101] Y. Q. Zhang & Z. D. Zhang. Giant magnetoresistance and magnetocaloric effects of the $Mn_{1.82}V_{0.18}Sb$ compound. J. Alloys Comp. **365**, 35 (2004).

[102] S. A. Nikitin, G. Myalikgulyev, A. M. Tishin, M. P. Annaorazov, K. A. Asatryan & A. L. Tyurin. The magnetocaloric effect in $Fe_{49}Ni_{51}$ compound. Phys. Lett. A. **148**, 363 (1990).

[103] T. Tohei, H. Wada & T. Kanomata. Negative magnetocaloric effect at the antiferromagnetic to ferromagnetic transition of Mn_3GaC. J. Appl. Phys. **94** 1800 (2003).

[104] W. J. Hu, J. Du, B. Li, Q. Zhang & Z. D. Zhang. Giant magnetocaloric effect in the Ising antiferromagnet DySb. Appl. Phys. Lett. **92**, 192505 (2008).

[105] A. Z. Menshikov, A. P. Vokhmyanin & Yu. A. Dorofeev. Magnetic structure and phase transformations in Mn_5Si_3. Phys. Status Solidi b **158**, 319 (1990).

[106] G. H. Lander, P. J. Brown & J. B. Forsyth. The antiferromagnetic structure of Mn_5Si_3. Proc. Phys. Soc. **91**, 33 (1967).

[107] T. Hahn. International tables for crystallography. Volume A, Space-group symmetry (5th ed.). Dordrecht: Kluwer Academic Publishers, for the International Union of Crystallography (2002).

[108] F. I. Fedorov. Theory of elastic waves in crystals. Plenum Press, New York (1968).

[109] M. Hase, M. Soda, T. Masuda, D. Kawana, T. Yokoo, S. Itoh, A. Matsuo, K. Kindo & M. Kohno. Experimental confirmation of spin gap in antiferromagnetic alternating spin $-\frac{3}{2}$ chain substances $RCrGeO_5$ (R=Y or ^{154}Sm) by inelastic neutron scattering experiments. Phys. Rev. B **90**, 024416 (2014).

[110] R. Ballou. Geometric frustration in rare earth antiferromagnetic compounds. J. Alloys Compounds **275 − 277**, 510 (1998).

[111] R. Ballou, B. Ouladdiaf, P. J. Brown, M. D. N. Regueiro & C. Lacroix. Unusual field-induced transition in a frustrated itinerant antiferromagnet. Phys. Rev. B **45**, 3158 (1992).

[112] C. Sürgers, W. Kittler, T. Wolf & H. v. Löhneysen. Anomalous Hall effect in the noncollinear antiferromagnet Mn_5Si_3. AIP Advances **6**, 055604 (2016).

[113] J. Oh, M. D. Le, H.-H. Nahm, H. Sim, J. Jeong, T. G. Perring, H. Woo, K. Nakajima, S. Ohira-Kawamura, Z. Yamani, Y. Yoshida, H. Eisaki, S.-W. Cheong, A. L. Chernyshev & J.-G. Park. Spontaneous decays of magneto-elastic excitations in non-collinear antiferromagnet (Y,Lu)MnO_3. Nat. Commun. **7**, 13146 (2016).

[114] P. Dai, H. Y. Hwang, J. Zhang, J. A. Fernandez-Baca, S.-W. Cheong, C. Kloc, Y. Tomioka & Y. Tokura. Magnon damping by magnon-phonon coupling in manganese perovskites. Phys. Rev. B **61**, 9553 (2000).

[115] R. Pradip, P. Piekarz, A. Bosak, D. G. Merkel, O. Waller, A. Seiler, A. I. Chumakov, R. Rüffer, A. M. Oleś, K. Parlinski, M. Krisch, T. Baumbach & S. Stankov. Lattice dynamics of EuO: Evidence for giant spin-phonon coupling. Phys. Rev. Lett. **116**, 185501 (2016).

[116] S. Petit, F. Moussa, M. Hennion, S. Pailhés, L. Pinsard-Gaudart & A. Ivanov. Spin phonon coupling in hexagonal multiferroic $YMnO_3$. Phys. Rev. Lett. **99**, 266604 (2007).

[117] S. Tóth, B. Wehinger, K. Rolfs, T. Birol, U. Stuhr, H. Takatsu, K. Kimura, T. Kimura, H. Rønnow & C. Rüegg. Electromagnon dispersion probed by inelastic X-ray scattering in $LiCrO_2$. Nat. Commun. **7**, 13547 (2016).

[118] A. B. Sushkov, R. Valdés Aguilar, S. Park, S-W. Cheong & H. D. Drew. Electromagnons in multiferroic YMn_2O_5 and $TbMn_2O_5$. Phys. Rev. Lett. **98**, 027202 (2007).

[119] E. Burkel. Phonon spectroscopy by inelastic x-ray scattering. Rep. Prog. Phys. **63**, 171 (2000).

[120] G. Xu, Z. Xu & J. M. Tranquada. Absolute cross-section normalization of magnetic neutron scattering data. Rev. Sci. Instrum. **84**, 083906 (2013).

[121] O. Steinsvoll, R. M. Moon, W. C. Koehler & C. G. Windsor. Magnetic form factor of metallic iron and nickel as seen by inelastic neutron scattering from phonons. Phys. Rev. B **24**, 4031 (1981).

[122] P. J. Brown, I. K. Jassim, R. M. Mankikar, Y. Nakamura & K. R. A. Ziebeck. An inelastic polarized neutron scattering investigation of the dynamic form factor in the Invar alloy $Fe_{65}Ni_{35}$. J. Phys. Colloques **49**, C8-307 (1988).

Acknowledgements

Most results on Chapter 4 are based on the publication in Phys. Rev. B **96**, 104407 (2017). Sections in Chapter 4 dealing with that topic present additional information that is not included in this publication. Concerning this publication the single crystal used for neutron scattering experiments was grown by **J. Persson**, **P. Hering** and **Dr. K. Friese**. **Dr. A. Schneidewind** was local contact on PUMA. **Dr. R. Georgii** was instrument responsible of MIRA. Data on MIRA were collected from **Dr. J. Voigt**. **Dr. S. Raymond** and **Dr. K. Schmalzl** were instrument responsibles of IN12 and IN22. **N. Biniskos**, **Dr. S. Raymond** and **Dr. K. Schmalzl** participated in the experiments on PUMA, IN12 and IN22. **Dr. S. Raymond** and **Dr. K. Schmalzl** taught **N. Biniskos** how to analyze the inelastic neutron data. All data have been analyzed by **N. Biniskos**. **Dr. S. Raymond** taught **N. Biniskos** how to perform spin-wave simulations with the SpinWave software package. Spin-wave simulations were performed by **N. Biniskos**. **Prof. Dr. T. Brückel** was the scientific coordinator of the project and head of the JCNS group in Jülich and in Garching. **N. Biniskos**, **Dr. S. Raymond** and **Dr. K. Schmalzl** wrote the paper with input from all authors.

Some results on Chapter 5 are based on a manuscript (title: Spin fluctuations drive the inverse magnetocaloric effect in Mn_5Si_3) accepted (16 May 2018) in Phys. Rev. Lett. Sections in Chapter 5 dealing with that topic present additional information that is not included in this publication. Concerning this publication the single crystal used for neutron scattering experiments was grown by **J. Persson** and **N. Biniskos**. **Dr. S. Petit** was local contact on 2T1. **Dr. P. Steffens** was instrument responsible of ThALES. **Dr. K. Schmalzl** and **Dr. S. Raymond** were instrument responsible of IN12. **N. Biniskos**, **Dr. K. Schmalzl** and **Dr. S. Raymond** participated in the experiments. All data have been analyzed by **N. Biniskos**. **Prof. Dr. T. Brückel** was the scientific coordinator of the project and head of the JCNS group in Jülich and in Garching. **N. Biniskos**, **Dr. K. Schmalzl** and **Dr. S. Raymond** wrote the manuscript with input from all authors.

I would like to express my gratitude to the following people:

Prof. Dr. Thomas Brückel for giving me the opportunity to work at JCNS, for the fruitful discussions and for reviewing my thesis. **Prof. Dr. Georg Roth** for reviewing my thesis. **Dr. Karin Schmalzl** and **Dr. Stéphane Raymond** for being my supervisors. I sincerely acknowledge them for their patience and support during my thesis. I had a great time discussing and working with them. **Jörg Persson** for his help during the Mn_5Si_3 single crystal growth. **Dr. Jörg Voigt**, **Dr. Karen Friese** and **Paul Hering** for providing a well characterized (by magnetometry, X-ray and neutron diffraction) $MnFe_4Si_3$ single crystal sample. **Dr. Paul Steffens** (ThALES−ILL), **Dr. Martin Böhm** (ThALES−ILL), **Dr. Wolfgang Schmidt** (IN22−ILL), **Dr. Frédéric Bourdarot** (IN22−ILL), **Dr. Mechthild Enderle** (IN20−ILL), **Dr. Andrea Piovano** (IN8−ILL), **Dr. Alexandre Ivanov** (IN8−ILL), **Dr. Alexei Bossak** (ID28−ESRF), **Dr. Sofia-Michaela Souliou** (ID28−ESRF), **Dr. Sylvain Petit** (4F1−LLB), **Dr. Robert Georgii** (MIRA−MLZ), **Dr. Kirill Nemkovski** (DNS−MLZ) and **Dr. Astrid Schneidewind** (PANDA−MLZ) for their help and support during the beamtimes. **Barbara Daegener** (JCNS institute secretary) for being always helpful. My family and friends for their support. Last but not least I would like to thank the colleagues at the ILL, CEA, ESRF, LLB, JCNS and MLZ for the stimulating discussions on various social occasions. Without you all, my work would not have been successfully completed. It was a great experience for me working in a comfortable and friendly atmosphere.

The present thesis project was co-financed from Forschungszentrum Jülich GmbH and CEA Grenoble.

Band / Volume 173
Spin scattering of topologically protected electrons at defects
P. Rüßmann (2018), vii, 230 pp
ISBN: 978-3-95806-336-5

Band / Volume 174
Interfacing EuO in confined oxide and metal heterostructures
P. Lömker (2018), vi, 140 pp
ISBN: 978-3-95806-337-2

Band / Volume 175
Operando Chemistry and Electronic Structure of Electrode / Ferroelectric Interfaces
S. Gonzalez (2018), 172 pp
ISBN: 978-3-95806-341-9

Band / Volume 176
Magnetic Properties of Self-assembled Manganese Oxide and Iron Oxide Nanoparticles
Spin Structure and Composition
X. Sun (2018), ii, 178 pp
ISBN: 978-3-95806-345-7

Band / Volume 177
Model-based reconstruction of magnetisation distributions in nanostructures from electron optical phase images
J. Caron (2018), XXI, 183 pp
ISBN: 978-3-95806-346-4

Band / Volume 178
Simultaneous dual-color imaging on single-molecule level on a Widefield microscope and applications
R. Ledesch (2018), ix, 119 pp
ISBN: 978-3-95806-348-8

Band / Volume 179
Methoden der Leitfähigkeitsuntersuchung mittels Rasterkraftmikroskop und deren Anwendung auf Barium Titanat Systeme
B. Reichenberg (2018), x, 144 pp
ISBN: 978-3-95806-350-1

Band / Volume 180
Manipulation of magnetism in iron oxide nanoparticle / $BaTiO_3$ composites and low-dimensional iron oxide nanoparticle arrays
L. Wang (2018), VI, 151 pp
ISBN: 978-3-95806-351-8

Band / Volume 181
Creating and characterizing a single molecule device for quantitative surface science
M. Green (2018), viii, 142 pp (untersch. Pag.)
ISBN: 978-3-95806-352-5

Band / Volume 182
8th Georgian-German School and Workshop in Basic Science
A. Kacharava (Ed.) erscheint nur als CD (2018)
ISBN: 978-3-95806-353-2

Band / Volume 183
Topological properties of complex magnets from an advanced *ab-initio* Wannier description
J.-P. Hanke (2018), xi, 173 pp
ISBN: 978-3-95806-357-0

Band / Volume 184
Translation Initiation with 70S Ribosomes: A Single Molecule Study
C. Remes (2018), iv, 113 pp
ISBN: 978-3-95806-358-7

Band / Volume 185
Scanning tunneling potentiometry at nanoscale defects in thin films
F. Lüpke (2018), iv, 144 pp (untersch. Pag.)
ISBN: 978-3-95806-361-7

Band / Volume 186
Inelastic neutron scattering on magnetocaloric compounds
N. Biniskos (2018), iii, 92 pp
ISBN: 978-3-95806-362-4

Weitere ***Schriften des Verlags im Forschungszentrum Jülich*** unter
http://wwwzb1.fz-juelich.de/verlagextern1/index.asp

Schlüsseltechnologien / Key Technologies
Band / Volume 186
ISBN 978-3-95806-362-4

Mitglied der Helmholtz-Gemeinschaft

JÜLICH
Forschungszentrum